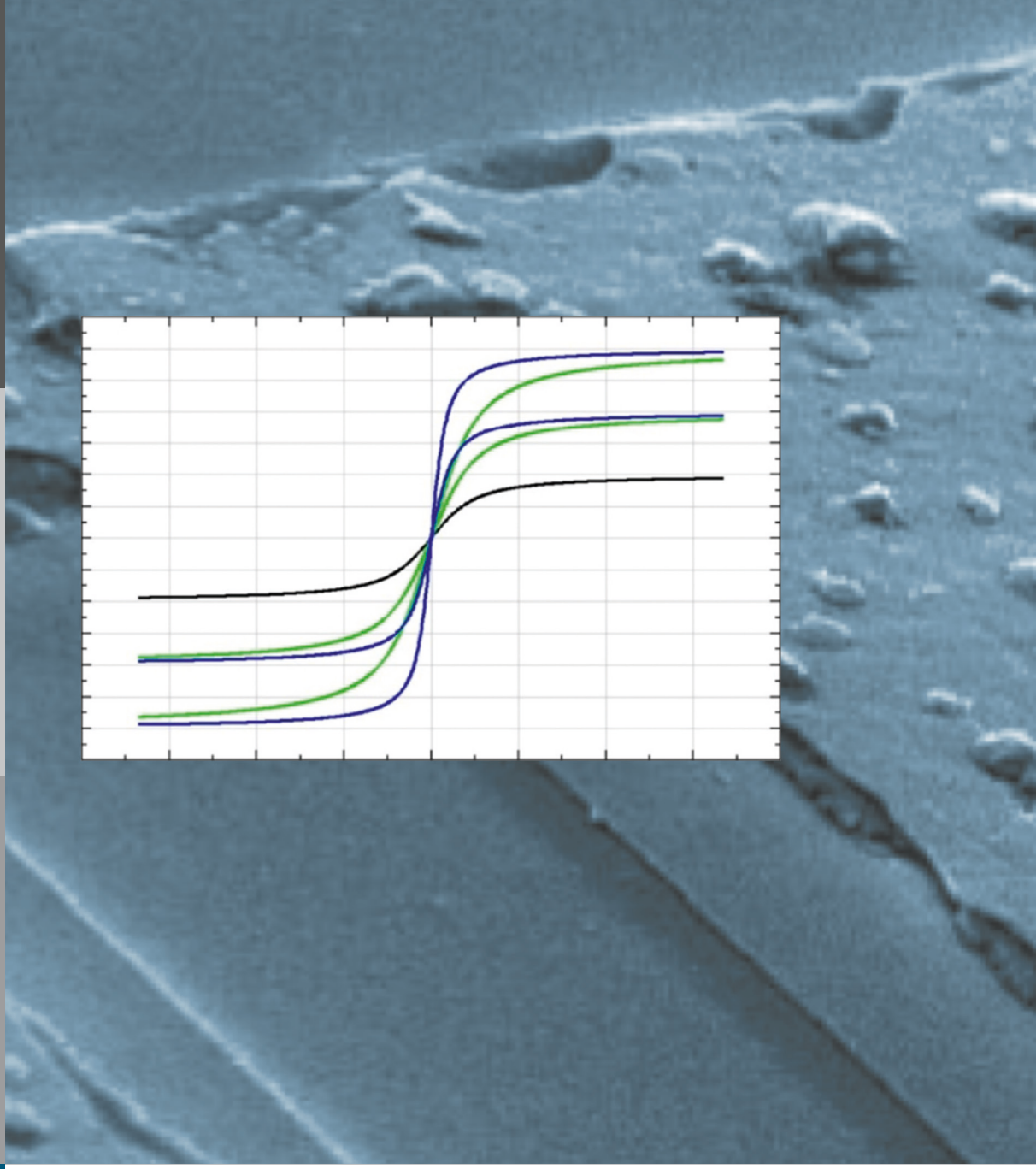

High Temperature Radio-Frequency Superconducting Quantum Interference Device System for Detection of Magnetic Nanoparticles

Alf Pretzell

Member of the Helmholtz Association

JÜLICH
FORSCHUNGSZENTRUM

Schriften des Forschungszentrums Jülich
Reihe Schlüsseltechnologien / Key Technologies Band / Volume 48

Forschungszentrum Jülich GmbH
Peter Grünberg Institute / Institute of Complex Systems
Bioelectronics (PGI-8 / ICS-8)

High Temperature Radio-Frequency Superconducting Quantum Interference Device System for Detection of Magnetic Nanoparticles

Alf Pretzell

Schriften des Forschungszentrums Jülich
Reihe Schlüsseltechnologien / Key Technologies Band / Volume 48

ISSN 1866-1807 ISBN 978-3-89336-814-3

Bibliographic information published by the Deutsche Nationalbibliothek.
The Deutsche Nationalbibliothek lists this publication in the Deutsche Nationalbibliografie; detailed bibliographic data are available in the Internet at http://dnb.d-nb.de.

Publisher and Distributor:	Forschungszentrum Jülich GmbH Zentralbibliothek 52425 Jülich Phone +49 (0) 24 61 61-53 68 · Fax +49 (0) 24 61 61-61 03 e-mail: zb-publikation@fz-juelich.de Internet: http://www.fz-juelich.de/zb
Cover Design:	Grafische Medien, Forschungszentrum Jülich GmbH
Printer:	Grafische Medien, Forschungszentrum Jülich GmbH
Copyright:	Forschungszentrum Jülich 2012

Schriften des Forschungszentrums Jülich
Reihe Schlüsseltechnologien / Key Technologies Band / Volume 48

D 82 (Diss., RWTH Aachen University, 2011)

ISSN 1866-1807
ISBN 978-3-89336-814-3

The complete volume is freely available on the Internet on the Jülicher Open Access Server (JUWEL) at http://www.fz-juelich.de/zb/juwel

Contents

1 Introduction

This doctoral thesis was aimed at establishing a set-up with high-temperature superconductor (HTS) radio-frequency (rf) superconducting quantum interference device (SQUID) technology for the detection of magnetic nanoparticles and in particular for testing applications of magnetic nanoparticle immunoassays. It was part of the EU-project “Biodiagnostics” running from 2005 to 2008.

The method of magnetic binding assays was developed as an alternative to other methods of concentration determination like enzyme linked immunosorbent assay (ELISA), or fluorescent immunoassay. The ELISA has sensitivities down to analyte-concentrations of pg/ml - p. 261 in [Raem 2007]. Multiple incubation and washing steps have to be performed for these techniques, the analyte has to diffuse to the site of binding. The magnetic assay uses magnetic nanoparticles as markers for the substance to be detected. It is being explored by current research and shows similar sensitivity [Enpuku 2007] compared to ELISA but in contrast

- does not need any washing and can be read out directly after binding
- can be applied in solution with opaque media, e.g. blood or muddy water
- additionally allows magnetic separation or concentration
- in combination with small magnetoresistive or Hall sensors, allows detection of only a few particles or even single beads.

For medical or environmental samples, maybe opaque and containing a multitude of substances, it would be advantageous to devise an instrument, which allows to be read out quickly and with high sensitivity. Due to the mentioned items the magnetic assay might be a possibility here.

Magnetic colloids have been investigated since the middle of the sixties when it became feasible to synthesize them - p. 1 in [Blum 1997]. As a possible application for these colloids Kriz introduced the idea of magnetic immunoassays in 1996 [Kriz 1996].

1.1 Aim of the Biodiagnostics Project

For reading and exploring magnetic immunoassay it is advantageous to make use of SQUIDs which regarding to sensitivity are on the same level as spin exchange relaxation-free (SERF) magnetometers [Kominis 2003]. The latter have been investigated only recently.

The targeted objective of “Biodiagnostics” was therefore “to develop new medical diagnostic tools based on the most sensitive detector technologies available today” [Biodiagnotics 2009]. The state-of-the-art research of 2005 - at the beginning of the project - yielded many promising approaches using magnetic immunoassays as will be discussed in the theoretical chapter of this thesis. However, no direct comparisons with standard clinical tests and no strict, comparable procedures to determine detection limits of the various techniques had been performed. This was one aim of “Biodiagnostics”.

Two gradiometric SQUID devices, a Hall sensor and measurements with a gradiometric inductive device were set up within “Biodiagnostics” to realize different approaches of magnetic immunoassays. Several groups developed and characterized magnetic nanoparticles. The following questions regarding our system were posed:

- Which sensitivity is achievable? The instruments are benchmarked with a reference assay using the biotin-streptavidin system.
- Which method of readout – relaxometry, alternating current (AC) susceptometry etc. - is advantageous?
- Is the assay comparable to standard enzyme linked immunosorbent assay (ELISA)?

1.2 Aim of this Thesis

Following the framework of the European project we tried to set up a system using gradiometric HTS rf SQUIDs. In particular we tried to extend and optimize the sample supply for magnetic immunoassay instruments. We decided to design the instrument for several readout techniques:

- Magnetorelaxometry - the magnetic field is rapidly decreased to observe the relaxation speed of the particle.

- AC susceptometry detects the amplitude and the phase shift of the particle's magnetization at oscillating fields.

- With frequency mixing a field having two distinct frequencies is applied: due to the non-linearity of the magnetization curve of the particles, the second derivative of the magnetization shows a peak at the sum of the two frequencies. For low magnetization fields all other linear magnetizations of the instrument et cetera do not play a role at this frequency.

Using an HTS rf SQUID the present study is a compromise between inductive instruments and costly low-temperature superconducting (LTS) SQUID instruments. The main assay strategy of our system is to perform measurements in the liquid without binding to any walls by making use of larger beads to which the particles are bound.

In addition to finally analyzing the sensitivity of the system, we tried to achieve the following items during the construction process

- integration of a fast room-temperature sample supply and a compact coil arrangement with a nitrogen-cooled SQUID sensor

- reliable operation of a gradiometric HTS SQUID with conventional tank circuit on top of a nitrogen cooled sapphire

- establishment of the three mentioned techniques for readout and the process steps required for optimal measurement results

1.3 Outline of the Thesis

Following this “Introduction” in the chapter “Theory” the most important theoretical framework mainly for SQUID sensors, magnetic nanoparticles and magnetic immunoassays is elucidated. To bring the instrument in line with current research state-of-the-art technology is also presented.

In “Set-up”, the construction process of the device is explained. This includes descriptions of the respective components and their development, characterization of the components and practical details for operation.

The chapter “Experiments and Results” presents the results of our first measurements with beads and nanoparticles as proof of principle. Prior to this some experiments to characterize the instrument like determination of the noise level and mechanical balance have been made. A first impression of sensitivity and comparability of susceptometric and relaxometric readout is provided.

The section “Discussion and Outlook” presents specifications of the device, sums up the two previous chapters and provides answers to the items mentioned in the previous sections 1.1 and 1.2. The results are compared to the the work of other groups. Ideas for future improvements and possible applications of the built system are suggested.

Following the section “References” the section “Annex” explains the abbreviations used, presents important physical data for set-up and experiments and provides an account of the materials and instruments used. Important proof and derivations from the theoretical chapter are presented as well.

General content of student textbooks is not cited. The content of publications and monographs is cited. Some physical data has been taken from industrial resources as indicated.

2 Theory

It was the aim of this project to engineer a state-of-the-art instrument and to perform basic experiments and not to develop new theoretical background. Nevertheless, the most important theory for set-up and performed experiments will be presented in the following. Since the beginning of magnetic immunoassay dates back only about a decade, no comprehensive monograph is available up to now – so the aim is

- to present the main theoretical framework for the following chapters
- to show important developments in the history of SQUID magnetic immunoassay
- to show how this device and the corresponding experiments fit into present state-of-the-art technology
- to present important publications from the field – many of them are reviews and can serve as a starting point for further research
- to stimulate feasible or advantageous future applications, in particular of this device.

The items are ordered in the respective sections according to the main parts of the system

- cooling of the sensor including evacuation
- state-of-the-art SQUID sensor physics
- state-of-the-art magnetic nanoparticles physics
- state-of-the-art magnetic immunoassay strategies
- measurements.

Only the basics are presented here. It is evident and shall be seen in the following that already at these fundamental stages, a large amount of theory would be necessary - completeness cannot be achieved and is not intended.

2.1 Cooling

Our lab works with high-temperature superconducting (HTS) sensors, which require cooling and are optimized with respect to the temperatures of liquid nitrogen. The sensor is thermally connected to a bath of liquid nitrogen and simultaneously thermally isolated from room-temperature environment as much as possible. A sapphire finger constitutes the thermal connection to liquid nitrogen. Evacuation is used to suppress of the heat transfer by convection. Finally, heat radiation is minimized by wrapping the cooling components using superinsulation (aluminum-coated Mylar) foil. The temperature on top of the sapphire is balanced by the incoming heat from the environment and the heat flow through the sapphire finger to the nitrogen-cooled copper block. If there was no incoming energy, the temperature at the top would level at the temperature of liquid nitrogen. This is not the case because there is a small amount of incoming energy. In the following some considerations concerning this equilibrium are developed.

2.1.1 Conduction

In a simplified model, which is based on the assumption of only two temperatures T_1 at the top and T_2 at the copper block, the heat flow j through the sapphire of length l, area A and heat conductance λ amounts to

$$j = A\,\lambda\frac{T_1 - T_2}{l} \tag{1}$$

It is determined by the incoming heat energy mainly due to radiation. By rearranging the equation it becomes obvious that the difference of the temperatures T_1 and T_2 is proportional to j and l and to the inverse of A and λ.

2.1.2 Convection

The convective energy transfer is impeded by the evacuation of the dewar. No flow of heated gas is possible – the mean free path of the molecules is larger than the dewar at 10^{-5} mbar. Therefore, convection can be disregarded entirely.

2.1.3 Radiation

The incoming radiative energy of the dewar at room temperature can be approximated by black body radiation according to Kirchhoff and is independent of the dewar's form. The radiation is reflected by smooth metallic surfaces – to reduce the transmitted energy, the sapphire finger is covered in aluminum foil.

2.2 SQUID Sensor

2.2.1 Superconductivity

Superconductivity - the disappearance of electric resistance - was discovered 1911 in the Netherlands by Heike Kammerling-Onnes for the element mercury. The transition to this state occurs like the transition to a new state of aggregation at a temperature, which is characteristic for each substance.

Superconductivity is a phenomenon like many discoveries over approximately the last 200 years not found on earth because of the low temperatures needed. Up to now, it has not been found in our natural environment and might be new physics without precedence in nature. Though worthy of discussion and not part of the technology impact assessment [Grunwald 2002] this topic – natural versus artificial processes and implications for science - will not be dealt with in this context.

With the discovery of high temperature superconductors by Bednorz and Müller in the year 1986 [Bednorz 1986], it became possible to obtain superconductivity at the boiling temperatures of liquid nitrogen, much facilitating handling and greatly reducing costs.

A few important and clarifying experiments which show the fundamentals of superconductivity regarding SQUIDs according to [Buckel 2003]:

- If a superconducting ring is cooled down in a magnetic field the flux is frozen after the field has been shut down. The ring also shields from and compensates outer magnetic flux penetrating its center. The current persists as long as the ring stays cooled, the current in a ring with resistance would rapidly decay exponentially. An early experiment of this kind in 1914 is described in [de Bruyn Ouboter 1987].

- Another phenomenon which is of interest for the present application of superconductivity is the quantization of frozen flux in such a ring in multiples of the flux quantum Φ_0, which amounts to h/(2e) = 2.068 x 10^{15} Tm^2. An experiment has been carried out by the group around Doll [Doll 1961], who cooled down a mini-cylinder made of lead (diameter 10 µm) and measured the torque in an oscillating outer field in resonance. A step function of the frozen flux was observed to be comparable to the Millikan experiment proving the elementary charge.

- A third experiment by Möllenstedt et al. [Möllenstedt 1961] is worth to be mentioned to show the effect of the magnetic flux on the electron's wave. Möllenstedt split up an electron beam with a negatively charged thread and guided the two beams around both sides of a magnetic coil. Then the two beams were brought to interference. They showed the characteristic interference pattern fitting to their momenta due to their quantum mechanical, wavelike structure. If a magnetic flux was generated in the coil the pattern shifted – a phase shift of one period was generated by an applied flux of $\Phi_0/2$! The fact that the flux in a superconducting ring is measurable in multiples of Φ_0 leads with other evidence to the assumption of paired electrons in superconductivity.

2.2.2 First Josephson Equation

The effects of weak links in superconductivity have been foreseen and formulated by Brian Josephson [Josephson 1962]. The theoretical considerations of this publication shall not be discussed here. Two weakly linked superconductors are connected by a quasi-point contact or are separated by a very thin isolating layer. A supercurrent I is able to flow over this connection up to a critical threshold I_c. Beyond this current I_c a voltage across the weak link is generated.

A superconducting ring for example possessing such a weak link still reacts to an outer magnetic field as described in the next section. The first Josephson effect relates the observed current I to the phase difference θ of the wave function over the link in the following way

(2) $$I = I_c \sin(\theta)$$

where I_c is the maximal supercurrent as described. The phase is related to magnetic flux shown in the experiment by Möllenstedt discussed above. The precise relations are discussed in the next section. Experiments, which show this effect for HTS superconductors have been performed for a microbridge, for instance. A zero voltage current and the modulation of the current for a transversally applied magnetic field are shown in this publication [Kataria 1988].

2.2.3 Physics of the rf SQUID

The idea of a superconducting ring with a weak link is developed in [Silver 1965]. In [Silver 1967] the following considerations about the behavior of such a ring in a magnetic field are presented.

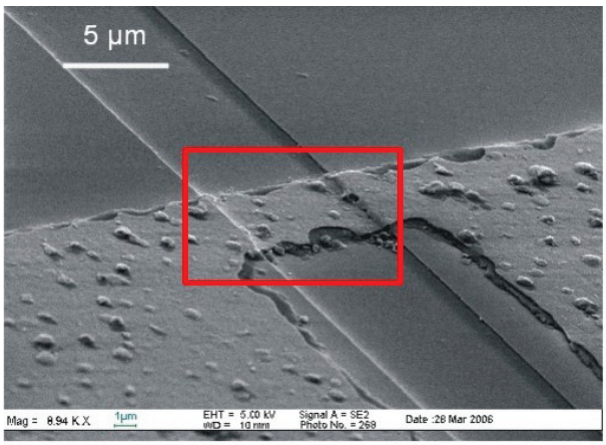

Figure 1: Electron micrograph showing the step edge junctions (marked by the red frame) of the Juelich SQUIDs fabricated in thin film technique. The grain boundaries at the two steps visible in the picture form these junctions.

Due to the weak link and its limited critical current I_c an external magnetic flux Φ_e is only partially shielded. According to Josephson, the flux Φ_i in the ring amounts to

(3) $$\Phi_i = \Phi_e + L_{SQ} I_c \sin(\theta)$$

with θ, the phase difference of the electron's wave function across the junction and the inductance L_{SQ} of the SQUID. According to quantum mechanics this phase difference depends on the vector potential around the ring by the equation

(4) $$\theta = \frac{4e\pi}{h} \int_{I(0)}^{I(2\pi)} A \cdot dI$$

with

(5) $$\int_{I(0)}^{I(2\pi)} A \cdot dI = \Phi_i$$

resulting in

(6) $$\sin(\theta) = -\sin\left(2\pi \cdot \frac{\Phi_i}{\Phi_0}\right)$$

Φ_0 being the flux quantum. With the first Josephson relation

(7) $$I = I_c \sin(\theta)$$

the internal flux Φ_i is specified by the expression

(8) $$\Phi_i = \Phi_e - L I_c \sin\left(2\pi \cdot \frac{\Phi_i}{\Phi_0}\right)$$

As shown in Figure 2 the gradient of the curve varies with the period of the flux quantum for different values of external flux Φ_e. The non-hysteretic case for a value of 0.82 < 1 for $2\pi L_{SQ} I_c / \Phi_0$ is shown in green – in this case the gradient is always limited to positive values. The blue curve displays the hysteretic case for $2\pi L_{SQ} I_c / \Phi_0 = 2.70 > 1$ – here parts of the curve

show a negative slope, which are not followed by the SQUID. Instead flux is caught, as shown by the dotted lines, and energy is dissipated. Strictly speaking, these relations are only valid for low thermal fluctuations: According to [Chesca 1997], for large fluctuations, the term $I_c \sin(\theta)$ is averaged due to a thermally caused distribution of θ and thus diminished.

The height of the tank circuit's voltage also varies periodically with the external flux as explained in the next section. During actual operation the SQUID is flux-locked, meaning the flux in the ring and thereby the height of the voltage is held constant by an adjusted coil and the current, which generates this compensating field, is measured.

In [Silver 1967] the authors verify the presented theoretical results experimentally for the hysteretic and non-hysteretic case. Interestingly they use the readily developed properties of the superconducting ring with a weak link to construct a sensitive magnetometer. This magnetometer resembles present SQUIDs using a tank circuit, flux-locked loop – called servo mode here - and the height of an rf-voltage for readout. But the ring is not inductively coupled to the circuit as in our case. Instead it is connected in series with the tank circuit.

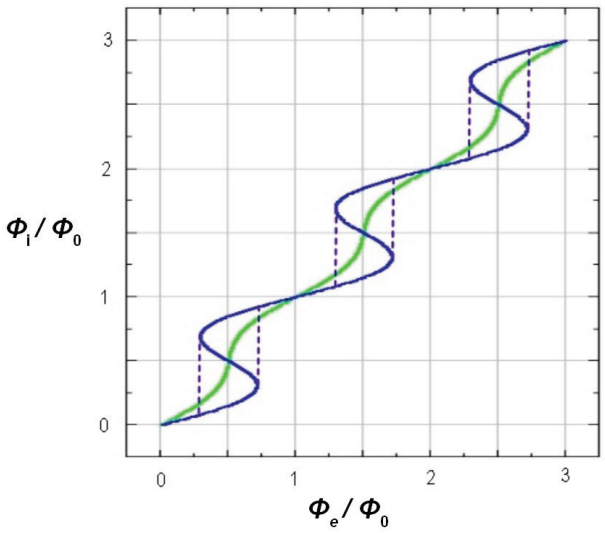

Figure 2: Graph of the internal flux Φ_i versus external flux Φ_e in units of the flux quantum Φ_0. Non-hysteretic case (green), hysteretic case (blue).

This resulted in further developments in [Zimmermann 1968]. An early review of superconducting quantum magnetometer measuring even magnetic fields of as small as approx. 10 fT is given by [Webb 1972]. First HTS rf SQUIDs were set up in 1987 [Zimmerman 1987].

The inductance L_{SQ} of the SQUID shall not be chosen too high, as explained in the next section. For concentration of the flux the SQUID is constructed as a disc of diameter d_d with a hole of diameter d_h. The flux concentrating superconducting disc is referred to as washer. In [Ketchen 1989] the effective area A_{eff} of the SQUID has been shown to be proportional to $d_d \cdot d_h$ due to concentration of the flux by the washer – clear experimental verification of the proportionality of A_{eff} and d_d has been provided for square shaped washers in this publication.

In the present study, the SQUID is constructed as a gradiometer. There the currents of the two centers in the SQUID cancel each other out for homogeneous magnetic fields. The principle of opposing currents at the junction and the layout of design is shown in the drawing below.

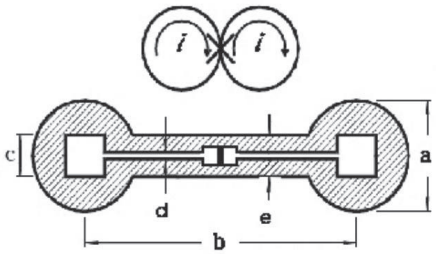

Figure 3: Principle (top) and layout of the design (bottom) used for the SQUIDs of this study – not to scale.

Numbers for the dimensions a – d are given in the chapter “Set-up”. The ratio of the field measured by the gradiometer to the applied homogenous field is called the balance of the gradiometer. For our gradiometers, balances in the range of 0.1 % are reached [Zhang 1997].

2.2.4 Operation of the rf SQUID

Figure 4 depicts the three principle elements for operation of the SQUID: On the left the coupling coil is shown where an rf-current I_{rf} is injected. This is adjusted to be in resonance with

the tank circuit shown on the right. At the same time, the voltage V_{rf} of this oscillation is measured. In between both elements, the SQUID is positioned and cooled to 77 K by liquid nitrogen.

In the hysteretic case for a particular value of an external magnetic field threaded through the SQUID, a the voltage V_{rf} is limited due to dissipating processes in the tank circuit at the point where flux is caught. In the non-hysteretic case the SQUID is a flux-sensitive inductor. For a particular value of an external magnetic field, it puts the tank circuit out of tune thus reducing the voltage V_{rf}.

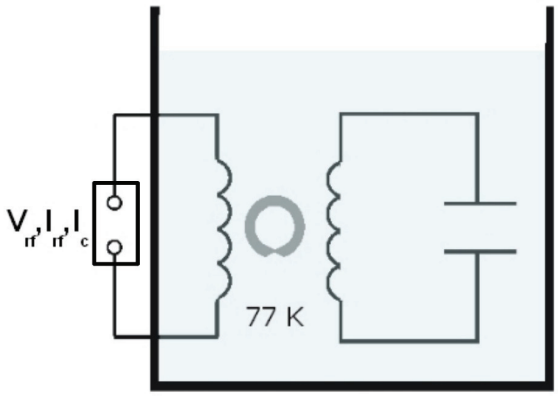

Figure 4: Coupling coil with electronics circuit, cooled SQUID and tank circuit - elements for SQUID operation schematically.

A current I_c is guided into the coupling coil via a feedback resistor. Holding V_{rf} at a constant value, the threading magnetic field is fixed at a constant value as well. I_c is adjusted relative to the strength of the changing outer magnetic field. If the change is too fast, the electronics cannot follow.

Figure 5 shows in more detail but still simplified the circuit diagram of the SQUID with important parameters. The three parts of the system - SQUID, tank circuit and coupling coil with its electronics – and the parameters are discussed in the following. Then hysteretic operation – used for most of the measurements – and briefly non-hysteretic operation of the sensor is treated.

The transfer function

(9) $$f(\Phi) = \frac{\partial V}{\partial \Phi}$$

and optimal coupling of SQUID to the tank circuit as well as noise contributions are considered. Most of the ideas are taken from [Zhang 1990], [Mück 2000] and [Clarke 2003].

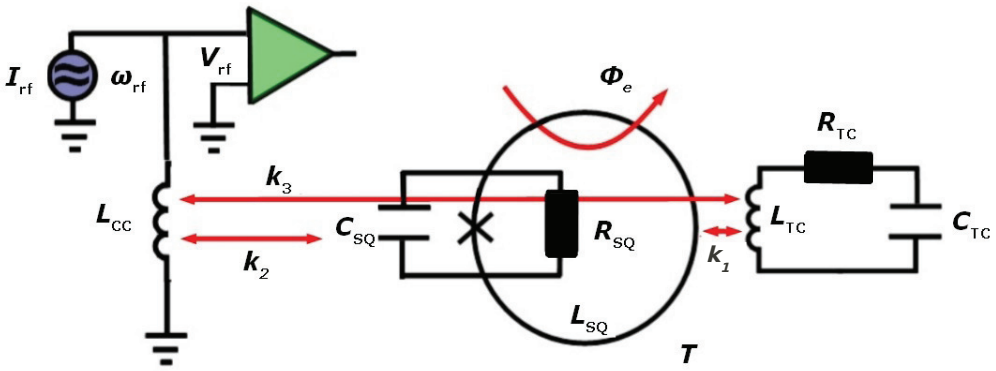

Figure 5: Schematic circuit diagram of the rf SQUID with important parameters and magnetic relations in red. Coupling coil (left), SQUID (middle), tank circuit (right). Parameters are discussed in the text.

First for the junction of the SQUID the model of the resistive-capacitive shunted junction (RCSJ model) is commonly used where the Josephson junction is in parallel with its self-capacitance C_{SQ} and a resistance R_{SQ} [Stewart 1968], [McCumber 1968].

To explain hysteretic operation, this model is not absolutely mandatory. Here the parameter

(10) $$\tau = \frac{L_{SQ}}{R_{SQ}}$$

denotes the time for the quantum transition required to be known for selecting the frequency ω_{rf}. For the dependence of the inner flux on the outer flux the Josephson conditions mentioned in the previous section apply. Second the tank circuit can be modelled by an LCR–circuit with resonance frequency

(11) $$\omega_0 = \frac{1}{2\pi\sqrt{L_{TC}C_{TC}}}$$

It dissipates energy due to the resistance R and radiative losses. The quality factor of the circuit

(12) $$Q = \frac{\omega_0}{2\pi\ BW}$$

with the resonating frequency ω_0 and the bandwidth BW, describes the resonating capability of the tank circuit – the ratio of stored to dissipated energy.

The coupling constants k_1 - k_3 determine the mutual inductances of the three elements and depend on geometrical parameters. The circuit is coupled inductively via k_3 to the coupling coil. If a current I_{rf} is fed in the coupling coil, a voltage V_{rf} is generated over the impedance L_{CC}. At the same time, due to k_3 and L_{TC}, a voltage is produced across the circuit which is highest at the resonance frequency ω_0 because the impedance of the circuit is highest in this case. In resonance, the circuit generates a relatively high reactive current. The reactive current – via k_3, L_{TC} and L_{CC} – contributes to V_{rf} in the coupling coil. The stored energy – in the hysteretic case - or the inductance L_{TC} of the SQUID – in the non-hysteretic case – is modified via k_1 by the SQUID depending on the flux Φ_e as will be explained.

Third the coupling coil with inductance L_{CC} as already explained is operated with a distinct current I_{rf}. The voltage V_{rf} is produced by the reactive current in the tank circuit by inductive

coupling via k_3 and amplified making use of the lock-in principle. In this way the coil is inductively coupled to the inductance L_{TC} of tank circuit via k_3 but also to the SQUID via k_2. The coupling to the SQUID is necessary to lock the flux of the SQUID to a constant value via a feedback-controlled DC current I_c, thus enabling a null-detector of magnetic flux.

Coupling coil, SQUID and tank circuit make use of the frequently applied principle in sensor technology to operate a component in resonance and disturb it by the quantity to be measured.

At hysteretic operation, a SQUID producing flux jumps (blue curve in Figure 2) due to high $2\pi L_{SQ} I_c / \Phi_0$ is chosen. The reactive current of the tank circuit increases until the critical flux of the SQUID is reached and the energy in the tank circuit is dissipated. The voltage V_{rf} drops and is reinforced only after further loading of the tank circuit over many cycles by I_{rf}. If I_{rf} is increased only the number of cycles is reduced but not the averaged voltage V_{rf} – the plateaus visible in Figure 6. V_{rf} depends more on the magnitude of Φ_e because depending on Φ_e the critical flux Φ_c is reached for different current values - in Figure 6 this is shown for I_A and I_B.

This leads to a triangular voltage-to-flux function clearly observed for one of the SQUIDs (SQUID III) during experiments. A derivation of these relations and of the transfer function [Clarke 2004]

(13) $$\frac{\partial V_{rf}}{\partial \Phi} = \frac{\omega_0}{k_1}\left(\frac{L_{TC}}{L_{SQ}}\right)^{1/2}$$

is contained in section “Proofs and Derivations”.

The maximum value the voltage in the tank circuit can amount to for a particular flux in the SQUID is inversely proportional to the coupling constant k_1 – thus k_1 should be as small as possible. On the other hand

(14) $$k_1^2 Q \geq \pi/2$$

derived in “Proofs and Derivations” has to be fulfilled for correct operation. These requirements are satisfied for a low k_1 and a high Q. In the case of non-hysteretic operation, the SQUID acts via k_1 as flux-sensitive modifier of the inductance L_{TC} of the tank circuit. Depending on Φ_e, the

resonance frequency ω_0 is “detuned”. The voltage V_{rf} is reduced. A theory developed by [Chesca 1997] for HTS rf SQUIDs yielded very a good experimental agreement. This theory will not be developed further, because non-hysteretic voltage-to-flux curves were observed only during testing of SQUIDs and not during experiments.

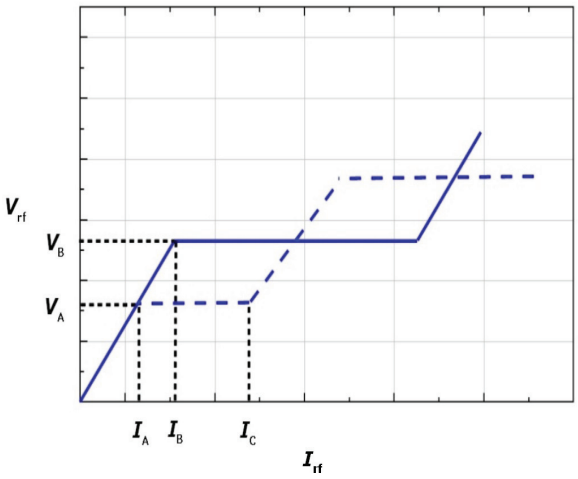

Figure 6: Dependence of voltage V_{rf} on current I_{rf} for zero outer field (solid line) and an outer field of $\Phi_0/2$ (dashed line). Discussion in the text.

No theory for the noise of the hysteretic rf SQUID with large thermal fluctuations at 77 K confirmed by experiment has been found. In addition it was not the most important aim of this thesis to optimize the system for lowest possible noise. Therefore the next items discuss those topics of system noise which were important during the construction process for acceptable noise levels:

- the noise of the SQUID itself, of the tank circuit, of the preamplifier and of the environment can be distinguished
- the thermal noise of the SQUID and the tank circuit at 77 K is approx. 20 times higher than the noise at the temperatures of liquid helium
- at the high radio-frequencies used - up to 900 MHz – the noise of the preamplifier has to be optimized with respect to the input impedance [Mück 2000]

- for higher inductances of the gradiometers, the noise levels are increased and are higher than those of conventional magnetometers due to the additional slit inductance [Zhang 1997]

- the noise of the environment is considerably lowered by the gradiometric approach thus making unshielded operation possible.

Table 1: Noise contributions.

Type	Origin	Reduction
thermal noise	preamplifier (SQUID electronics) tank circuit SQUID	low temperature optimum inductance of SQUID optimal coupling and input impedance
environmental noise	power line disturbances earth's magnetic field	soft magnetic shielding gradiometry

Evidently operating rf SQUIDs means handling a system with many parameters. The following table sums up important parameters of the SQUID's circuitry, which allow trimming for optimization purposes.

Table 2: Important parameters for SQUID operation.

Parameter	Effects on	Typical value
inductance of SQUID L_{SQ}	thermal noise, operation mode (hysteretic or not), quantum transition time	400 pH [Zhang 1997]
critical current I_c	operation mode	2 μA [Zeng 2000]
resistance R_{SQ}	thermal noise, quantum transition time	12 Ω [Zeng 2000]
resonance frequency ω_0	transfer function	800 MHz
coupling constant k_1	transfer function, condition $k_1^2 Q$	not determined
quality factor Q	condition $k_1^2 Q$	60
gradiometer balance	environmental noise	0.1 % [Zhang 1997]

2.2.5 State-of-the-Art SQUIDs and Instruments

In addition to the sensitivity, important parameters of a magnetic sensor are costs, ease of handling and its dimensions. A review of highly sensitive magnetometers is presented in [Robbes 2006]. The following table gives an overview of magnetic sensors. The device used in this thesis makes use of planar HTS rf SQUID gradiometers as described in [Zhang 1997]. The sensor is patterned from a 200 nm thick layer of YBCO by pulsed laser deposition. The step edges for the junction are etched by argon ion milling of the lanthanum aluminate substrates. A review of HTS SQUIDs is given in [Koelle 1999] and [Yang 2008], presenting sensors with field sensitivities of 10 $fT/Hz^{1/2}$ at 1 kHz with an integrated multiturn input coil. As resonating elements of rf SQUIDs, conventional tank circuits can be used, as done in this thesis, but for standard magnetometers, a superconducting microstrip resonator or a coplanar substrate resonator could also be chosen [Mück 2000]. A dielectric resonator, made for example of rutile, is possible as well.

Basics and applications of SQUID instruments are presented by [Fagaly 2006]: Magnetotellurics, rock magnetometry, nondestructive testing of materials, magnetic microscopy, magnetic immunoassays or biomagnetic applications presented in [Sternickel 2006] and [Yang 2006a] like magnetoencephalography or magnetocardiography.

Table 3: Magnetic sensors available today.

Sensor	Principle	Costs and handling	Sensitivity is proportional to	Order of sensitivity for cm-scale sensor
inductive	induction	low	frequency, area, windings	approx. 10 $pT/Hz^{1/2}$ at 100 Hz p. 215 [Göpel 1989]
Hall	Hall effect	low	width/length	0.3 $nT/Hz^{1/2}$ [Kleinpenning 1983]
magnetoresistive	magnetoresistance	medium	≈ $(width/length)^{1/2}$ [Pannetier 2005]	12 $pT/Hz^{1/2}$ [He 2009]
fluxgate	harmonic core magnetization	low	windings and area of second coil and other factors [Hinnrichs 2001]	1 $pT/Hz^{1/2}$ [Hinnrichs 2001]
HTS SQUID	Josephson effect	high	area	10 $fT/Hz^{1/2}$ [Yang 2008]
SERF	spin exchange collisions	high	-	0.5 $fT/Hz^{1/2}$ [Kominis 2003]

“Microscopic” SQUID-instruments – reviewed in [Kirtley 2002] - with high spatial resolution and minimal space between sensor and sample are the predecessors of our instrument. Such a device was first realized with a cooled sample [Buchanan 1989]. An HTS SQUID microscope for samples at room temperature with a layout similar to the device presented is shown in [Morgan 1995] and in [Lee 1996]. Since then, many similar constructions have been developed - some with a soft magnetic flux guide - see for example [Dechert 1999], [Gudoshnikov 2002], [Itozaki 2003], [Matthews 2003] or [Hayashi 2005].

Table 4: HTS SQUID gradiometers used for liquid phase magnetic immunoassays.

Type	Baseline (mm)	Sensitivity ($\Phi_0/Hz^{1/2}$)	Publication
rf SQUID	3.7	$2 \cdot 10^{-4}$	[Pretzell 2009]
dc SQUID	5	$7 \cdot 10^{-5}$	[Tsukamoto 2005]
dc SQUID	3	$5 \cdot 10^{-6}$	[Öisjöen 2008]

A SQUID instrument specially devised for readout of nanoparticles has been set up within the EU project “Biodiagnostics” with a gradiometric HTS dc-SQUID and a sapphire window [Öisjöen 2008] and by a Japanese group [Enpuku 2001]. A gradiometric SQUID microscope is also developed in [Lee 2002]. A strategy comparable to that pursued in this thesis has been used in [Carr 2007]: Here with a HTS SQUID and in parallel with a GMR sensor a samarium cobalt particle with a diameter of 100 µm is detected in a room-temperature titanium tube with an outer diameter of 1.5 mm and a sample-to-sensor distance of 2 mm. The state of our instrument without gradiometer and sample supply prior to the additions made in the course of this thesis has been described by [Schmidt 2006].

2.3 Magnetic Nanoparticles

In the next four sections, the physics of magnetic nanoparticles used in our experiments is discussed. Concerning the magnetism of magnetic colloids of this kind, only the most basic equations are discussed.

These are

- Langevin function - describes the magnetization in static fields
- relaxation equation – describes the decay of magnetization upon fast field-shutoff
- Debye's dispersion equation – describes the oscillating magnetization in AC fields

These equations express the magnetization of the particles in a most simplistic manner and disregard numerous factors. The simplifications and possible extensions will be explained and it will be checked whether they are theoretically and experimentally justified for our experiments.

2.3.1 Composition of Magnetic Nanoparticles

Magnetic nanoparticles consist of a magnetic core and a polymeric shell. Options realizing this structure are given in the following table.

Table 5: Some structural characteristics of magnetic nanoparticles.

Core structure	Core matter	Shell matter
monodomain superparamagnetic monodomain blocked ferromagnetic, multidomain (e.g. beads) multicore (core with many crystallites)	magnetite maghemite iron cobaltferrite etc.	starch carboxydextran etc.

Toxic issues of nanoparticles – which have been found - are presented by [Lewinski 2008] or [Buzea 2007] where also the natural expositions are discussed. We use small amounts of the particles in vitro.

Characteristics of the particles used in our project are presented in the annex in Table 16, Table 17 and in Figure 48. The magnetic core is made of ferromagnetic or ferrimagnetic material, which is magnetically anisotropic. The particles have a core made up of multiple crystallites, which have diameters of 12 nm in the case of FluidMAG particles [Ludwig 2009] or 5 nm and 10 nm – a bimodal distribution - in the case of the Resovist particles according to [Thünemann 2009].

To avoid sticking due to van-der-Waals forces or aligning by dipole-dipole interactions, the particles are surrounded by a polymeric shell, which generates repulsive forces if two particles approach each other. In our case the Resovist particles are stabilized by a carboxydextran shell [Reimer 2003], while the FluidMAG particles have a shell consisting of starch and are functionalized with streptavidin [Chemicell 2009].

2.3.2 Magnetism of Single Magnetic Nanoparticles

Ferrimagnetic maghemite or magnetite shows behavior similar to ferromagnetic substances. Though in ferrimagnetism the directions of the spins change, the spins of the atoms are still aligned, resulting in a large magnetization compared to paramagnetic substances.

The domains of a ferrimagnet are separated by Bloch walls. Below a certain size, magnetic nanoparticles are made up of a single domain. For larger radii the particle splits up into many domains with differently orientated magnetizations due to the resulting decrease in magnetic field energy. This effect is proportional to the volume of the particles, while the surface energy of domain walls is proportional to the surface of the particle and hence is comparatively larger for small nanoparticles - p. 12 in [Blums 1997]. In case of magnetite, the radius below which the particles are definitely single-domain, is 35.5 nm according to [Galt 1952].

The mechanism of magnetization as well as its decay depend on the sizes of the cores and whether the particles are fixed or not. Accordingly they show Néel or Brownian relaxation or both with respective relaxation times τ_N and τ_B. Brownian rotation here refers to the diffusive relaxation of the particle with hydrodynamic volume v due to random rotational movement in the fluid of viscosity η with the relaxation time

(15) $$\tau_B = \frac{3\eta v}{k T}$$

The relaxation time describing the reorientation of the inner magnetic moment with core volume v and anisotropy constant K was formulated by Néel in 1949

(16) $$\tau_N = \tau_0 e^{\frac{Kv}{kT}}$$

This law is taken from chemical kinetics formulated by Arrhenius and calculates the rate for a reaction – in this case a flip of the magnetic moment - with an energy barrier of Kv resulting in

this case from the anisotropy of the magnetic material. Experimental verification of this flip process at low temperatures for single particles with 15 - 30 nm diameter is given by [Wernsdorfer 1997]. Néel's theory was also confirmed for example by remanence measurements [Dunlop 1968].

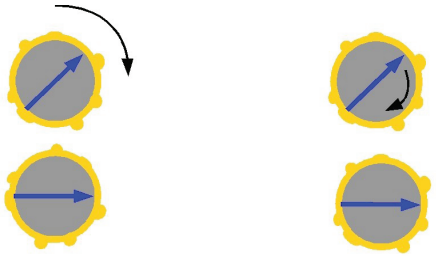

Figure 7: Scheme of Brownian (left) and Néel (right) relaxation of the magnetic moment (blue) - shown here for a particle with shell.

If both Brownian and Néel relaxation is present τ_N and τ_B combine to

(17) $$\tau_{eff} = \frac{\tau_B \tau_N}{\tau_B + \tau_N}$$

due to the addition of the rate constants.

2.3.3 Magnetism of Magnetic Fluids

In the simplest case, the magnetization of the nanoparticles follows superparamagnetic behavior – no hysteresis is observable. If the moments of the particles are rotating very fast due to the Néel mechanism, agglomeration and hysteresis of the particles is hindered and the particles are said to be superparamagnetic. If τ_N compared to the measurement time is comparatively long, the particles are said to be thermally blocked. Those particles can also be magnetized without hysteresis by the Brownian mechanism – see [Prieto Astalan 2004] for example.

The magnetization M for non-interacting particles is described by the Langevin function for paramagnetism. The magnetic moments of the particles are much higher than the single spins of the paramagnetic substance, leading to a comparatively strong magnetization M of the ferrofluid.

To describe M the Energy E of a magnetic moment $\boldsymbol{m}$ in a magnetic field $\boldsymbol{B}(\boldsymbol{r})$ is regarded

(18) $$E = -\boldsymbol{m} \cdot \boldsymbol{B}$$

It is minimized if the magnetic moment is parallel to the magnetic field. Therefore a torque aligns $\boldsymbol{m}$ and $\boldsymbol{B}(\boldsymbol{r})$. At the same time, the particles are thermally disturbed by a mean energy kT. The Langevin function L is based on the Boltzmann distribution resulting from the magnetic energies of the moments in an outer field according to equation (18) in thermal equilibrium over the unit sphere of possible positions. For the magnetization the equation

(19) $$M(B) = N m \left[\coth\left(\frac{m B}{k T} \right) - \frac{k T}{m B} \right] = N m \, \mathrm{L}\left(\frac{m B}{k T} \right)$$

holds and is derived in the annex.

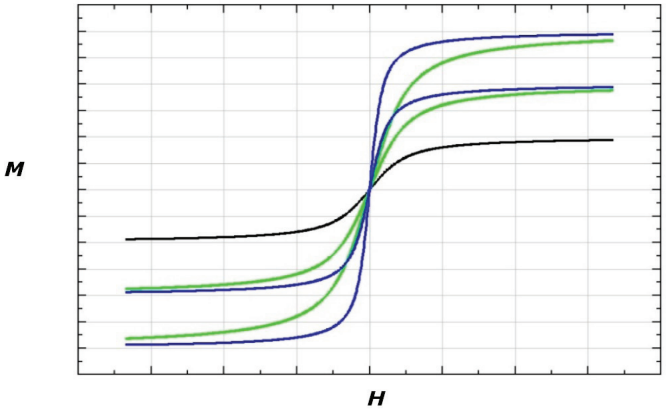

Figure 8: Graph of the Langevin magnetization curve. Magnetization M versus magnetic field H (black), same concentrations, particles with higher magnetic moments (blue), same particles , higher concentrations (green).

What are the essentials of this equation?

- The initial magnetization is linear, allowing to attribute a magnetic susceptibility χ.
- The magnetization is saturated for high field strengths, when all magnetic moments are parallel to the field at a level depending on the sum of all magnetic moments.
- The steepness of the initial magnetization curve depends on concentration, temperature and the magnitude of the magnetic moments.

The simplifications made in this law are the disregard of interactions and the assumption that the magnetic moments of the particles are monodisperse, without any size distribution. The effect of the energy barrier $k\nu$ of unblocked Néel particles in this context depends on its magnitude relative to kT and $\boldsymbol{m}\cdot\boldsymbol{B}$ and might contribute to the numerator in L.

Concerning the particle-particle interaction, the field $\boldsymbol{B}(\boldsymbol{r})$ of a magnetic moment $\boldsymbol{m}$ can be calculated according to

(20) $$\boldsymbol{B}(\boldsymbol{r}) = \frac{\mu_0}{4\pi}\left[\frac{3(\boldsymbol{r}\cdot\boldsymbol{m})\boldsymbol{r}}{r^5} - \frac{\boldsymbol{m}}{r^3}\right]$$

The field sensed by a neighboring particle decreases with the distance to the power of three.

In a first approximation, ferrofluids with particle-particle interaction are modeled by the “mean effective field model” - p. 48 in [Blum 1997]. Accordingly, a magnetic dipole in the liquid experiences the macroscopic field and a local field proportional to the magnetization $\boldsymbol{M}$ is produced by the particles themselves. Thus the following equation for the initial magnetization holds

(21) $$\boldsymbol{M} = \chi_0(\boldsymbol{H} + \lambda\boldsymbol{M})$$

where χ_0 is the susceptibility of the non-interacting colloid. For our measurements we can briefly compare the field produced by a tenfold diluted colloid of FluidMAG particles. According to the Figure 48 in the section “Physical Data”, we can calculate the field of the magnetization: For a field of 0.5 mT and without demagnetization factor it amounts roughly to 6 µT - approximately 1 % of the main field - and can therefore be disregarded.

The tendency of the particles to agglomerate or to build chains depends on many factors, such as the shells of the particles and the strengths of their magnetic moments for dipole-dipole interactions, applied magnetic fields aligning the particles, ionic interactions and so forth. Agglomeration of magnetite particles with diameters of 7 nm and 10 nm persistent even in dilute solutions are presented in [Eberbeck 2003], for instance.

2.3.4 Response of Magnetic Fluids to Non-Stationary Fields

In magnetorelaxometry, the particles are aligned by a magnetic field, which is shut off very quickly. For fields with $\boldsymbol{m} \cdot \boldsymbol{B} \ll \mathrm{k}T$

(22) $$M(t) = M_0 \mathrm{e}^{-\frac{t}{\tau}}$$

follows from Debye's dielectric theory.

The assumption $\boldsymbol{m} \cdot \boldsymbol{B} \ll \mathrm{k}T$ used is justified because magnetic moments of approx. 10^{-19} Am^2 and fields of approx. 0.2 mT occur, yielding a value of approx. 10^{-22} to 10^{-23} J, smaller than the respective $5 \cdot 10^{-21}$ J on the left side of the inequality.

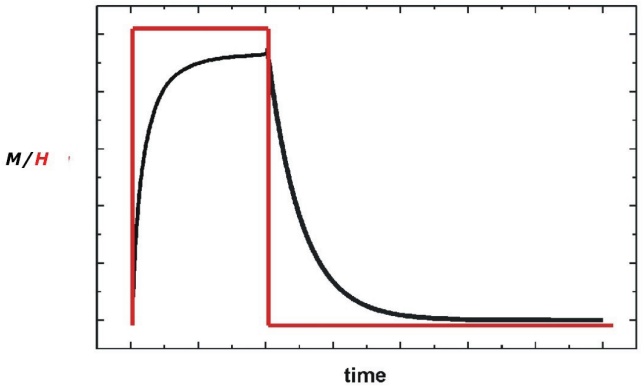

Figure 9: Graph showing relaxometry, schematically.

The relaxation according to Néel must be derived in a different manner because here a flip process governs the development. Here, as above an exponential decay of the magnetization is expected for monodisperse particles.

Considering AC susceptometry, an outer force is added, acting sinusoidally as a torque on the particle. This results in a sinusoidal magnetization with the same frequency but an additional phase lag depending on the relaxation time τ and the frequency ω. Once τ is known from relaxation, the theory can be taken from Debye's dielectric polarization as well and results in the equation

(23) $$M(t, \omega, \tau) = \chi(\omega, \tau)\ H(t)$$

with

(24) $$\chi(\omega, \tau) = \chi'(\omega, \tau) - i\chi''(\omega, \tau)$$

For a distribution of sizes always present in real fluids, the relaxation as well as the complex susceptibility for the Néel process have to be described differently. As has been shown in equation (16) the dependence of τ on the volume v of the crystallites is exponential, which leads to a very broad distribution of τ, even for a small distribution of v. This is totally different from the linear dependence of the Brownian τ on v.

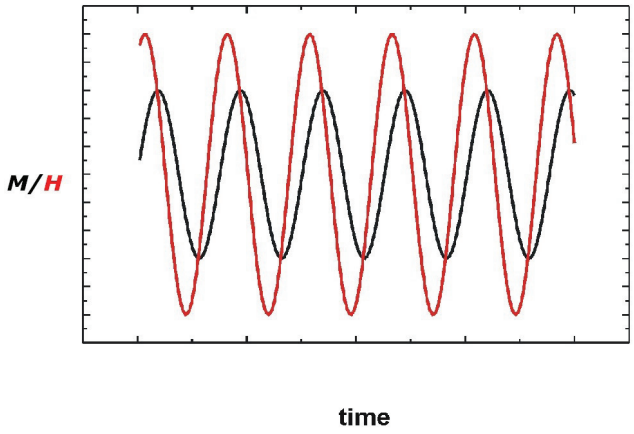

Figure 10: Graph of AC susceptometry, schematically.

This problem has to be solved by integrating the discussed expressions over the volumes v: The resulting relaxing magnetization will follow a logarithmic time dependence due to the sweep of the flip processes over time through the corresponding critical volumes of the particles [Cayless 1983], [Chantrell 1983]. Here

$$M(t) = M_0 \ln\left(1 + \frac{t_c}{t}\right) \tag{25}$$

is observed. Experiments on the relaxation of nanoparticles with a distribution of sizes have been done in [Kötitz 1999] for example and have been successfully fit to this equation.

For the formula of the complex susceptibility the same procedure of integration over the volumes is necessary [Chung 2005]. Experiments for AC susceptometry have been done by [Fannin 1986], [Fannin 1987] and [Fannin 1988] and agreed with the theory of Néel and Debye. Successful comparison of theory and experiment were also made by [Fischer 2005], who achieved reasonable results for the particle diameters, curve fit and dependence on the viscosity using an approach based on polydisperse particles. A comparison of relaxometric and susceptometric experiments is presented by [Prieto Astalan 2006]. Here the relaxation times τ obtained from relaxometry and susceptometry are comparable.

2.3.5 State-of-the-Art Biomedical Magnetic Nanoparticles

Magnetic nanoparticles like nanoparticles in general [Sahoo 2003] have a broad potential in biomedicine. For example separation, drug delivery or MRI contrast enhancement are currently being developed, as described by [Pankhurst 2003] or [Gu 2006].

Synthesis and properties of iron oxide magnetic nanoparticles are reviewed in [Lin 2006], [Horák 2007] and [Teja 2009]: Briefly, in chemical vapor composition, a carrier gas stream is delivered to a vacuum chamber to form clusters or nanoparticles. In the liquid phase, thermal decomposition of organometallic precursors such as Fe(III)acetylacetonate or hydrothermal high pressure synthesis can be applied. Two-phase approaches using microemulsions or methods with metal alkoxides in sol-gel phase are also used.

Generally the particles have a distribution of sizes that can be described well by a lognormal function. An example is shown in [Horng 2005] measured by laser scattering. A general review including the physics of iron nanoparticles is given in [Huber 2005].

2.4 Magnetic Immunoassay

2.4.1 Structure and Detection of Biological Samples

Because man does not have senses for the microscopic processes in his body or the environment, it is desirable to measure concentrations of biological matter for example by NMR or IR spectroscopy with high sensitivity in vivo or even to attain a tomographic image of these concentrations. But because the signals are too small, absorbed by the body and distorted by the collisions of the molecule in the liquid, this is not possible with state-of-the-art technology.

To overcome this problem, strategies have been devised to specifically bind targets like proteins, viruses or bacteria in vitro and subsequently detect them. This is achieved by recognizing the polymeric surface of the target substance. Binding using antibodies leads to the immunoanalytical techniques [Marquette 2006] shown in Table 6. Here as well as in the following tables, typical results are shown without claiming completeness. If the detection is realized by a transducer and electronics or optics, a biosensor has been set up [Nakamura 2003], [Nicu 2008].

Table 6: Immunoanalytics to quantify biological samples.

Method	Measured quantity	Principle	Liquid phase /labeled	Found detection limit	Publication
labeled immunoassay	diverse labels	specific binding	-+/+	varying, 1 pg/ml	p. 261 [Raem 2007]
optical biosensors	fluorescence mass refractive index	Fluorescence, SPR, interferometry, waveguide, ring resonator, optical fiber, photonic crystal	-/-	0.1 pg/mm^2 protein	[Fan 2008]
capacitive	dielectricity	capacitive	-/-	8 fM human serum albumin	[Teeparuk-sapun 2009]
mechanical biosensors	mass	cantilever, quartz crystal microbalance	-/-	100 pg/ml protein	[Fritz 2008]

2.4.2 Labeled Immunoassays

The labeled immunoassay is a subgroup of the previously mentioned techniques. Dating back to the seventies, best known and widely applied is ELISA [Voller 1978]. Apart from enzymes, many other labels can be used as indicated in Table 7 [Hempen 2006]. The table is not comprehensive - other labels are possible [Liu 2007]. Nowadays, often several label-techniques are combined, for example quantum dots and magnetic nanoparticles [Agrawal 2007] or magnetic particles and chemiluminescence [Zhao 2009]. A recent approach is the combination with microfluidics to optimize the binding with respect to efficiency and time in [Bange 2005] and [Henares 2008].

Table 7: Immunoassay strategies.

Type	Label	Found detection limit	Publication
Enzyme immunoassay	enzyme	varying, 1 pg/ml clinical	p. 261 [Raem 2007]
Fluorescence immunoassay	fluorophor	100 pg/ml	[Marquette 2006]
Magnetic immunoassay	magnetic particle	600 particles research	[Srinivasan 2009]
Quantum dot immunoassay	quantum dot	5 ng/ml research	[Zhang 2009]
Chemiluminescence immunoassay	luminescent dye	5 pg/ml research	[Zhao 2009]

For heterogeneous immunoassays, which make use of binding to a solid phase, separation and concentration of bound versus unbound substances prior to the measurement is desirable. It can be achieved for example by magnetic [Martins 2009] or chromatographic [Tang 2000] separation.

2.4.3 Diffusion, Mixing, Collision, Binding

The assay depends on the movement of the particles in the liquid and their binding. The convective motion of the particles caused by mixing or thermal misbalances has to be distinguished from diffusional movement.

The translational diffusion coefficient can be described as

(26) $$D_t = \frac{k T}{3 \pi \eta d}$$

The rotational movement has been shown to depend on the rotational diffusion coefficient

(27) $$D_r = \frac{k T}{8 \pi \eta v}$$

Correct results for the diameters according to these expressions have been verified – restricted to low viscosities – for example in [Lin 1984] using latex spheres with diameters of 20, 80, 620 and 1500 nm in polyacrylic-acid in water. These equations have been also verified in [Koenderink 2000] where the translational and rotational diffusion of 100 nm spheres in solutions with different volumetric contents of 10 nm silica host-spheres is investigated. The case is similar to our approach using magnetic particles and agarose beads in higher concentrations and shows also the limitations of the above equations in a dense matrix of particles. Magnetic particles with a diameter of approx. 100 nm and agarose beads with diameters of approx. 40 - 165 µm were used. Calculating the mean translational and rotational velocities for particles with a density of 4 g/cm^3 and varying diameters from their thermal energy kT can be illustrative. Additionally the mean square distance of translation and rotation can be calculated by using the diffusion coefficients introduced above. The results obtained are listed in Table 8. The enormous difference between the velocities shown on the left and the effective directional movement displayed on the right in Table 8 is remarkable.

The second topic of interest for this project is the collision probability of two particles as a function of their concentrations in a fluid. How long does it take until a particle finds – and binds to - its antigen? It is clear from the results given above that for binding a nanoparticle to a bead, additional mixing is mandatory, especially in dilute solutions because of the short diffusive distances of only 2 µm per second.

The mechanisms for flocculation of two substances are discussed in [Amirtharajah 1991]: Brownian diffusive flocculation, orthokinetic flocculation via velocity gradients in the bulk fluid motion and differential settling due to the collisions of larger particles with smaller, slower settling particles. Additionally the binding for real antigen applications at low concentrations in contrast to the simple approach with a biotin-streptavidin model is hindered by the requirement that after binding of the antigen to the bead, the nanoparticle has to find the point on the bead

where the antigen is located. Not every collision will end up in binding the two particles. These issues will be facilitated by a dense coating of bead and nanoparticle with antibodies.

Table 8: Thermal kinetic characteristics of spheres with various diameters and a density of 4 g/cm³ at 300 K in water.

Diameter (nm)	Mean translational velocity (m/s)	Mean angular velocity (rotations/s)	Diffusive root mean square distance per second (m)	Time for one diffusive root mean square rotation (s)
10	4	$3 \cdot 10^{8}$	$2 \cdot 10^{-5}$	$5 \cdot 10^{-6}$
50	0.4	$6 \cdot 10^{6}$	$8 \cdot 10^{-6}$	$6 \cdot 10^{-5}$
100	0.1	$8 \cdot 10^{5}$	$5 \cdot 10^{-6}$	$5 \cdot 10^{-3}$
1000	$4 \cdot 10^{-3}$	$3 \cdot 10^{3}$	$2 \cdot 10^{-6}$	5

Another important parameter of the assay is the binding of the antigen to the antibody. The forces of molecular interaction are explained by electron-electron and internuclear repulsive forces, solvophobic effects, hydrogen bonds, short-range covalent bonding forces and long-range non-covalent attractive forces [Connors 1987]. Nowadays these forces can be explored not only statistically but with single-molecule atomic force microscopy as shown in [Hinterdorfer 2006] and [Kienberger 2006]. In antigen-antibody binding events, forces in the range of 50 pN and for the biotin-streptavidin bound a few hundred pN have been found [Fritz 1997]. It is interesting to compare such values to forces acting on the particle attached to a surface or to a bead in solution while performing an assay.

The affinity of the binding of antibodies is described by the dissociation constant

(28) $$K_D = \frac{k_d}{k_a} = \frac{[A][B]}{[AB]}$$

K_D takes values for antibodies from canines in the range 10^{-7} to 10^{-11} M [Raem 2007]. The streptavidin-biotin binding of our experiments has a K_D of approx. 10^{-14} - 10^{-15} M.

Interferences have to be taken into consideration in immunoassays as well. Frequent problems are [Raem 2007]

- unspecific binding - binding to surfaces and immunoglobulines
- matrix effects – pH, ionic effects, other proteins in the solution
- cross reactivity – binding to other antigens.

The antibodies are available by polyclonal immunization of animals, monoclonal hybridoma technique, phage-display or ribosome-display [He 2002] techniques or recombinant expression in eukaryotic or prokaryotic organisms [Raem 2007].

2.4.4 Magnetic Immunoassays

Magnetic immunoassays form a subgroup of the immunoassays described above. The first question concerning the magnetic immunoassay might be: What are the advantages of this type of immunoassay? Repeating what was said in the introductory chapter one may argue that magnetic immunoassays

- can be read out in the liquid without washing steps because the particle changes its reaction to magnetic fields by binding to the antigen or larger beads
- can be read out in opaque liquids because the magnetic field is not influenced by the medium
- by applying gradient fields can be combined easily using concentration and/or separation of bound particles, thus reducing the background signal or allowing a close distance between particle and sensor.

With these properties, the magnetic immunoassay is a candidate for point-of-care testing as described in [Warsinke 2008] or for portable environmental applications. The technique dates back to 1996 [Kriz 1996] - recent realizations of magnetic immunoassays are discussed in the following section.

2.4.5 State-of-the-Art Magnetic Immunoassays

To realize a magnetic immunoassay a variety of sensors can be used – a recent overall review comprising resonant coils, Maxwell bridges, SQUIDs, GMRs and Hall sensors is given in [Tamanaha 2008]. The following table shows a spectrum with typical results.

Early attempts for magnetic immunoassays are discussed in [Kriz 1996] and [Kriz 1998], based on permeability measurements with induction coils to determine concentrations of a dextran coated ferrofluid non-specifically bound to concanavalin A. LTS SQUIDs were used in [Kötitz 1997] and [Lange 2002] using magnetorelaxometry. Magnetoresistive sensors with the aim of single molecule detection aided by magnetic beads were developed [Baselt 1998]. Also, the magnetization of nanoparticles has been measured [Enpuku 2001] as well as the remanent field [Enpuku 2003] both with HTS SQUIDs.

Strategies for measurements in the liquid phase using frequency-dependent susceptibility were introduced in [Connolly 2001]. The change of the hydrodynamic diameter after binding was further explored with AC susceptibility in [Chung 2004] and [Prieto Astalan 2004] – successfully in both cases. The liquid phase binding of magnetic nanoparticles to latex beads and the subsequent hindered relaxation was described in [Eberbeck 2005].

Table 9: Magnetic immunoassays realized by using diverse sensors and methods.

Sensor	Assay type	Sample volume	Found detection limit	Publication
inductive	solid phase frequency mixing	0.5 ml	10^4 cfu/ml bacillus Francisella tularensis	[Meyer 2007]
Hall	solid phase AC magnetization	-	one bead with 2.8 µm diameter	[Besse 2002]
spin valve magnetoresisitive	solid phase AC magnetization	100 µl	approx. 1 fM DNA	[Martins 2009]
fluxgate	liquid phase relaxometry	150 µl	14 µM	[Heim 2009]
HTS SQUID	liquid phase susceptometry	60 µl	0.3 pM	[Enpuku 2009]

The binding of nanoparticles to the relatively large fungus Candida Albicans [Enpuku 2007], to the bacterium Listeria monocytogenes [Grossman 2004] or - in sandwich mode - to polystyrene

particles [Enpuku 2009] is comparable to the approach of this thesis. Particle clustering after binding was used in [Yang 2006b] to detect binding of avidin.

In parallel, solid phase approaches have been further developed. A single magnetic bead with a diameter of 2.8 µm with a Hall sensor was detected successfully in [Besse 2002]. A Hall sensor for detection of a 1.2 µm bead was developed in [Mihajlovic 2007]. A microfluidic solid phase approach has been described [Mulvaney 2007]. Chip-technology using arrays of sensors was presented [Schotter 2009] - a review of magnetoresistive sensors for immunoassays is given in [Graham 2004], [Reiss 2005] and [Wang 2008]. Zeptomolar sensitivity for particles with diameters of only 13 nm, which show diffusive and binding characteristics different from larger µm-sized beads, is shown in [Srinivasan 2009]. It is important to note that our approach in the liquid phase cannot compete with the solid phase GMR or Hall sensor results regarding detection limits. This is because of the minute dimensions of these sensors and the resulting close distance of the particles to the sensor. In [Martins 2009], concentration of the particles by a gradient field at the solid phase prior to measurements has been realized and led to femtomolar detection of DNA .

New inductive devices have been set up, as described by [Yang 2004] and for CMOS technology by [Baglio 2005]. With frequency mixing [Paoli 1976] solid phase binding to porous filters has been applied in [Nikitin 2007] and in [Meyer 2007] with technical details explained in [Krause 2007]. A fluxgate sensor with relaxometry applied has been used in [Heim 2009].

2.5 Measurements

2.5.1 Lock-in Amplification

The technique of lock-in amplification is used twice in this system: For the preamplifier of the SQUID measuring the voltage V_{rf} and to read out the AC susceptometric measurements using a lock-in amplifier by Stanford Research Systems.

The principle there is to feed the sample a sinusoidal signal and multiply its output with a sine of same frequency as explained in “Proofs and Derivations”. Noise reduction with a factor of thousand or better is achieved.

2.5.2 The Magnetic Field of the Coils

The differential magnetic field $d\boldsymbol{B}(\boldsymbol{r})$ of a current over a length $I d\boldsymbol{l}$ that is expressed by the Biot-Savart-Law

$$d\boldsymbol{B}(\boldsymbol{r}) = \frac{\mu_0 I}{4\pi} \frac{d\boldsymbol{l} \times \boldsymbol{r}}{r^3} \tag{29}$$

With the help of this expression, it is possible to analyze the fields of many arrangements and any configurations using the finite element method. For example, the axial field of a coil having diameter d along the z-axis as a function of current I can be written in accordance with Biot-Savart

$$B(z) = \frac{\mu_0 I (d/2)^2}{2((d/2)^2 + z^2)^{3/2}} \tag{30}$$

In our set-up described in section 3.2 for two opposing coils with a distance of 26 mm, we take as mean diameter d of the voluminous coils d = 8 mm. In the middle of the two coils, an approximate axial field of 0.22 mT for a current of 28 A – for 28 windings - can be computed. For this range of field strengths the contribution of the earth's magnetic field – approx. 50 µT – to the measurements should be kept in mind but in a first approximation it is disregarded in our preliminary experiments presented in the chapter “Experiments and Results”.

2.5.3 Magnetization of the Instrument

At the end of this chapter a discussion about the magnetism of water and components of the instrument is necessary. The DC magnetic susceptibility of diamagnetic water is – 9.04 · 10^{-6}. With this value, the magnetic moment of 1 µl water, which we are sensing using the SQUID, amounts to 0.5 mT/μ_0 · 10^{-9} m^3 · 9.0 · 10^{-6} ≈ 4 · 10^{-12} Am^2. This is a high value and corresponds roughly to 10^6 - 10^7 FluidMAG particles magnetized by this field strength. It is clearly lower than the detection limit of 5 · 10^{-10} Am^2 found for our instrument however. The diamagnetic AC susceptibility of water is reported in [Tsukada 2006] and shown to increase with higher frequencies. The phase is shown to be 180° for most of the frequencies in the explored range of 50 Hz to 1.2 kHz - ionic and pH effects are excluded.

The Vespel used at the top of the dewar is also diamagnetic – see Table 19 in the annex. For PEEK no value for χ was found in the database used (Web of Science, INSPEC). Assuming a similar susceptibility like Vespel, the PEEK holder of the coils in this set-up with a volume of approx. 1 cm^3 at fields of approx. 1 mT will be magnetized to a magnetic moment of approx. 10^{-8} Am^2. This will influence the measurement and has to be minimized as will be explained at the end of this section.

Relative to diamagnetic materials the stainless steel dewar shows a high χ – approx. 0.1 in Table 19 in the annex – and has to be taken into special consideration. Assuming a stray field of the coils of approx. 1 µT at the dewar, it is magnetized to a value of approx. 0.1 A/m. No direct measurement has been performed so far but surely a source of additional stray fields is added. To avoid these difficulties, the dewar could be made of glass or glass fiber instead.

Magnetizing effects of matter apart from nanoparticles can be suppressed by using the frequency-mixing technique [Paoli 1976]. Here, only nonlinear magnetization is sensed by application of two distinct frequencies ω_1 und ω_2 and readout at $\omega_1 + \omega_2$. This technique has been applied in our lab for the inductive readout of magnetic immunoassays before [Krause 2007]. This technique is not discussed here because it cannot be applied for reasons discussed in the chapters “Experiments and Results” and “Discussion and Outlook”.

In our set-up, the stray fields mentioned are reduced by the gradiometer but due to their inhomogeneity, they cannot be cancelled entirely. The fields have to be reduced by adjusting the height of the capillary relative to the gradiometer as discussed in the chapter “Experiments and Results”. In relaxometry the signals of water and of the instrument have been subtracted.

3 Set-up

The construction will be not described in sequence but the different parts of the system are explained separately.

To allow very sensitive measurements of magnetic nanoparticles using an HTS rf SQUID, a system with nitrogen cooling must be provided as well as electronics for operation of the SQUID. Additionally, magnetizing coils with a holder and a unit for sample supply are necessary.

In contrast to conventional systems for magnetocardiography (MCG) or for non-destructive material testing, where the SQUID is operated in liquid helium or nitrogen, the SQUID has to be operated in vacuum in this case in order to permit a short sample-to-sensor distance to the room-temperature sample. Briefly, cooling is achieved by thermally connecting the SQUID via a sapphire rod to a copper tank, which is filled with liquid nitrogen. The tank is enclosed by a vacuum stainless steel dewar for insulating purposes, the nitrogen is stored in a cryostat. A specially designed specimen holder ensures the small distance of the room-temperature sample to the cooled sensor.

To prepare the device for the planned measurements with magnetic nanoparticles, the following items were integrated into the system. They are described in the following sections, together with the fundamental parts:

- non-magnetic top cover of the dewar to allow magnetizing coils to be installed
- sample supply by a glass capillary for easy supply of sample
- installation of nearby magnetizing coils for deflecting the particles
- adjustable assembly of coils and capillary in a suitable specimen holder
- design and manufacturing of tank circuits for rf-coupling and suitable plates for insertion on top of the sapphire

- additionally a complete new design and manufacturing of the sapphire for optimal thermal coupling

- manufacturing, characterization and implementation of gradiometric SQUIDs, robust against disturbances

- construction of an aluminum frame for mounting and stabilizing the instrument

- coil electronics for fast field-shutoff and LabVIEW software for readout in relaxometry

Figure 11 shows the ready-made set-up used in the end for the experiments - the respective parts described and developed in the following sections are designated by numbers.

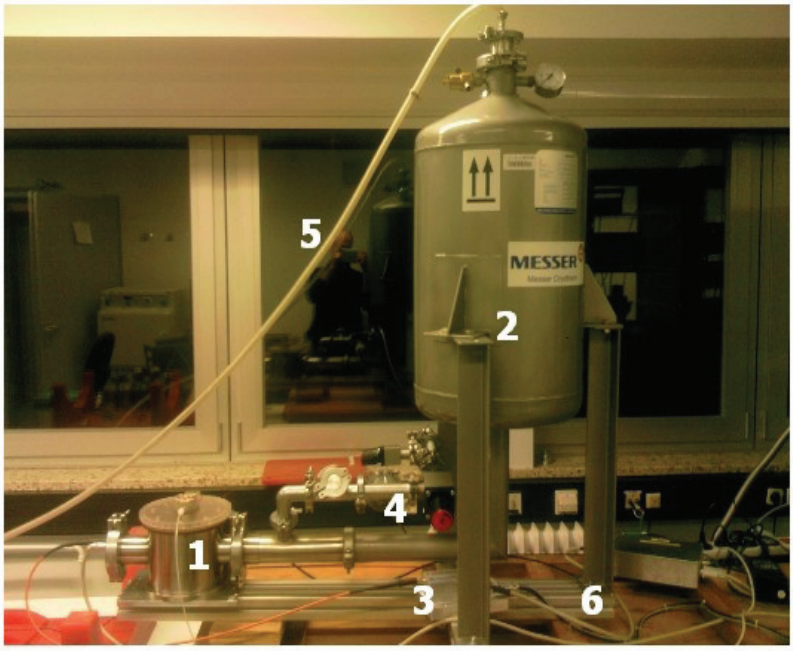

Figure 11: Picture of the set-up showing dewar with sapphire and SQUID inside (1), cryostat (2), SQUID electronics (3), vacuum gauge (4), tube for pumping the reservoir (5), mounting frame (6).

Apart from the fundamentals described in the theoretical section, the following essential parts of the system had already been developed at the beginning of the thesis:

- gradiometric HTS rf SQUID design and manufacturing [Zhang 1997]
- rf SQUID electronics for operation in flux locked loop by JSQ GmbH
- LabVIEW software for SQUID operation
- a complete SQUID microscope with a SQUID magnetometer [Schmidt 2006]

The SQUID microscope at this time consisted of the dewar with supplies made entirely of stainless steel, the cryostat, the copper tank, a sapphire finger, where a superconducting substrate resonator and SQUID magnetometer was inserted and a sapphire window. This window was in the middle of the plate on top of the dewar and served for sample supply nearby to the SQUID similar to other constructions alike presented in [Lee 1996], [Dechert 1999], [Gudoshnikov 2002], [Matthews 2003], [Sata 2003] or [Zhong 2005].

3.1 The Dewar and Copper Tank

The whole assembly of copper tank, sapphire and SQUID is positioned in a vacuum stainless steel dewar to avoid heat conduction to the outside. The copper tank as an electric conductor also shows excellent heat conduction connecting the sapphire thermally to the liquid nitrogen. The tank as well as the sapphire is mantled by multiple layers of superinsulation polyethylene foil with a thin aluminum layer to block heat radiation. Its cavern is connected to a cryostat serving as a large nitrogen reservoir by a double walled transfer line using an indium seal. The volume of the cryostat amounts to 40 liters. Figure 12 shows an AutoCAD graph of the dewar and copper tank. The top of the dewar originally consisted of stainless steel. It was replaced by a plate made of Vespel, a plastic suitable for vacuum applications, stable at different temperatures and diamagnetic. In the middle of this plate a hole has been drilled, wherein the specimen holder can be inserted. The height of the holder and thus the distance of the sample to the SQUID can be adjusted with µm-precision by turning a plastic wheel above the Vespel plate, on which the holder sits.

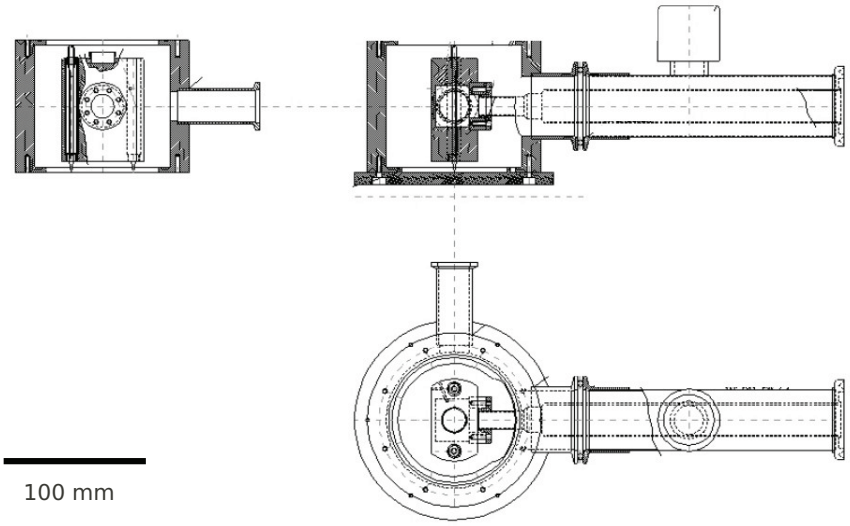

Figure 12: Overview of an AutoCAD draft of the dewar with copper tank inside and double walled transfer line for nitrogen supply. Cross sections: lateral (top), from the top (bottom).

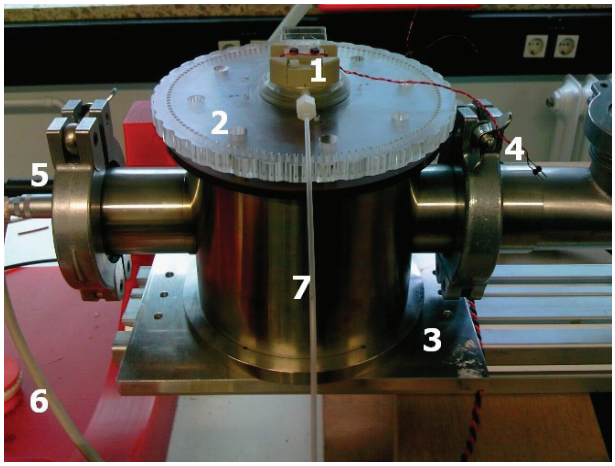

Figure 13: Picture of the dewar showing specimen holder (1), plastic wheel for adjusting the height of the holder (2), mounting plate (3), electrical connection to the coils (4), connection to the SQUID (5), connection to the Pt 100 sensor (6), tube to fill the capillary (7).

Due to the fact that the Vespel lies in direct proximity to the SQUID and magnetizing coils, magnetic and electric disturbances are to a large extent avoided. The interior of the dewar is connected to a turbomolecular vacuum pump via pipes with KF-fittings. A pressure gauge is mounted to the connection between dewar and pump. The gauge is magnetic and is mounted as far as possible from the dewar. Behind the gauge, a valve is mounted which enables the connection to the pump to be closed after evacuation, ensuring operation without disturbance from the working pump.

3.2 The Specimen Holder

3.2.1 Basic Ideas and Purpose

The sapphire window of the original construction and - as explained in the theoretical chapter - used by previous systems alike has been replaced by a specimen holder providing the following features:

- made of thermally stable polyetheretherketone (PEEK)
- option of holding the magnetizing coils in direct vicinity to the SQUID providing reduced interference with the metallic dewar
- a built-in microfluidic capillary for sample supply guided through the vacuum and thereby allowing easy liquid sample handling, close and freely adjustable sensor-to-sample-distance and expansibility (automated and/or continuous flow of samples)
- adjustability of the capillary's distance to the SQUID as well as adjustable height and angle of the coils

To fit in the Vespel plate of the dewar, the holder has four O-rings for sealing the vacuum. It was necessary to place the coils in plane with at the level of the SQUID. To do this, pockets in the holder were manufactured to allow the coils to duck under the level of the Vespel plate – see Figure 15 – imposing limits on the maximal size of the coils. The coils are wound around a removable attachment fixed to the holder with two screws made of Vespel, which is more rigid than nylon.

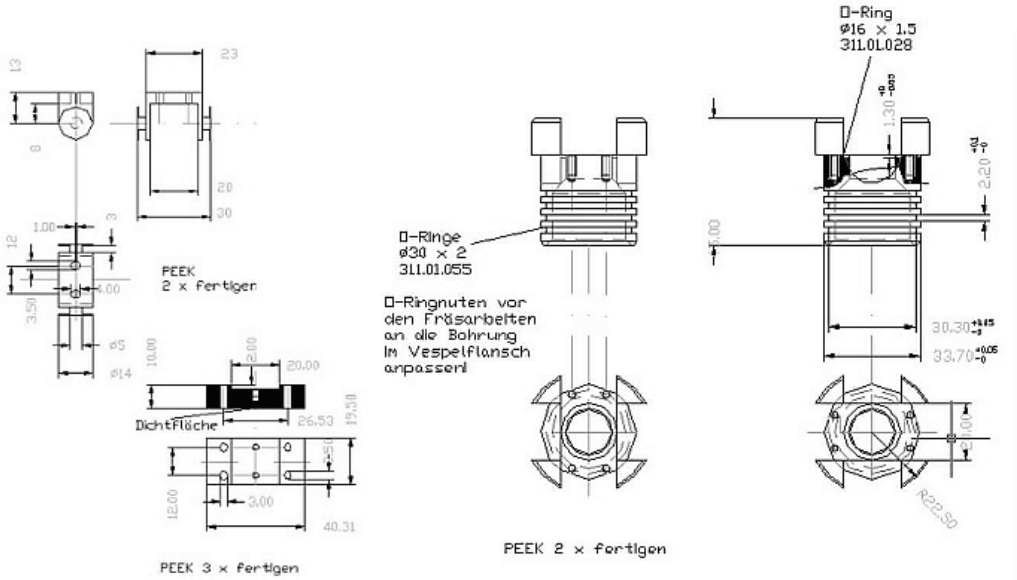

Figure 14: AutoCAD graph of the components of the specimen holder. Attachment for coil (left), block for the capillary (middle), holder (right).

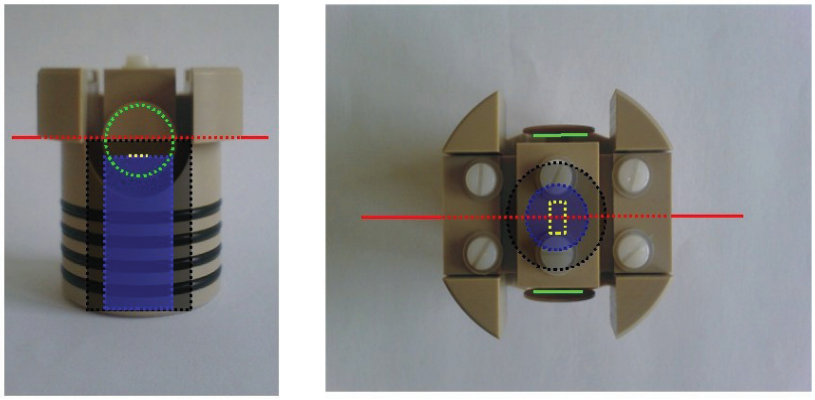

Figure 15: Pictures of the holder and in color schematically the respective parts of the system. Broken lines show hidden parts. Capillary (red), cavern for the sapphire (black), sapphire (blue), coils (green), SQUID (yellow).

3.2.2 The Coils

The coils are made of copper wire with a diameter of 0.55 mm. They are wound 28 times each around the attachment made also of PEEK and are connected to the electronics for relaxometry. For susceptometric measurements they can be connected directly to a BNC cable. For the field of such a pair of coils simple approximate analytical solutions exist as described in the theoretical section. A technical drawing of the attachment is shown on the left in Figure 14. With the formula presented in the theoretical section for a current of 28 A a field of 0.22 mT for the field in the middle of the two coils can be calculated. This refers to an injected current of 1 A.

3.2.3 Guiding of the Capillary

Capillaries with inner/outer diameters of 100/200, 400/800 and 800/1000 µm with a Luer adapter were used as sample supply.

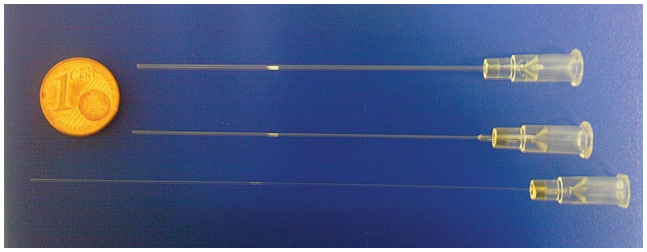

Figure 16: Picture of the capillaries used with inner diameters of 800 µm, 400 µm and 100 µm.

Initially it was planned to use a bent capillary guided through the PEEK and protruding into the vacuum close to the SQUID. This, however, did not permit diameters of the capillary of more than 200 µm. To achieve the sample-supply the capillary is guided through a groove in the PEEK block and directed to the SQUID in the middle of the block to which it is glued using two-component glue.

In principle it is possible to touch the SQUID using this configuration, which means that the smallest possible distance to the sensor is provided. Figure 17 contains a picture of the design showing the bottom of the PEEK block with the glued capillary.

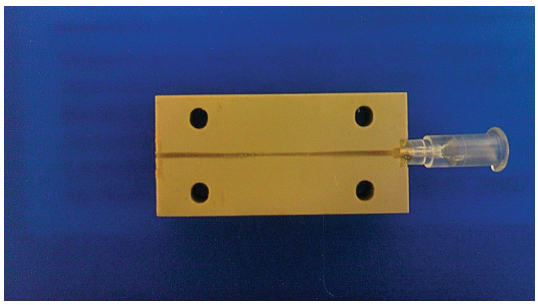

Figure 17: Picture of the first design for capillary guiding.

The disadvantage of this construction is the complicated task of adhesion and the correct sanding of the block. To allow smallest distances to the SQUID for the capillary, two slots at the sides of the capillary with a depth of 2 mm were also necessary to provide for space for the tank circuit, whose higher parts would touch the PEEK block when the wheel was lowered. The pockets were manufactured by the workshop of the Research Center. These necessities resulted in the second design of the PEEK block, as shown in the photograph below.

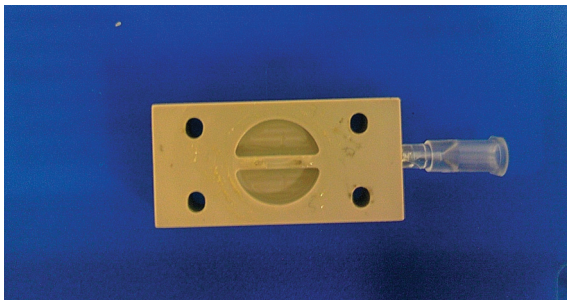

Figure 18: Picture of the second design for capillary guiding.

Now two openings for the capillary in the middle of the block prevent the need for complicated gluing and sanding. The capillary is still bent and therefore diameters above 200 µm are not possible. But using this principle and going back to an idea of a colleague [Tafhime 2006] it became evident to make use of a third design which uses a straight capillary crossing a round insertion at the bottom of the PEEK block. Based on this approach, capillaries with diameters above 200 µm become feasible. Those with inner diameters of 800 µm were used, because that would also enlarge the sample volume and signal. The design ultimately used is shown in Figure 19. The capillary is glued to the rim of the insertion.

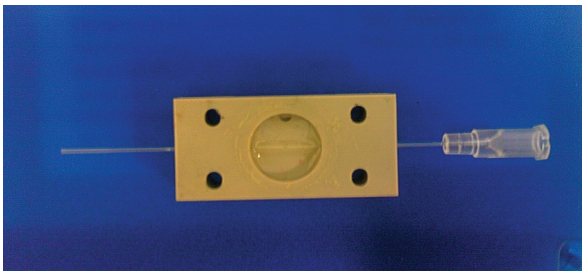

Figure 19: Picture of the third design for guiding the capillary.

Based on this configuration, the gradiometer can easily be touched by the capillary or set close to it - the protruding tank circuit arches into the insertion.

3.3 The Tank Circuit

The following features have to be provided by the rf-resonating element for gradiometric SQUID operation:

- resonance at rf-frequencies appropriate for the electronics between 500 and 900 MHz
- a sufficient quality factor, the quotient of frequency and bandwidth Δ_B at - 3dB of the peak as described in the theoretical section
- a small diameter of the coil for good coupling to the washer of the SQUID gradiometer
- attachment by a suitable plate for stable operation

3.3.1 Manufacturing of the Circuits

The principle of substrate resonators – see theoretical section - cannot be applied to gradiometric SQUIDs, because the superconducting resonator blocks the flux through the second hole of the gradiometer. Conventional tank circuits were made by hand winding a thin copper wire with a diameter of 0.15 mm two to four times around a special tool made of brass,

Figure 20: Left cross-section of the substrate resonator (purple) and gradiometer (grey): The flux (blue) can only be threaded through one hole of the gradiometer due to the shielding by the superconducting resonator. On the right the picture of the brass tool to facilitate winding the coils for the tank circuits.

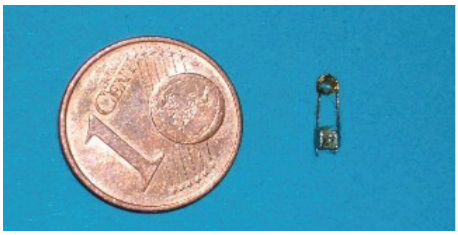

Figure 21: Picture of a typical tank circuit with coil and SMD capacitor.

which facilitated the work. Figure 20 gives an overview. Different diameters can be wound with this tool, a slit is provided to guide one end of the wire down the inside of the coil to the other end of the coil, where both ends of the wire are routed to the SMD capacitor. With appropriate practice a copper wire with suitable diameter can be used instead of the tool. The ends were

sanded down and soldered to an SMD capacitor with a capacity of 11 pF. For mounting purposes and to ensure stable operation, the circuits were inserted into a plate – see Figure 22 - which was to be placed on top of the sapphire and where the SQUID was to be placed as well.

3.3.2 Characterization of the Circuits

To characterize the circuits, the reflection was measured using a network analyzer. Measuring the reflection means measuring the response of the instrument for each frequency in a predefined range. The plates with the circuits were attached to a coupling coil using grease and the reflection was measured in air and in liquid nitrogen. Also measurements with a SQUID gradiometer on top were exercised. For the measurements, the tank circuit was connected inductively to a coupling coil. With a current flowing in the coupling coil, a voltage is induced in the tank circuit. For such an AC voltage applied to the coil and the capacitor, the impedance of the tank circuit increases steeply when the resonance frequency of the circuit is applied. If the impedance is high, the reflection measured by the network analyzer is reduced accordingly - as shown in Figure 23.

In the beginning, nine tank circuits on glass fiber substrates with the following parameters were manufactured. The reflections of the circuits were measured in air using the network analyzer. The parameters of the circuits are listed in Table 10.

Table 10: Tank circuit parameters in air and using SQUID in LN2 according to [Tafhime 2007].

Tank circuit	Number of turns	Diameter of coils (mm)	in air		in LN2 with SQUID	
			Resonance frequency (MHz)	Loss of the signal (dB)	Resonance frequency (MHz)	Loss of the signal (dB)
1	3.5	1.8	772	16	804	11
2	2.5	2	981	14	1018	10
3	3.5	1.85	798	12	838	14
4	3.5	0.8	1250	6	1261	11
5	5.5	0.8	856	5.5	876	5
6	4.5	0.8	987	7.5	1003	8.5
7	8.5	0.8	696	5	712	8
8	6.5	0.8	799	8.5	837	9
9	3.5	1.2	837	7	871	10.5

As shown in the table, the resonance frequency is higher for larger diameters and increases with the number of turns, as expected. The maximum loss at resonance and the quality factor of the circuits differ considerably, they are strongly influenced by the soldering process, presumably because of the very small capacitance of only 11 pF. The upper limit of the SQUID electronics is at 1 GHz. For better coupling to the washer of the SQUID, which has a diameter of 2 mm, a small diameter of the coil is advantageous. In summary the following statements can be made:

- a compact design of the coil - few windings and a small diameter - and a resonance sufficiently low level had to be achieved, preferably below 900 MHz

- no design rules for achieving sharp and deep resonances could be found – trial and error fabrication and subsequent testing had been envisaged

- the position of the SQUID relative to the tank circuit and coupling coil is a crucial parameter - coupling constant k is explained in the theoretical chapter – and has to be known for the reproducibility of the results and for later application inside the system

For the experiments, tank circuits with the capacitance mentioned and coils with 2½ or 3½ windings and a diameter of 1.8 mm were used.

3.4 The Sapphire Coldfinger

The sapphire is cooled by liquid nitrogen, which is thermally connected to the SQUID. Al_2O_3 is used because its thermal conductivity and dielectric constant is appropriate and that the heat is conducted via phononic rather than electronic energy transfer. Electronic conduction for example in copper would disturb the rf SQUID operation.

3.4.1 The Search for a Suitable Substrate

For fixation of the tank circuit and as a thermal conducting substrate for the SQUID, small plates for insertion into the sapphire were used initially. Different materials for the plates were explored. To avoid disturbance of gradiometric SQUID operation, the material should show good thermal conductivity, non-magnetic and non-superconducting behavior and a low dielectric constant. In the end the sapphire itself served as substrate for the SQUID, but first glass fiber, silicon and lanthanum aluminate were tested.

Glass fiber was chosen first, because of the excellent electrical properties of non-conductivity and a low dielectric constant. Unfortunately, sufficient cooling via the sapphire was not possible using a glass fiber mask with the SQUID inside the dewar. The thermal conductivity of glass fiber even in combination with conducting grease for better conduction was just not sufficient. To optimize in this respect, a highly doped silicon mask was chosen instead – see the following Figure 22.

Figure 22: Pictures of the substrate plates for the tank circuits. Glass-fiber (left), silicon (center), lanthanum aluminate (right).

Here the problem was the higher value of the dielectric constant disturbing the rf-coupling. The reflection peak was considerably diminished and broadened in comparison to glass fiber.

A plate made of lanthanum aluminate drilled by the ceramics workshop was finally chosen and better results were obtained. As an example the following graph shows the reflection peaks on lanthanum aluminate in air and in liquid nitrogen.

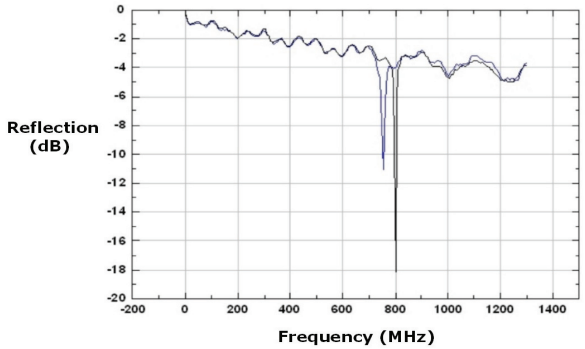

Figure 23: Graph of the reflection of a tank circuit on lanthanum aluminate plate with gradiometric SQUID (baseline 2.7 mm). In air (blue), in liquid nitrogen (black) - according to [Tabet 2006].

Numerous experiments were carried out to operate the system with the lanthanum aluminate plate. Sometimes the SQUID was lockable inside the dewar after cool-down, but not reproducibly. Due to these difficulties, the next step was a complete redesign of the sapphire to allow the gradiometer to be inserted directly into its top.

3.4.2 Redesign of the Sapphire

After it had become clear that for sufficient cooling the SQUID would have to be inserted directly into the sapphire finger, a design with pockets for the tank circuit and the SQUID was devised.

The following features were to have been provided:

- direct and good thermal coupling of the SQUID to the finger
- no electric disturbance due to the low dielectric constant of sapphire
- means of attachment, but at the same time adjustability relative to the capillary of SQUID and tank circuit
- additional pocket for the coupling coil
- channel for the cable of the coupling coil
- insertion near the top of the finger for the Pt 100 sensor for temperature sensing

An AutoCAD drawing and a schematic view of the final assembly are shown on the next page. The rough block was machined in the ceramics workshop of the Research Center. To fit the upper part of the sapphire to the holder, the diameter was reduced using a drilling machine, while the pockets were tailored by ultrasonic drilling. For this a matching driller had to be fabricated at the workshop.

The ready-made sapphire has a socket to fit in the copper tank with a diameter of 20 mm. The channel for the coupling coil supply runs through the interior part. The coupling coil is made of a loop of 1 ½ turns of copper wire, which is inserted into a recess of a depth of 1.5 mm. First only a one-winding loop had been tried, but this yielded poor results, probably due to a low

coupling constant k_3 - see theoretical chapter. The SQUID is positioned above the coil in a recess of a depth of 0.5 mm and, as mentioned above, is movable horizontally. The tank circuit is positioned above the SQUID. Using this configuration, the tank circuit is coupled to the coupling coil with in between the SQUID. The capacitor of the tank circuit is fixed onto a slit and thus movable. There is no other stabilizing element for the tank circuit, as it was provided by the substrates used before. A hole with a diameter of 2.2 mm for the Pt 100 sensor has been drilled at a height of 9.8 mm beneath the top.

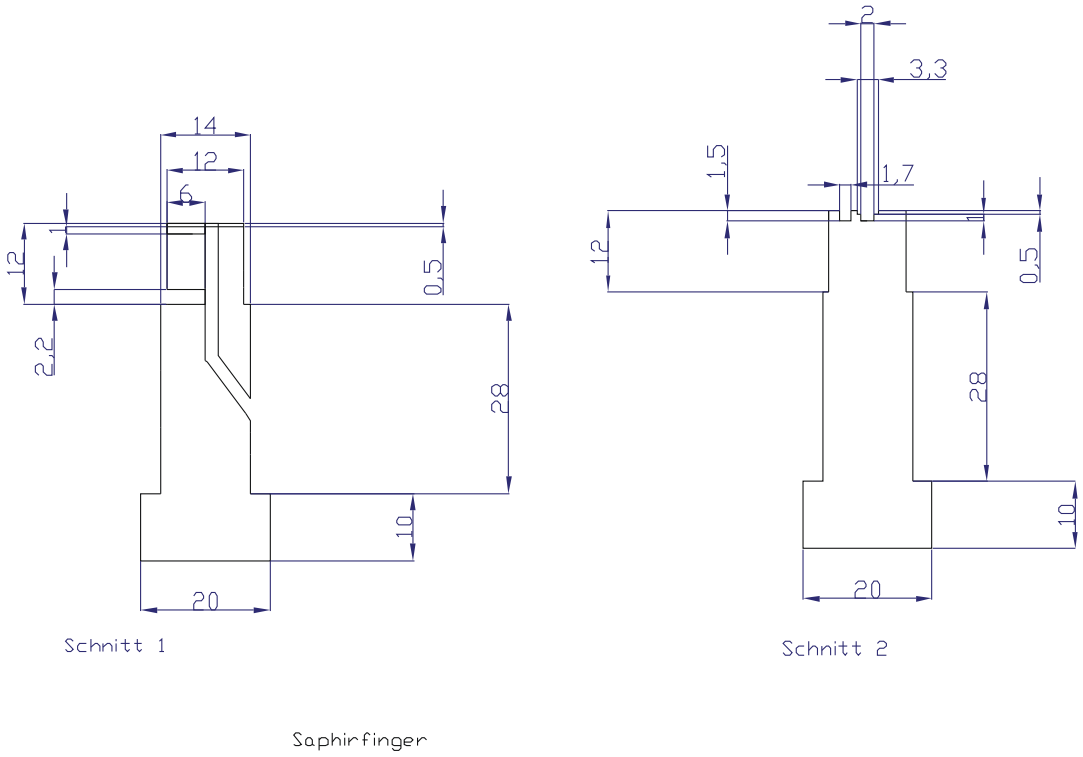

Figure 24: AutoCAD cross-sections of the sapphire.

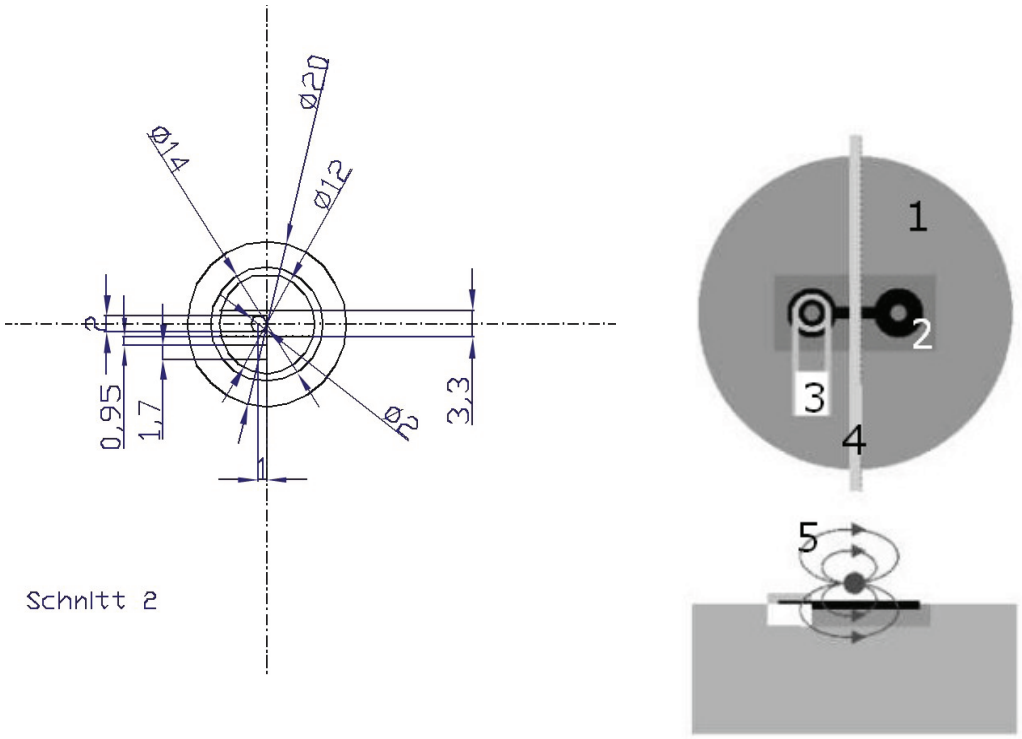

Figure 25: AutoCAD top view (left), assembly of respective parts (right). Sapphire (1), SQUID (2), tank circuit (3), capillary (4), field lines of magnetized particles inside the capillary threaded into the gradiometer (5).

The sapphire is fixed in the socket by a box nut and thermally connected to the copper block by heat conducting paste. The supply cable is grounded by connecting it to the copper block. The SQUID is fixed in the slit using vacuum grease. The Pt 100 is also fixed in its hole using vacuum grease. For operation the sapphire is mantled by multiple layers of insulation foil to reduce heat radiation.

Figure 26 shows a reflection spectrum which was measured with the sapphire totally inserted in liquid nitrogen to demonstrate proper positioning of SQUID, tank circuit and coupling coil relative to each other before operation inside the instrument.

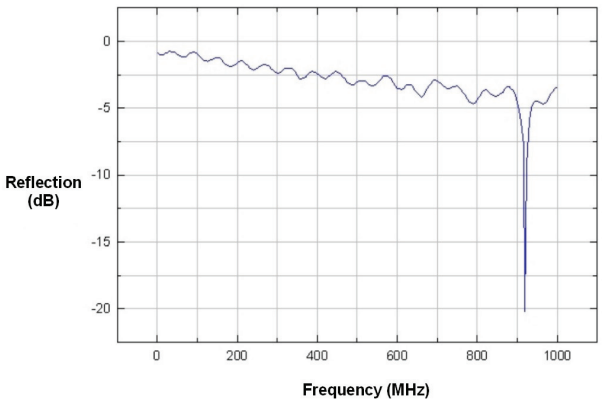

Figure 26: Reflection of tank circuit inserted in the sapphire with SQUID I in liquid nitrogen.

3.5 The SQUID

3.5.1 Testing and Choice of Functioning SQUIDs

Several batches of SQUIDs were fabricated in our institute as explained in the theoretical chapter. All were tested for operation at the temperature of liquid nitrogen. A can made of polystyrene was filled with liquid nitrogen and placed inside the shielding tube. The SQUID to be checked was mounted on a plate using a coupling coil and fixated together using a bare tank circuit by a rubber band.

For readout, a SQUID electronics by JSQ GmbH was used together with the oscilloscope and a Tiger Controller made by the Research Center for adjusting the voltage-controlled oscillator (VCO) and the voltage-controlled attenuator (VCA). A modulation signal of approx. 800 Hz by a signal generator was applied. The Tiger Controller performs a frequency scan of the VCO at a VCA value of 800. After detection of a sinusoidal signal on the oscilloscope, the VCA is varied for maximum amplitude.

The SQUIDs were checked by searching for modulation signals with acceptable noise levels. The figure below shows photographs of the modulation signals of two working SQUIDs as examples and of the rack used for testing the SQUIDs.

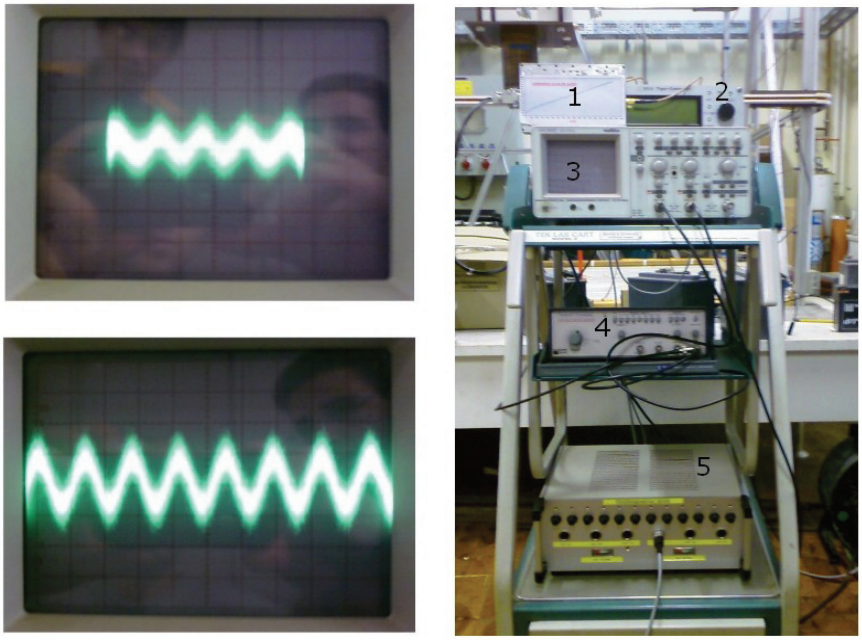

Figure 27: Left pictures of the modulation shown by the oscilloscope for inspection of SQUIDs. Weak signal (top) - barely lockable, good signal (bottom) – lockable. On the right the rack with SQUID electronics (1), Tiger Controller (2), oscilloscope (3), signal generator (4), battery (5).

Three large batches of 18 gradiometers with a baseline of 3.7 mm on 6 lanthanum aluminate substrates with a thickness of 0.5 mm each and several small batches of 6 to 12 gradiometers were tested for operation in liquid nitrogen. Usually three measurements were taken for each sensor over the course of several days to check for reproducible results.

Working SQUIDs were selected and cut using a dicing saw. Only 5 to 10 percent of the SQUIDs passed this check. Many showed no modulation signal at all. Four SQUIDs proved to be suitable for operation in the system, one of which was an old gradiometer with a base length of 2.7 mm on a substrate with a thickness of 1 mm.

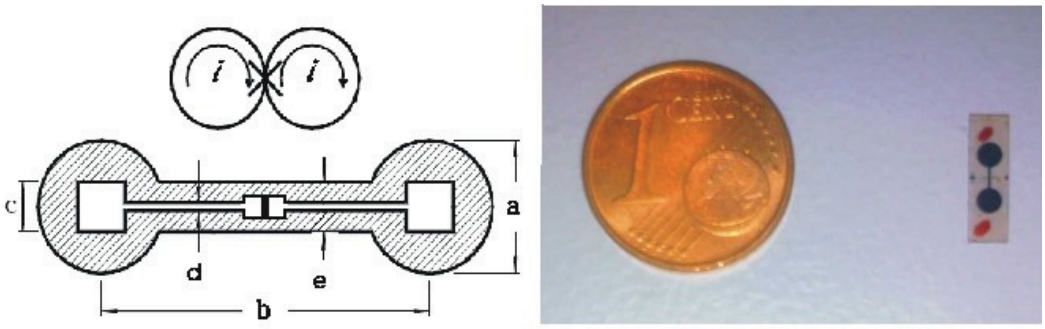

Figure 28: On the left design of the gradiometers used with direction of current at the top and layout (not to scale) at the bottom with parameters a – e and junction in black. On the right picture of the gradiometer.

Important parameters of these four SQUIDs as shown in Figure 28 are listed in the table below.

Table 11: Parameters of the four chosen SQUIDs refering to Figure 28.

SQUID	Washer diameter a (mm)	Base length b (mm)	Size of hole c (µm)	Slit width d (µm)
I	2	3.7	100	5
II	2	3.7	80	5
III	2	3.7	80	5
IV	2	2.7	50	5

3.5.2 Characterization of Gradiometric SQUIDs

The noise of the SQUIDs was measured with a spectrum analyzer inside a shielding µ-metal barrel. The white noise level was found to be approx. $2 \cdot 10^{-4}\ \Phi_0/\mathrm{Hz}^{1/2}$ – see Figure 29.

For calibration purposes, the SQUIDs are set in a magnetic field of known strength. To determine the sensitivity of the sensor, it is placed in a cage-like arrangement shown in Figure 30, which produces a homogeneous gradient.

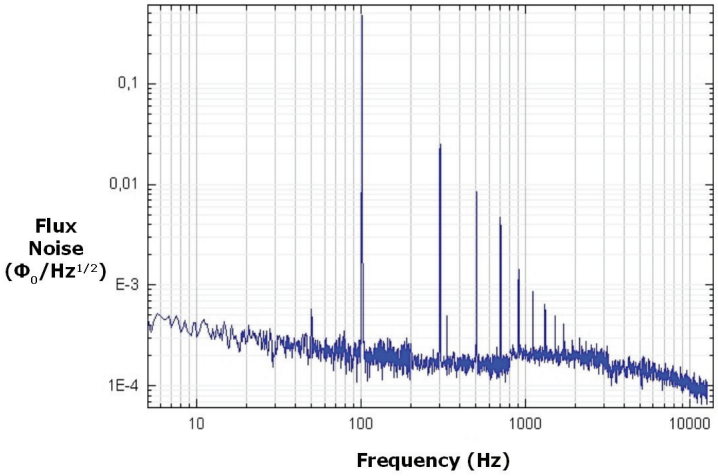

Figure 29: Graph of the spectral noise of SQUID I on circuit board in shielding barrel.

The principle of this assembly is coils on top and at the bottom with windings increasing in number of turns to the outside of the arrangement. The principle of the design is described in [Zhang 1997]. The field of the cage can be calculated or measured.

Figure 30 shows a measurement of the field with a fluxgate. The field strength for a current of 63.1 mA at 87.23 Hertz is depicted. This frequency was chosen to eliminate DC and power line disturbances.

The measuring head of the fluxgate consists of a block with cm-dimensions. The field is measured by a coil inside this block, not at a single point. The center of measurement was determined by looking for the field strength in a gradient field and turning the fluxgate by 180°. Only when measuring at the center, the measured field is inverted exactly after turning.

The center of the fluxgate was moved horizontally (x-direction) inside the cage while it was centered in y- and z-direction and then the field in z-direction was measured. The measurement was performed using a lock-in amplifier. The values were measured in steps of 1 cm. The software Origin 5.0 by Origin Lab Co. was used to perform a linear fit.

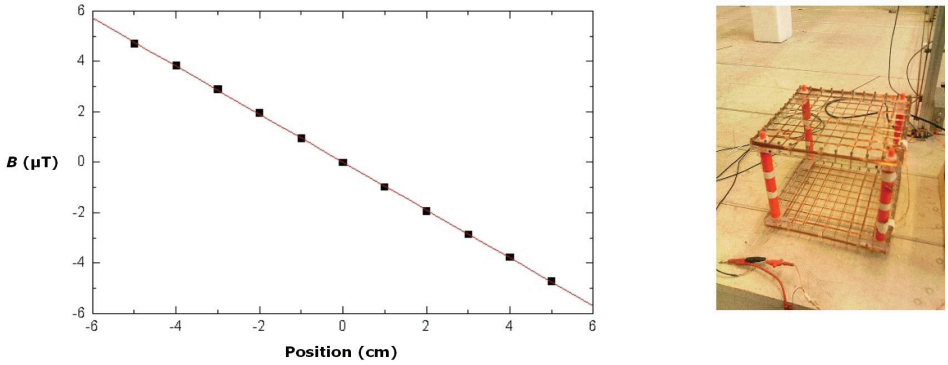

Figure 30: On the left graph of the gradient field (squares) and linear fit (red line) for a current of 63.1 mA. On the right: experimental assembly.

With this result the fit for a current of 1 A becomes

(31) $B(x)=(0.07 \pm 0.18)\ \mu T - ((15.07 \pm 0.06)\ \mu T/cm) \cdot x\ cm$

Theoretically a gradient of 1.421 mT/m can be calculated for a current of 1 A through this geometrical configuration – the fitted measurement shows a gradient of 1.507 ± 0.006 mT/m. For precise results one has to take into account the angle of the fluxgate, which might differ slightly from 90°, and the limited precision of the windings.

The voltage per flux-quantum was determined by modulating the SQUID with a saw-tooth magnetic field and evaluating the SQUID response voltage in open loop using a LabVIEW routine. The voltages displayed in Table 12 were measured for a current of 12.6 mA.

The errors of the fit and LabVIEW program (assumed to be 0.5 %) and the lock-in (1%) result in a 1.1 % percentage of inaccuracy. Based on these values a sensitivity of 4.78 ± 0.05 $(\mu T/m)/\Phi_0$ for SQUID I, 7.09 ± 0.07 $(\mu T/m)/\Phi_0$ for SQUID II, 5.81 ± 0.06 $(\mu T/m)/\Phi_0$ for SQUID III and 9.26 ± 0.09 $(\mu T/m)/\Phi_0$ for SQUID IV can be calculated. Taking the values shown in Table 13, the SQUID can be calibrated for measurements by determining the voltage difference of one flux quantum during modulation. The field gradient can be calculated by measuring the actual voltage.

Table 12: Parameters of the SQUIDs.

SQUID	Measurement	Voltage (mV)
SQUID I	voltage/flux quantum	7.30
	voltage gradient coil	28.9
SQUID II	voltage/flux quantum	9.86
	voltage gradient coil	26.4
SQUID III	voltage gradient coil	27.7
	voltage gradient coil	25.3
SQUID IV	voltage/flux quantum	13.5
	voltage gradient coil	27.7

Table 13: Sensitivities of the four SQUIDs.

SQUID	Sensitivity (μT/m)/Φ_0
I	4.78 ± 0.05
II	7.09 ± 0.07
III	5.81± 0.06
IV	9.28 ± 0.09

3.6 Shielding Tube and Mounting of the Instrument

3.6.1 Purpose and Design of the Tube

To shield from magnetic stray fields, the dewar should be set in a shielding tube made of highly permeable μ-metal. Such tubes are commonly used in magnetic shielding. A description of the physical properties of μ-metal can be found in [Vacuumschmelze 2009]. The principle is that the magnetization increases until the recurrent field inside the tube almost cancels out the outer field. Later it turned out that measurements were also possible completely without shielding. Therefore, for facilitating sample handling the tube was removed.

The tube has a length of 120 cm and a diameter of 40 cm. In the middle, a hole with a diameter of 10 cm is inserted for access to the dewar inside the tube. The thickness of the μ-metal wall of the tube amounts to 1.6 mm.

3.6.2 Determination of the Shielding Factor

To characterize the transversal and longitudinal shielding of the tube, it was placed in the center of 2 or 3 large coils with dimensions of 2 x 2 meters – see Figure 31. To imitate power line noise, a field with a frequency of 56.17 Hz and a voltage of 0.5 V was applied. The field without the tube had the strength of 302 ± 5 nT in vertical direction and a strength of 288 ± 5 nT in horizontal direction, as measured using the fluxgate. With the tube and a voltage of 5 V, magnetic fields with a strength of 13.9 ± 5 nT in vertical and 20.4 ± 5 nT in horizontal direction were found. These values result in shielding factors of around 220 in the direction of the tube's axis and around 140 in transverse direction at 56.17 Hz. The values are approximate because the magnetic fields are not homogenous over the dimensions of the tube.

Figure 31: Picture of the coil assembly for determining the tube's shielding factor.

3.6.3 Mounting the Instrument

Initially during cool down, the height of the instrument was stabilized using wooden plates. Therefore, slight movements often destroyed or worsened the vacuum. A frame made of

aluminum profiles was devised to establish a solid connection of the relatively heavy dewar to the cryostat and to avoid tensions in the pipes - Figure 11 contains a picture.

3.7 Electronics

3.7.1 SQUID Electronics

The electronics use the principle of lock-in amplifying of section 2.5.1 and operate as a null-detector in the flux-locked loop discussed in section 2.2.4. The oscillator produces the reference VCO signal I_{rf} injected into the coupling coil. In the mixer the signal of the SQUID is multiplied with the reference signal. The demodulated signal is integrated in the integrator and a feedback current I_c generates the compensating flux in the SQUID via the feedback resistor R.

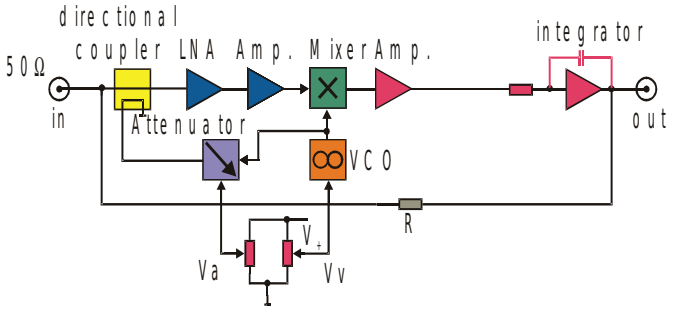

Figure 32: Schematic diagram of the electronics for SQUID operation. Explanations are provided in the text.

The speed of the compensation of the applied magnetic field is not infinite. The slew rate in our case amounts to approx. $2 \cdot 10^5$ Φ_0/s which corresponds to approx. 1 (T/m)/s for the gradiometers.

Using the newly developed electronics, it was necessary to adapt the length of the cable to the preamplifier to adjust its input impedance [Mück 2000].

3.7.2 Coil Electronics

The electronics of the coil have been devised to switch off the magnetic field as fast as possible. This is accomplished using a field effect transistor for switching and a capacitor and a resistor in parallel to the coil. This way, the high voltage across the coil during shut-off are controlled. The current for the coils is generated by a current generator.

3.8 Operation of the System

3.8.1 Evacuation

A turbomolecular pump was used to generate the vacuum. A pressure of 10^{-4} mbar is reached after one or two days in case of correct handling. The following items are important for a successful evacuation:

- elimination of leaks with the help of the leak detector
- elimination of water and dirt from inside the dewar
- gas-tight sealing of the pipes for nitrogen transfer (danger of cold leaks)
- there should be nothing inside the dewar producing vapour of any kind, e.g. unsuited plastics or glue

For leak detection, a helium leak detector has been used. Leaks at the capillary, the bottom of the dewar and other places have been found and eliminated during development of the system.

Two-component glue was used for gluing inside the dewar. As paste for the fittings and for attaching the SQUID and the Pt 100 sensor, vacuum or silicon grease was chosen.

To accelerate evacuation time a connection of the dewar to a nitrogen flask for dry ventilation was established after poor evacuation performance. In case of excess pressure, a safety valve to the outside ensures pressure balance. The evacuation performance decreases, the longer the dewar is left open.

The rubber rings of the KF-fittings were prepared with a thin coat of vacuum grease. Nevertheless, it was often difficult to establish the vacuum and the pressure decreased slowly over many days. In part this was due to water and dirt residue after the device had been open for a long time, upon ventilation with air instead of dry nitrogen and residual dirt after manipulating in the inside of the dewar. However, the main reason - found quickly by a colleague from the central technology division – was brittle rubber rings near the pump behind the Leybold valve, which had not been found by the leak detector.

Figure 33: Picture shows a brittle rubber ring of the KF-fittings – a possible contributor to leaks.

3.8.2 Cool down and Temperature Adjustment

When a pressure of around 10^{-4} mbar is reached, the valve is closed, the turbomolecular vacuum pump is shut off and liquid nitrogen is poured into the cryostat. After approximately one hour, the temperature at the sapphire stabilizes.

The Pt 100 sensor – see Figure 34 **-** is a resistor made of platinum with a resistivity of exactly 100 Ω at 0 °C. Class A devices in accordance with DIN IEC 751 and DIN 43 760 were used. The sensor is connected for a conventional four-point-measurement. It is covered with vacuum grease and inserted in a hole at the top of the sapphire – see section 3.4 for details.

By measuring the voltage across the resistance using a multimeter, the temperature T [°C] can be calculated in accordance with the equation below [Niebuhr 2002]

(32) $$R(\theta) = R_0 \, (1 + 3.908 \cdot 10^{-3} \, T - 0.580 \cdot 10^{-6} \, T^2 - 4.274 \cdot 10^{-12} \, (T\text{-}100) \, T^3)$$

For class A the precision of the sensor is ± 0.54 K at 77 K. The resistance after cool down falls down to 21 Ω corresponding to approx. 77 K. The temperature can be set to values far below 77 K using an additional vacuum pump, which is connected to the cryostat – see Figure 34. Upon pumping the nitrogen begins boiling and dissipates heat, until the boiling point of the adjusted pressure is reached. An adjustment of an attached needle valve is necessary until the desired balance of evaporation and evacuation is reached. By fine-tuning the valve, the temperature of the sapphire can be held at a nearly constant value. Nevertheless, the operation of the system is of course more complicated than nitrogen cooling at ambient pressure.

SQUID I was reliably operated based on pure nitrogen cooling. Preliminary measurements were made and it was checked whether or not the SQUID could be operated in a flux-locked loop. Probably due to repetitve warm-ups and icing, the sensor lost its reliability and had to be replaced by SQUID III. It then became necessary to employ the additional vacuum pump for temperatures below 77 K because the sensor did not work correctly on top of the sapphire. The temperature range for possible operation of the SQUID is only a few Kelvin. For these measurements SQUID III was operated at a resistance of 20.25 Ω, corresponding to a temperature of 74 K.

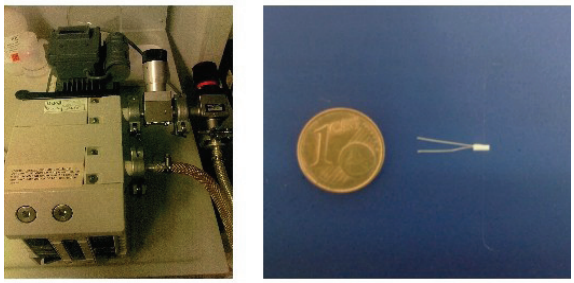

Figure 34: On the left a picture of the additional vacuum pump with needle valve, on the right Pt 100 sensor.

3.8.3 Course and Parameters for Operation

The following items summarize which parameters – shown in bold face - have to be maintained and which steps have to be followed for correct operation of the system. Some steps can be left out if a SQUID that can be operated without the additional pump is chosen.

- attachment of gradiometer and tank circuit on top of the sapphire using vacuum grease, the sapphire has to be covered using insulating foil
- attachment and tightening of the Vespel plate
- evacuation down to a pressure of **10^{-4} mbar**
- closing of the valve and shutting down the turbomolecular vacuum pump
- adding of approx. **6 liters** liquid nitrogen - for approx. 1 hour of cool down and approx. 1 day of cooling - and warm up of the second vacuum pump
- after stabilization of temperature and pressure at **10^{-5} mbar** connection of the cryostat to the second vacuum pump and - by using the needle valve - reduction and stabilization of the Pt 100 resistor to **20.25 Ω** (for SQUID III)
- setting VCO and VCA of the SQUID and testing for feasibility of flux-locked loop
- determination of the voltage per flux-quantum
- threshold value of **1 A** for the coils during measurement
- setting the height of the holder by turning the plastic wheel for minimization of the coil field transverse to the SQUID
- performance of the measurements with careful rinsing of the capillary

- after taking the measurements, the second vacuum pump has to be disconnected and the cryostat has to be ventilated

- after warm up of the system, ventilation of the dewar using nitrogen from a bottle

For convenience the following items are also worth mentioning:

- repeated cooling and warming of the SQUIDs should be avoided and the SQUIDs should be stored in liquid nitrogen

- records of every change of the running system should be taken

4 Experiments and Results

The basic preliminary experiments to explore the performance of the instrument without magnetic nanoparticles and possible assay strategies with particles are presented in this chapter. Particle measurements were carried out in the liquid in susceptometric and relaxometric mode. No statistics, error analysis or optimization of the measurement process has been done in the following experiments, which can be regarded as a first exploration of the instrument and possible strategies for readout. Detailed experiments on particles and calibrations will be conducted in the months following this thesis.

In order to determine the sensitivity, a diluted series of Resovist nanoparticles was used. These are assumed to be superparamagnetic. As a first instance, detection limits of the instrument should be explored this way. For binding experiments the following homogeneous assay strategy was explored: In a sandwich approach where the antigen binds to a magnetic nanoparticle and to an agarose bead, the Brownian relaxation is impeded and a slow Néel relaxation remains [Eberbeck 2005]. Therefore streptavidin FluidMAG nanoparticles were bound to agarose beads of various concentrations using a biotin shell imitating a sandwich assay with two antibodies and one antigen in between. The relaxation of freeze-dried versus free FluidMAG particles is shown in [Ludwig 2009] as well as their superparamagnetism.

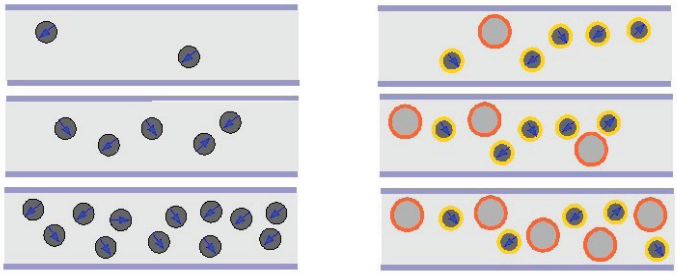

Figure 35: Sketch of the performed assay types in liquid phase. On the left increasingly concentrated magnetic particles to explore sensitivity of the instrument are depicted. On the right increasingly concentrated agarose beads with biotin shell (red), which binds to the streptavidin shell (yellow) of the magnetic particles to explore the possibility for the detection of binding, are shown.

4.1 Characterization of the Instrument

Before starting experiments on particles it is of interest to characterize the instrument by determining the noise level of the SQUID inside the instrument. Furthermore, the mechanical balance is explored by determining the minimal flux threaded through the SQUID after optimal adjustment and the stability over time is regarded. Also nonlinear behavior of the instrument was detected with increasing coil currents for different frequencies and is described below.

4.1.1 Sensitivity

The absolute spectral noise of the system was measured using the spectrum analyzer without the shielding tube. The noise is comparable to the results of SQUID I in the shielding barrel described in section 3.6.1 – approx. $2 \cdot 10^{-4}\ \Phi_0/\mathrm{Hz}^{1/2}$.

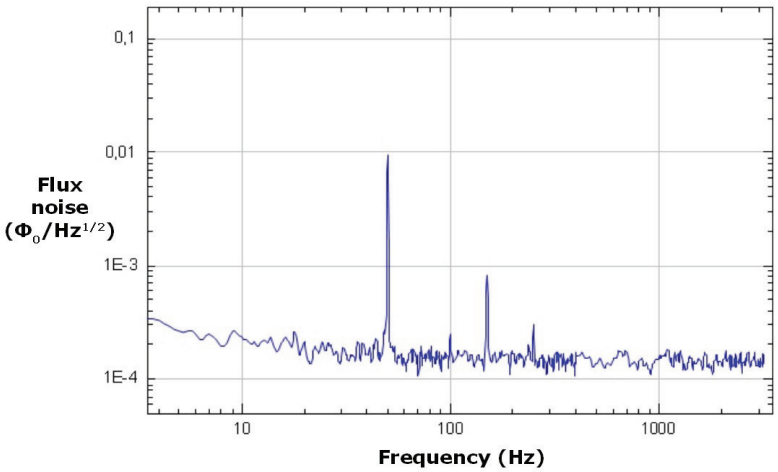

Figure 36: Graph of the spectral noise of SQUID III inside the instrument.

4.1.2 Mechanical Balance

For susceptometric measurements, the field of the coils cannot be shut off during measurement of the field of the particles as it is possible in relaxometry. Rather it has to be

minimized by setting the height of the coils to render the field at the site of the gradiometer parallel to its base, as shown in Figure 37 below. Stray fields by the components of the instrument also have to be minimized by this procedure.

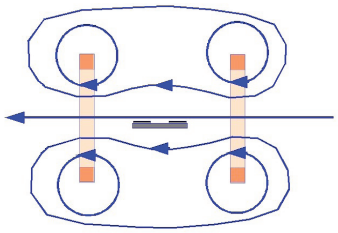

Figure 37: Schematic cross section of the SQUID (black) in plane with the axial magnetic field (blue) of the two coils (orange).

This is done by turning the plastic wheel, setting the height with micrometer precision and minimizing the amplitude in the lock-in amplifier.

For susceptometric measurements, a power amplifier is used to amplify the voltage of the lock-in amplifier. The drift of the SQUID signal was measured over a time of 12 minutes after adjusting. The graph shows the drift of the real and imaginary part relative to the phase of the coil current, which amounted to 0.2 A at 530 Hz. The measurement was conducted using SQUID III and 40 mV/(µT/m). As can be seen in Figure 38, a drift up to approx. 2.5 (nT/cm)/min for the real part of the signal is visible. This may be due to slight movements of the specimen holder relative to the sensor. The drift of the real part of the signal is much larger than the drift of the imaginary part.

4.1.3 Non-Linearity

Originally it was also intended to apply frequency mixing, but as shown below, the balance of the instrument shows nonlinear behavior especially for frequencies above 100 Hz, rendering the use of frequency mixing impossible. Measurements showed that the power amplifier with connected coils does not produce nonlinearity, also the removal of the µ-metal shielding tube, which may be easily magnetized by the coils, did not result in any positive effects. Neither the SQUID itself nor its electronics with their large dynamic range should contribute to this behavior.

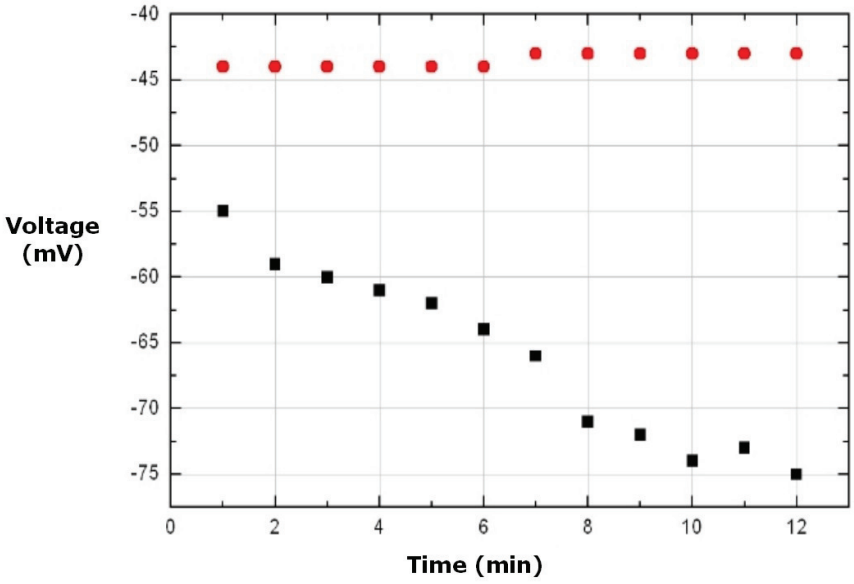

Figure 38: Graph showing the drift of the balance without particles due to movement of the coils relative to the SQUID. The phase angle is set relative to the coil current. Real part (black), imaginary part (red).

The graph in Figure 39 shows the measured nonlinearities of the imaginary amplitude for the frequencies 10, 55, 105, 265 and 530 Hz without shielding tube. A moderate current of up to 0.2 A was applied because the SQUID was not lockable for higher currents in this experiment. The measurement was done using SQUID III and at 40 mV/(μT/m).

Only the imaginary part of the signal is shown due to the large drift of the real part, as explained earlier. The graph demonstrates that even for these moderate currents below 1 A, there is non-linear behavior for higher frequencies. This effect can be attributed to the magnetization of the stainless steel dewar for large coil currents. Due to this effect, however, only measurements at a constant amplitude and frequency are feasible.

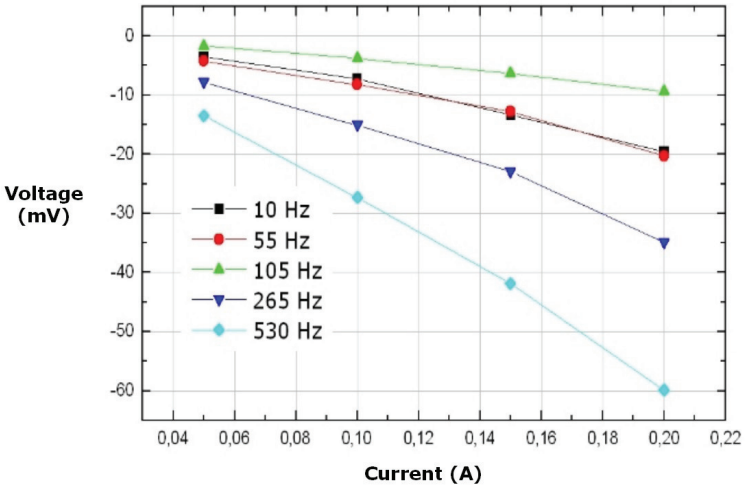

Figure 39: Graph showing the imaginary amplitude for various currents and frequencies as indicated.

4.2 Preparation of Particles

For determination of the sensitivity in susceptometry and relaxometry, we used Resovist nanoparticles for MRI contrast enhancement. Resovist is a liver-specific MRI contrast agent with the following properties [Reimer 2003]:

- consists of a polycrystalline magnetite/maghemite-core
- is coated with carboxydextran
- has a mean hydrodynamic diameter of 62 nm
- contains 0.5 mol/l iron

The lock-in amplifier was used to conduct susceptometric measurements. The power amplifier was used for the binding experiments to increase the excitation field strength. The currents were measured by determining the voltage across a resistor of 0.1 Ω.

For the binding experiments, FluidMAG nanoparticles coated with streptavidin together with agarose beads coated with biotin were used. The nanoparticles have a mean hydrodynamic diameters of approximately 100 nm and a multidomain core described in the theoretical section, with a diameter of approximately 70 nm [Chemicell 2009]. The magnetic moment of a single particle amounts to approx. 10^{-16} Am^2 in saturation according to the magnetization curve in Figure 48. The agarose beads have a mean diameter of 40 – 165 µm and a streptavidin binding capacity of 59.6 mg/ml in the delivered concentration. Further information about the particles can be found in the respective tables in the section “Physical Data”.

The beads should be washed before use to remove the solution containing dissolved biotin. To this end the procedure described below was carried out three times using 1 ml of bead solution:

- centrifugation for 3 or 5 minutes at 3000 or 5000 rpm
- removal of the supernatant containing biotin
- refill with aqua dest.

4.3 Susceptometric Measurements

4.3.1 Sensitivity Measured with Resovist

To explore the principal feasibility to measure signals of the particles, a preliminary susceptometric measurement of diluted Resovist particles was performed. The measurement was conducted using a current of 4.5 mA at 530 Hz without power amplifier. A time constant of 100 ms for the lock-in amplifier and SQUID I at 1.59 mV/(µT/m) was selected.

As expected, the graph shows a linear dependence of the complex amplitude $|z|$ with increasing concentrations – Figure 40. Concentrations of 10 µmol/ml iron can be read out easily. The absolute sensitivity can only be estimated for a current of 1 A generated by the power amplifier. For larger currents it is no longer possible to take the complex amplitude $|z|$ due to the imbalance of the system. Instead, one has to choose the value of the imaginary part y.

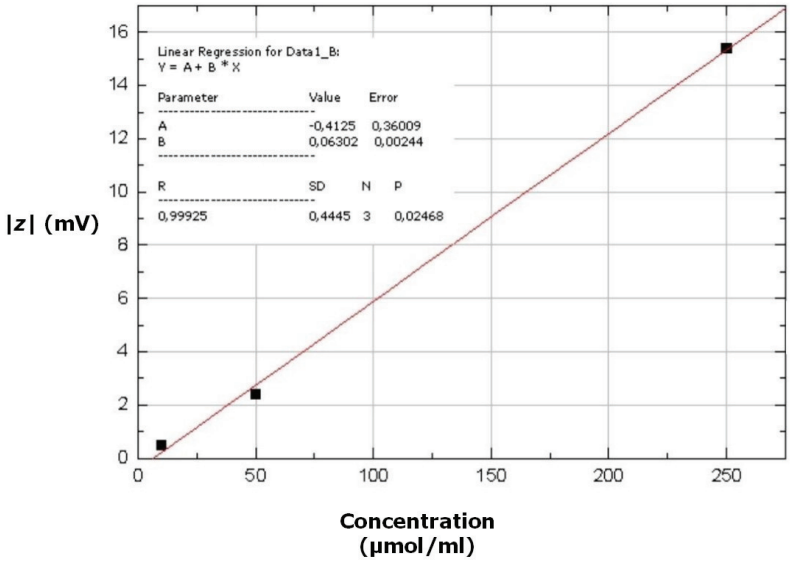

Figure 40: Graph of the complex amplitude *|z|* for different concentrations of Resovist - linear fit in red. The x-axis shows the concentration of iron.

Although *y* is considerably lower than *|z|,* this approach is chosen in the next section. This measurement was conducted to provide a first impression of the performance of the system. Additional measurements with higher coil currents and error analysis should be performed in the future.

4.3.2 Streptavidin-Biotin Binding Experiments

To test the capability of the system of determining antigen concentrations, streptavidin-coated magnetic nanoparticles diluted to a ratio strength of 1/30 were vortexed for one minute at varying concentrations of agarose beads prepared as described. The FluidMAG particles relax by the Brownian and Néel mechanism due to the dispersion of the particles' diameters in the core. The Brownian relaxation is blocked by binding to the beads and only the Néel relaxation remains – the susceptometric signal should be diminished.

The mixed solution was filled in the capillary and signals were measured at a frequency of 530 Hz and a coil current of 1 A. Measurements were performed using SQUID III with 1.57 mV/(µT/m) and a time constant of 300 ms for the lock-in amplifier.

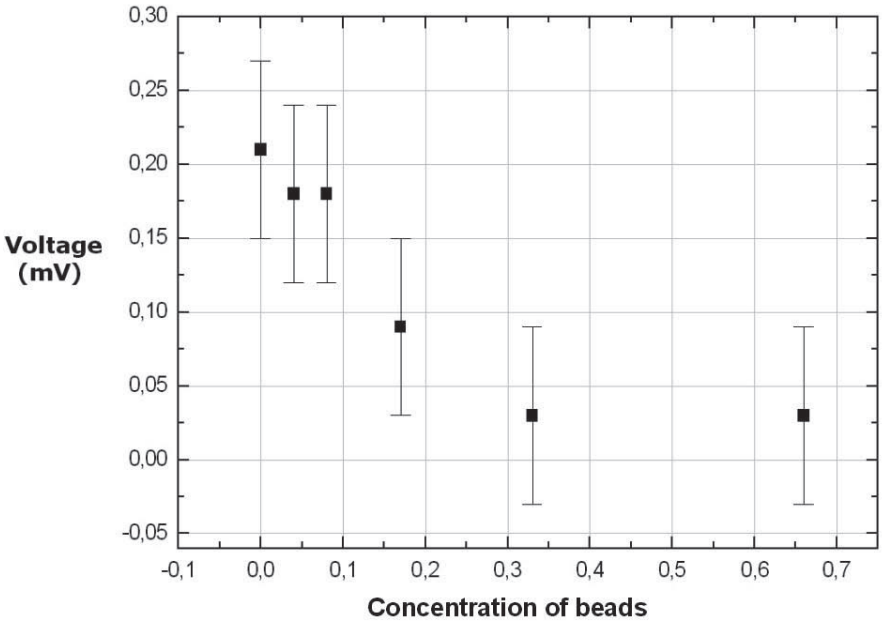

Figure 41: Graph of the imaginary part of the SQUID signal for 1/30 diluted magnetic particles with agarose beads diluted as indicated. Errors are calculated as explained in the text.

The error bars are the standard deviation calculated by taking errors in the following way: The offset was set to zero before the measurement, the measurement was performed and the capillary was rinsed, the new offset was noted and taken as error. Dilutions far beyond this value would be hardly detectable. This is due to the increasing imbalance of the system with higher coil currents.

For simplification and as prerequisite in this case, it is assumed that each particle binds to one antigen as it is the case for sufficiently low concentrations of antigen. With the chosen dilution of 1/30, one arrives at $0.6 \cdot 10^{12}$ particles per ml or a magnetic moment of approx. $5 \cdot 10^{-10}$ Am^2 at 0.2 mT field. In the volume of approx. 1 µl seen by the sensor, a detection limit of 1 fmol binding events can be calculated with this kind of method corresponding to 1 nM absolutely or to 1 µg marker.

In real applications, particles covered with primary antibodies would be added to the solution and would capture the antigen, the signal would be measured, beads with secondary antibodies would be added and capture the particles and finally signal reduction proportional to the concentration of antigens could be measured without any washing steps. Further statistical calculations seem necessary to calculate appropriate concentrations of nanoparticles, beads and antigens, reaction rates and optimal mixing procedures for real application as explained in section 2.4.3 in the theoretical chapter. Only one minute of mixing was chosen in order to enable binding to occur. Reaction rates and the time for complete binding have to be explored for future measurements and probably might lead to longer incubation times. The general feasibility of this bead-based method with our instrument has been shown here.

4.4 Relaxometric Measurements

4.4.1 Sensitivity Measured with Resovist

Just like susceptometric measurements, relaxometric experiments were also performed using Resovist particles to explore the sensitivity of the set-up. SQUID III and a newly built electronic circuit of 38 mV/(μT/m) were selected. A coil current of 1.66 A was applied for 0.5 s before shutoff. Larger currents can be applied due to their shorter durations compared with AC susceptibility. The measurements were averaged over 100 cycles.

The results can be fitted to a simple exponential decay for the first 5 ms assuming a Brownian mechanism in this time frame [Eberbeck 2009]. It is not entirely clear why the Resovist particles show a Brownian relaxation in this time frame at all - the larger core crystallites with diameters of around 10 nm might be an explanation.

The time constant τ as well as the difference Δ of the signal from 0.25 ms to 1 ms seconds can be determined using the fitting routine. The difference should be proportional to the concentration of the particles. τ should be more or less constant because the same particles were used. The curve was generated using the software Origin 5.0 with the option “Fit Exponential Decay – First Order”. The results listed in Table 14 were obtained.

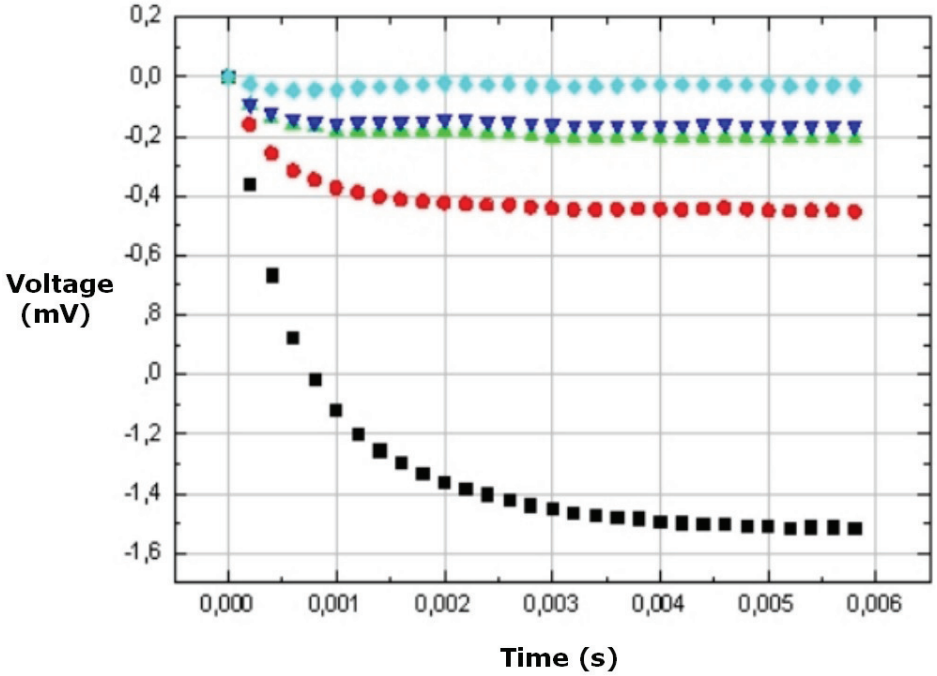

Figure 42: Graph of the relaxometric measurements using Resovist - colors refer to concentrations of iron as follows: 125 µmol/ml (black), 41 µmol/ml (red), 10 µmol/ml (green), 2.5 µmol/ml (blue), 0.6 µmol/ml (turquoise). Relaxation of water and instrument is subtracted.

Table 14: Parameters τ and Δ for the various concentrations calculated based on the results of the exponential fitting procedure.

Iron concentration (µmol/ml)	τ (s)	Δ (mV)
125	0.00075	0.67
41	0.00052	0.20
10	0.00038	0.08
2.5	0.00026	0.06
0.6	fit not possible	0.02 without fit

The table shows that Δ decreases steadily with an increasingly diluted solution, but not proportional to it. Also the parameter τ is not constant as it should be in the ideal case, but decreases for higher dilutions.

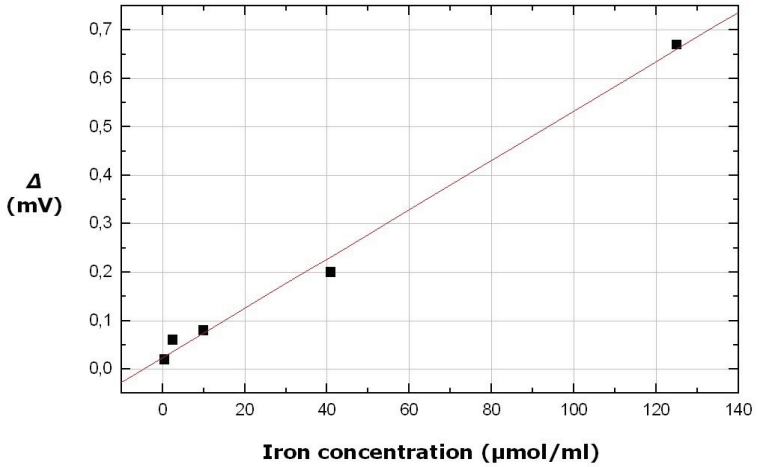

Figure 43: Signal difference Δ versus various concentrations. Linear fit shown in red.

Figure 44 shows a dilution of 1/16 with respective exponential fits. For the time frame – up to 5 ms - a first order exponential fit yields good results.

For longer times - up to 0.5 seconds – it is not adequate shown in Figure 45. Figure 45 shows that a first order exponential decay does not fit the relaxation well, especially for the first 50 milliseconds. Again it is not clear which parts of the particles relax in this time frame because there should be no magnetization present due to the Brownian relaxation shown in the graph at the top.

The purpose in conducting this experiment was to show the feasibility of concentration dependent relaxometric measurements.

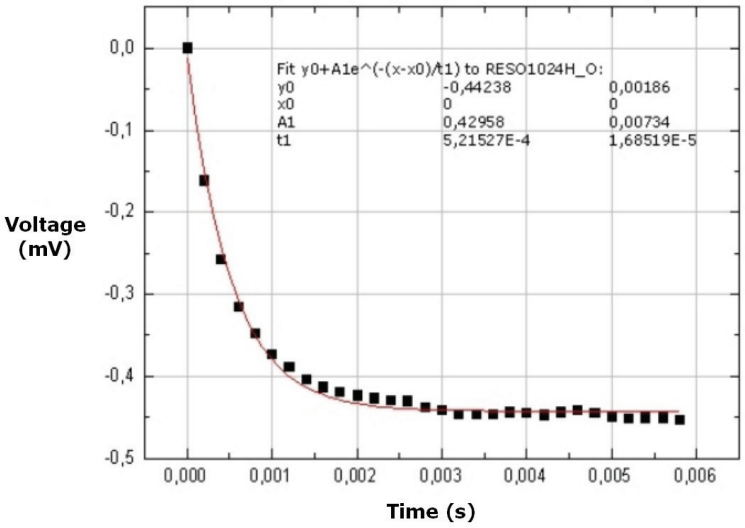

Figure 44: Graph of the Resovist relaxation at iron concentrations of 41 µmol/ml from 0 to 5 ms - exponential fit is shown in red (top).

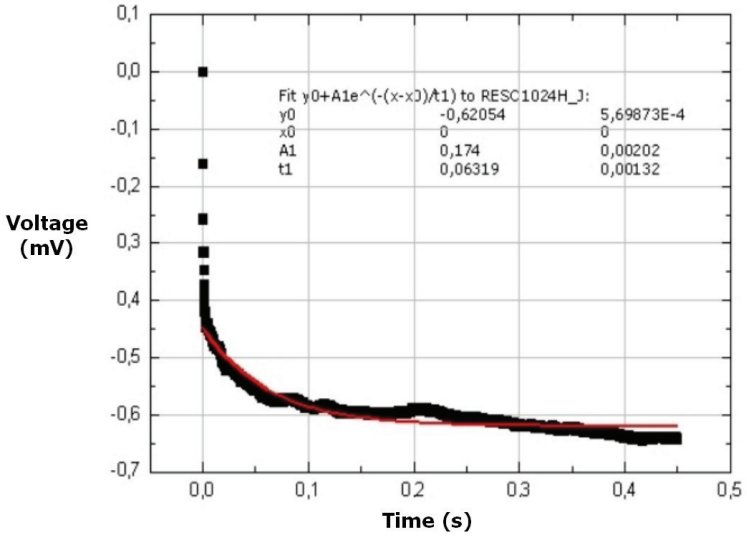

Figure 45: Graph of the Resovist relaxation with concentration 41 µmol/ml 0 to 0.5 seconds – first order exponential fit shown in red (bottom).

4.4.2 Streptavidin-Biotin Binding Experiments

For binding experiments, the same SQUID and electronic circuits used for the Resovist measurements were employed. 300 µl solution of FluidMAG nanoparticles 1/30 diluted with varying concentrations of agarose beads were vortexed for one minute. The mixed solution was filled into the capillary. Relaxometric signals were measured using SQUID III and 40 mV/(µT/m) at a current of 1.66 A.

The following graph – Figure 46 - shows the relaxation signal after subtracting the water signal from 2 to 10 ms, normalized to a starting value of 0.00. The dilution of the agarose beads is as indicated.

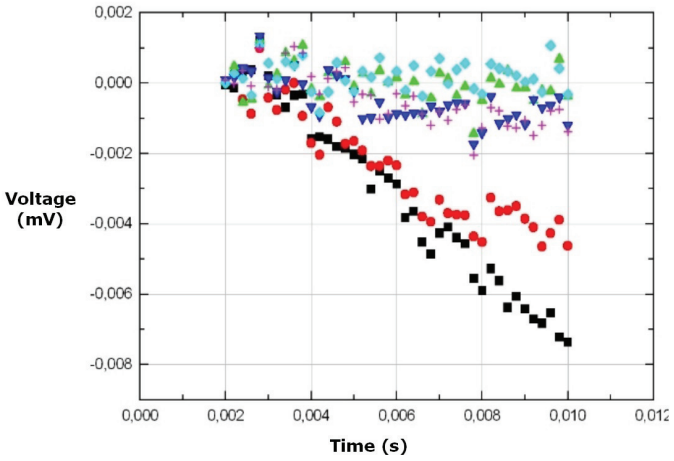

Figure 46: Graph showing the relaxation of particles diluted 1/30 after binding to beads, after subtraction of the water signal. Colors refer to dilutions of beads as follows: Only particles without beads (black), 1/24 (red), 1/12 (red), 1/6 (blue), 1/3 (turquoise), 2/3 (purple).

In the course of first two milliseconds all curves showed jumps, probably due to the flux-locked loop approaching the locking point of the SQUID. It is clearly visible that for pure particles the signal is highest. For higher concentrations of beads the relaxation is inhibited. In a measurement with beads only a signal similar to the signal of pure particles was observed without explanation.

A second measurement showed the same trend of the curves. The parameter Δ for the difference of the signal from 2 ms to 8 ms has been calculated for this measurement without fit and is displayed in Figure 47. A decrease of the shift Δ is measured for a higher concentration of beads.

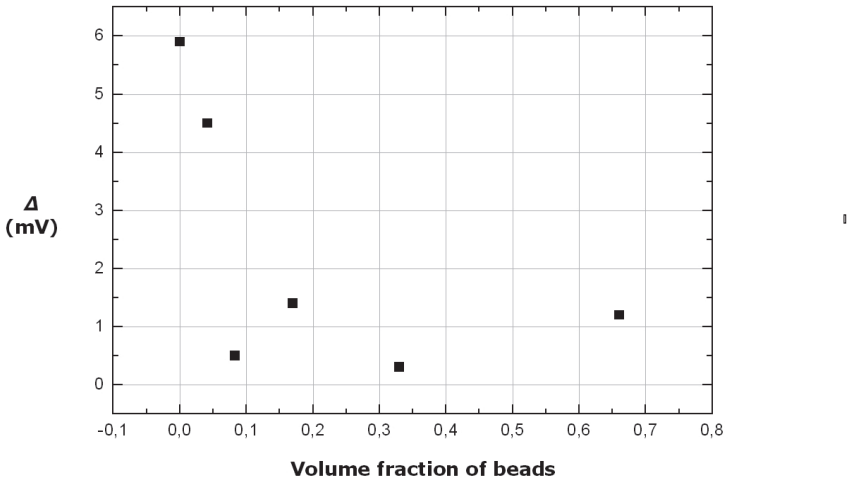

Figure 47: Graph showing parameter Δ for several dilutions of beads.

5 Discussion and Outlook

An HTS rf SQUID system for readout of magnetic nanoparticles was set up. Preliminary measurements on superparamagnetic nanoparticles – free and bound to agarose beads - have been performed. In this chapter the results of the previous chapters are summarized and compared to current research. An outlook on further experiments and an optimization of the system is given.

5.1 Discussion of the Main Results

5.1.1 Set-up

In the following table, the specifications of the system in its final state are shown including the preliminary measurements with particles.

Table 15: Specifications of the device.

Specification	Value
flux noise / sensitivity	$2 \cdot 10^{-4}\,\Phi_0/\mathrm{Hz}^{1/2}$ / 12 (pT/cm)/$\mathrm{Hz}^{1/2}$
effective area of washer	0.16 mm^2 (SQUID III)
slew rate	$2 \cdot 10^5\ \Phi_0$/s / 1 (T/m)/s
sample-to-sensor distance	0.5 - 1 mm
coil field strength	0.22 mT/A (calculated)
measured / used sample volume	approx. 1 µl / approx. 300 µl
detected magnetic moment / marker	$5 \cdot 10^{-10}$ Am^2 / 1 µg
experimentally detected binding events	$0.6 \cdot 10^9$ / 1 fmol / 1 nM

The values of this table shall are discussed briefly – in the next section the are compared to the results of other groups:

The flux noise and the sensitivity are typical for the kind of gradiometer fabricated in the Research Center. They are not as high as the values reached by HTS rf SQUID magnetometers.

The washer of the gradiometer has an effective area of 0.16 mm^2. This is a common value but much smaller than the areas reached using pick-up coils.

The slew rate of 1 (T/m)/s is sufficient for the purposes of this thesis as fields in the range of a few µT/cm or less at approx. 1 kHz are explored. Proper timing of locking the SQUID can be used to eliminate the fast shutoff of the coils.

The sample to sensor distance of typically 0.5 mm is limited by the diameter of the capillary and the washer and cannot be reduced further using the present sample volume. The strength of the field produced by the coils is sufficient for linear magnetization of the FluidMAG particles. On the other hand, using saturation at fields of approx. 0.3 T, stronger magnetization is desirable for lowering possible detection limits by three orders of magnitude or for frequency mixing.

The sample volume of 1 µl is small, allowing a short sample-to-sensor-distance and only small amount of substance. The detection limit of 1 fmol determined in the experiments conducted so far is not as good as ELISA or the results of other groups. This is also valid for the detection limit of the magnetic moment – explanations will follow in the next sections.

Answers to the questions of the introductory chapter concerning the instrument are provided below:

- How is integration of a fast room-temperature sample supply and a compact coil design achieved?

A capillary with a Luer adapter and an inner diameter of 800 µm is used, which is directed transversally through the vacuum to the SQUID. Rapid injection or continuous flow applications are possible.

The coils have a diameter of only 8 mm on average and are attached directly to the measuring head, which was inserted in the middle of the dewar's top. The angle and height of the coils relative to the SQUID are adjustable. Stray field effects such as magnetization of the dewar are minimized this way. Due to the limited size of the coils, the magnetic field cannot be increased further to arbitrarily high values. The reached field strength amount to 0.35 mT for relaxometry or 0.22 mT for susceptometry, without heating the coils.

- How can a reliable operation of a gradiometric HTS SQUID with conventional tank circuit be realized on top of a nitrogen cooled sapphire?

The SQUID and the tank circuit are inserted directly into appropriate pockets on top of the sapphire without substrate wafers. For cooling below 77 K, an additional pump adjustable by means of a needle valve is used to lower the pressure in the nitrogen cryostat. The temperature can be held constant and stable operation of the SQUID at optimum conditions is possible.

- Which steps and adjustments have to be followed to permit readout using the three techniques mentioned?

For AC susceptometry the balance of the system is important because the measurement time is comparatively long. The imaginary part of the signal shows less drift. The optimum frequency to maximize the imaginary part of the signal has to be determined. It depends on the relaxation time τ of the particles and, in case of Brownian movement, is proportional to the radius of the particle.

For relaxometry, the applied fields can be larger. Subtraction of the signal produced by water and instrument is necessary. LabVIEW routines are used to average the results. To be able to fit the results properly, the distribution of the diameters as well as the contributions of both, Brownian and Néel relaxation, should be considered. Results in [Chantrell 1983] can be used for fitting of the Néel part as explained in the theoretical section.

The instrument for frequency mixing has to be optimized further. In particular, the generation of spurious harmonics due to the nonlinearity of the stainless steel vessel has to be avoided.

Finally, for practical purposes, and to mention major problems during the construction of the device and to gain understanding of the incidents, which have been most time-consuming and have impeded progress, the following points are of interest:

The vacuum of the dewar was only stabilized after multiple leak detection and elimination, the investigation of brittle rubber rings, ventilation using dry nitrogen and repeated eliminations of cold leaks at the indium seal - a purely technical problem, but very time-consuming.

The adjustment of the temperature on top of the sapphire was a major issue: It was stabilized only after careful use of superinsulation foil and heat conducting paste, by choosing the suitable material for the substrate wafers of SQUID and tank circuit and finally by a complete redesign of the sapphire including an embedded SQUID. Employing a second pump and a needle valve for reducing and controlling the pressure in the nitrogen reservoir, the boiling temperature of the nitrogen was reduced to a temperature of the SQUID below 77 K.

Not unusual for current research, detailed descriptions of the devices set up by other groups are difficult to find doing searching the Internet. Generally, the respective publications do not provide enough detail of the realized systems to profit practically from the existing experience of other groups.

5.1.2 Experiments

Both readout techniques – relaxometry as well as AC susceptometry - yielded good results. These were performed here only for a first check of the device – without calculations and error analyses. A major drawback of susceptometry is the imbalance, which makes application of higher fields difficult. The experiments conducted so far are only preliminary, but the easy and quick preparation and supply of the sample has been demonstrated as well as the feasibility of binding experiments. Answers to the introductory questions are given below:

- Which degree of sensitivity is achievable?

Approx. 1 pmol/ml or 1 nM – using susceptometry as well as using relaxometric experiments in a first attempt. Here it is assumed that one magnetic particle corresponds to one binding event or one antigen. The detectable magnetic moment amounts to approx. $5 \cdot 10^{-10}$ Am^2, deduced from the magnetization curve of the FluidMAG particles in Figure 48 in the annex. The corresponding moment can be approximated by multiplying the magnetization with the volume of 1 µl. In this case the number of $0.6 \cdot 10^9$ particles corresponds to approx. 1 µg marker. The field of a magnetic dipole of this strength at 1 mm distance amounts to approx. 50 nT.

- Which readout method – relaxometry, AC susceptometry or frequency mixing – is most advantageous?

Both techniques applied – relaxometry and AC susceptometry – yielded good results. For relaxometry the signals proved to be not exactly proportional to the concentration. The reasons

for this should be explored in further experiments. The distinct signal for the detection of 2.5 µmol/ml iron using relaxometry is slightly better than that of the 10 µmol/ml iron with suceptometry. The difference is assumed to depend on the mechanical imbalance of the system, which does not allow nulling of the transverse field in susceptometry. Additionally the susceptometric measurement in this case was conducted without the power amplifier. Frequency mixing proved to be impossible based on the present system. The nonlinearity of the system's magnetization is too strong. Also it will be difficult to achieve the required field strengths for nonlinear magnetization of the particles used with the present coil arrangement and particles.

- Is the assay comparable to standard ELISA?

Up to now, ELISA with a typical sensitivity of 1 pg/ml equivalent to roughly – depending on the antigen - 10 fM is clearly better than the system described in this thesis. However, the preparation of the sample and ease of readout are advantageous using the SQUID system. Further optimization should be possible as will be explained in the section “Outlook”.

Again some obstacles during the course of the experiments also interesting for further projects:

No theoretical essay or paper on the possible binding strategies for magnetic immunoassays has been found yet – neither binding to beads, nor direct binding of antigens, nor enhancing the hydrodynamic diameter, nor flocculation of particles after binding in sandwich-mode or solid phase strategies. Nor do monographs or detailed reviews on magnetic immunoassays in general exist yet. The binding strategy is a very important factor for optimizing the immunoassay. This is due to the numerous possible and different approaches. It should be carefully considered apart from the device itself.

Often the signal amplitude during AC measurements decreased steadily – a possible indicator for non-superparamagnetic behavior or aggregation. Here, care has to be taken in future experiments. It was not possible to adjust the field to be completely orthogonal to the SQUID - a stray gradient of roughly 15 nT/cm for a field of 0.04 mT was observed, as shown in the chapter “Experiments and Results”. As explained, this impedes further optimization using AC susceptometry.

Additionally, the instrument shows a mechanical instability even after optimum adjustment, leading to a drift of the real part of the signal of approx. 2.5 (nT/cm)/min. It was impossible to

overcome this problem, which persists a long time after adjusting the height of the measuring head. It is complicated by the small size of the coils, which produce relatively large local inhomogeneities. The imaginary part of the particle's signal, which is orthogonal to the stray signal, was recorded in the course of the measurements. Because of these major difficulties the reported sensitivity amounts to $5 \cdot 10^{-10}$ Am^2 corresponding to a measured field strength of approx. 50 nT. As reported in Table 15, the gradiometer is able to detect gradients in the range of 10 (pT/cm)/$Hz^{1/2}$. If this instability is overcome in the future work, a substantial increase in sensitivity is to be expected.

5.2 Comparison to Systems and Results of Other Groups

As an overview, the approach of this thesis is compared to the experiments of three other groups who also detected binding of magnetic nanoparticles in the liquid phase with HTS SQUIDs.

The Swedish project partner group of Dag Winkler [Öisjöen 2008] established a HTS dc SQUID system with an excellent noise level of only 4.5 $\mu\Phi_0/Hz^{1/2}$. However, the absolute sensitivity to magnetic field gradients is only 5 times better than ours. The device is also operated unshielded, same as our instrument. For sample handling, an electro-wetting-on-dielectric positioning mechanism for the sample droplet on the sapphire window was devised. The achieved detection limit amounts to 600 pM for the streptavidin-biotin model.

The second device was built by a Taiwanese group [Yang 2006b]. An rf SQUID magnetometer with a field noise of 0.2 pT/$Hz^{1/2}$ made by the lab of our group was used in a magnetically shielded room. For magnetization purposes, fields of 0.5 mT are generated and a compensating coil provides orthogonality to the pick-up coil. The particles of 25 nm diameter are clustered by biotin-avidin binding. With relaxometry this group reaches a detection limit of 1.5 nmol/ml, corresponding to 1.5 µM for a sample volume of 3 µl.

The third approach is presented in [Enpuku 2007]. An HTS dc SQUID in a shielded environment is used and the fungus Candida albicans is detected using relaxometry. This group differentiates between bound and unbound particles by the remanence of the bound ones half a second after magnetization at high fields of up to 40 mT. The SQUID system is presented in [Enpuku 2001]. It is very sensitive and able to detect magnetic markers down to 1 ng weight for magnetizing fields in the mT range, which is approximately three orders of magnitude better than the system described in this thesis. A fungus is covered with approx. 500 particles

with a core diameter of 30 nm – in the best case 30 funghi can be detected by the system [Enpuku 2007]. This sensitivity even corresponds to approx. 2 pg magnetic marker. The stray field of this device measured when a field of 0.8 mT is applied during measurement, amounts to 1 nT using a compensation coil [Enpuku 2001].

With a value of 2 pg of magnetic marker with remanent magnetization, the approach of this group is superior to those of the others mentioned above, including the approach of this thesis, and at the moment sets the benchmark for achievable sensitivity of liquid phase immunoassays. Besides the larger magnetizing fields, the difference to our instrument is the pick-up coil used with an area of more than 10 mm^2 considerably enlarging the measured flux. Such an area is impossible to attain using our system, using only the washer of the SQUID gradiometer with an effective area according to [Ketchen 1989] of 0.16 mm^2 to catch the flux.

The further reduction of the distance to the sensor – used by the groups using Hall or GMR sensors - cannot be accomplished in the case of the system described here because of the capillary's diameter of 1 mm and due to geometrical constraints of the field lines above the flux-concentrating washer with a diameter of 2 mm.

The advantage of the measurements of this thesis compared to Enpuku's results [Enpuku 2007] is the unshielded operation and the application of AC susceptometry or – with extensions described in the last section – frequency mixing not reported by Enpuku's group so far. To test these techniques in conjunction with different assay strategies could be a target for future applications of our device.

The inductive device of our group is able to detect 10^4 cfu/ml, which is comparable to ELISA using beads with a diameter of 0.7 µm and frequency mixing [Meyer 2007].

The system described here cannot be compared to micro-sized magnetoresistive or Hall sensors. These are able to sense attomol concentrations or even single particles, which means in principle the ability to detect one single binding event. Here problems arise in positioning of the particles relatively to the minute sensor surface. Up to now, many of the publications measure particles, which have been prepared on the sensors in a complicated manner [Besse 2002], [Agrawal 2007], [Srinivasan 2009]. The sensitivity of these sensors, however, is in the range of pT and hence is comparable to the performance of the sensor described here. The recent work of Enpuku's group using a magnetoresistive sensor based on liquid phase AC susceptometry achieves a subpicomolar sensitivity with a distance of 1 mm from sample to

sensor and particles with a core diameter of 25 nm [Enpuku 2009] – a very promising approach with a commercially available sensor at room temperature.

5.3 Outlook

5.3.1 Further Measurements

The performed measurements should be repeated under optimized conditions as discussed below. As mentioned above, many possible assay strategies for magnetic nanoparticles do exist and could be explored using this instrument. The system built allows for a variety of reading methods to be tested.

The ultimate goal of determining sensitivity limits of magnetic immunoassays is better accomplished by SQUID systems equipped with pick-up coils or micrometer-sized space between sample and sensor, such as provided by Hall or GMR sensors. Though for liquid phase strategies, the SQUID system presented here is interesting because without shields it detects all kinds of fields – including slowly changing fields - measured in AC susceptometry, relaxometry, frequency mixing - with extensions - or other detection techniques like remanent magnetization of large beads. Furthermore, the device could serve for characterization of magnetic nanoparticles as well.

For liquid phase assays examined here, applications in medical or environmental diagnostics could be envisaged where a fast readout is required.

5.3.2 Possible Improvements

To optimize the system, several changes are possible and are sketched under the following items:

- The position of the capillary should be optimized relative to the SQUID – up to now the position has only roughly been estimated. A window for the application of optical control systems would be advantageous.

- The finite element method (FEM) could be applied to calculate the field of the coils and the field of the particles at the SQUID.

- The assay could be performed using different particles. If the diameter of the particle is doubled, the sensitivity will increase eightfold. Again a multicore particle would be favorable due to its shorter relaxation time.

- The diameter of the capillary could be enlarged to values beyond 1 mm. The sample volume and magnetic moment, which contributes to the signal will increase accordingly.

- The dewar could be made of glass fiber instead of stainless steel. This is the strategy applied in [Öisjöen 2008] and should result in smaller stray fields and reduced nonlinearity, maybe allowing for frequency mixing.

- Another point regarding the instrument is the strength of the magnetizing field. With 1 mT or less the particles are far from saturation. A new design of the coils for larger fields seems desirable to achieve better detection limits, but is difficult to attain due to the limited space provided by the specimen holder.

- The measurements could be extended by prior separation of unbound particles to reduce the background signal or by first collecting bound particles and then filling the capillary. The diameter of the particles could also be enlarged. The sensitivity will increase considerably by prior concentration of the particles. For example it would improve from 1 pmol/ml to 1 fmol/ml, if the particles of 1 ml solution were concentrated to the 1 µl volume, which is sensed by the SQUID gradiometer.

References

A. Agrawal, T. Sathe, S. Nie: Single-Bead Immunoassays Using Magnetic Microparticles and Spectral-Shifting Quantum Dots *Journal of Agriculture and Food Chemistry* **55** 3778−3782 2007

A. Amirtharajah, M. M. Clark, R. R. Trussel: *Mixing in Coagulation and Flocculation* Denver: American Water Works Association 1991

S. Baglio, S. Castorina, N. Savalli: Integrated Inductive Sensors for the Detection of Magnetic Microparticles *IEEE Sensors Journal* **5** No. 3 372-384 2005

A. Bange, H. B. Halsall, W. R. Heineman: Microfluidic immunosensor systems *Biosensors and Bioelectronics* **20** 2488–2503 2005

D. R. Baselt, G. U. Lee, M. Natesan, S. W. Metzger, P. E. Sheehan, R. J. Colton: A biosensor based on magnetoresistance technology *Biosensors & Bioelectronics* **13** 731–739 1998

J. G. Bednorz, K. A. Müller: Possible High T_c Superconductivity in the Ba-La-Cu-0 System *Zeitschrift für Physik B – Condensed Matter* **46** 189-193 1986

P.-A. Besse, G. Boero, M. Demierre, V. Pott, R. Popovic: Detection of a single magnetic microbead using a miniaturized silicon Hall sensor *Applied Physics Letters* **80** No. 22 4199-4201 2002

Biodiagnostics www.eu-biodiagnostics.org/Research/index.html

E. Blums, A. Cebers, M. M. Maiorov: *Magnetic Fluids* New York: de Gruyter 1997

Boedeker.com www.boedeker.com/mguide.htm

BSSA British Stainless Steel Association www.bssa.org.uk/faq.php

D. S. Buchanan, D. B. Blum, D. Crox, J. P. Wikswo : Microsquid : A Close-Spaced Four Channel Magnetometer, in: *Advances in Biomagnetism* edited by S. J. Williamson New York: Plenum Press 1989

W. Buckel, R. Kleiner: *Superconductivity Fundamentals and Applications* 2nd ed. Weinheim: Wiley-VCH 2003

C. Buzea, I. I. Pacheco, K. Robbie: Nanomaterials and nanoparticles: Sources and toxicity *Biointerphases* **2** Issue 4 17-71 2007

C. Carr, A. N. Matlachov, H. Sandin, M. A. Espy, and R. H. Kraus, Jr.: Magnetic Sensors for Bioassay: HTS SQUIDs or GMRs? *IEEE Transactions on Applied Superconductivity* **17** No. 2 808-811 2007

A. T. Cayless, S. R. Hoon, B. K. Tanner, R. W. Chantrell, M. Kilner: High Sensitivity Measurements of Néel Relaxation in Fine Particle Ferromagnetic Systems *Journal of Magnetism and Magnetic Materials* **30** 303-311 1983

R. W. Chantrell, S. R. Hoon, B. K. Tanner: Time-Dependent Magnetization in Fine-Particle Ferromagnetic Systems *Journal of Magnetism and Magnetic Materials* **38** 133-141 1983

Chemicell, personal communication 2009

Chemicell 2009 www.chemicell.com/products/nanoparticles/fluidmag-affinity/index.html

B. Chesca: Theory of RF SQUIDs Operating in the Presence of Large Thermal Fluctuations *Journal of Low Temperature Physics* **110** No. 5/6 963-1001 1998

S. H. Chung, A. Hoffmann, S. D. Bader: Biological sensors based on Brownian relaxation of magnetic nanoparticles *Applied Physics Letters* **85** No. 14 2971-2973 2004

S. H. Chung, A. Hoffmann, K. Guslienko, S. D. Bader, C. Liu, B. Kay, L. Makowski, L. Chen: Biological Sensing with magnetic nanoparticles using Brownian relaxation *Journal of Applied Physics* **97** 2005

J. Clarke, A. I. Braginski: *The SQUID Handbook Vol. I Fundmentals and Technology of SQUIDs and SQUID Systems* Weinheim: WILEY-VCH 2004

J. Connolly, T. G. St Pierre: Proposed biosensors based on time-dependent properties of magnetic fluids *Journal of Magnetism and Magnetic Materials* **225** 156-160 2001

K. A. Connors: *Binding Constants The Measurement of Molecular Complex Stability* New York: John Wiley & Sons 1987

R. M. Cornell, U. Schwertmann: *The Iron Oxides* 2nd ed. Weinheim: Wiley-VCH 2003

D. E. McCumber: Tunneling and Weak-Link Superconductor Phenomena Having Potential Device Application *Journal of Applied Physics* **39** No. 6 2503-2508 1968

J. Dechert, M. Mueck, C. Heiden: A Scanning SQUID Microscope for Samples at Room Temperature, *IEEE Transactions on Applied Superconductivity* **9** Issue 2 4111-4114 1999

R. Doll, M. Näbauer: Experimental Proof of Magnetic Flux Quantization in a Superconducting Ring *Physical Review Letters* **7** No. 2 51-52 1961

D. J. Dunlop: Monodomain Theory: Experimental Verification *Science* **162** 256-258 1968

H. F. Ebel, C. Bliefert, W. E. Russey: *The art of scientific writing: from student reports to professional publications in chemistry and related fields* 2nd ed. Weinheim: Wiley-VCH 2004

D. Eberbeck, A. Lange, M. Hentschel: Identification of aggregates of magnetic nano-particles in ferrofluids at low concentrations *Journal of Applied Crystallography* **36** 1069-1074 2003

D. Eberbeck, C. Bergemann, S. Hartwig, U. Steinhoff, L. Trahms: Binding kinetics of magnetic nanoparticles on latex beads and yeast cells studied by magnetorelaxometry *Journal of Magnetism and Magnetic Materials* **289** 435–438 2005

D. Eberbeck, personal communication 2009

K. Enpuku, T. Minotani, M. Hotta and A. Nakahodo: Application of High Tc SQUID Magnetometer to Biological Immunoassays *IEEE Transactions on Applied Superconductivity* **11** No. 1 661-664 2001

K. Enpuku, D. Kuroda, A. Ohba, T. Q. Yang, K. Yoshinaga, T. Nakahara, H. Kuma, N. Hamasaki: Biological Immunoassay Utilizing Magnetic Marker and High Tc Superconducting Quantum Interference Device Magnetometer *Japanese Journal of Applied Physics* **42** Part 2 No. 12A 1436–1438 2003

K. Enpuku, T. Tanaka, T. Matsuda, H. Kuma, N. Hamasaki, F. Dang, N. Enomoto, J. Hojo, K. Yoshinaga, F. Ludwig, F. Ghaffari, E. Heim, M. Schilling: Liquid Phase Immunoassay Using Magnetic Markers and Superconducting Quantum Interference Device *Japanese Journal of Applied Physics* **46** No. 11 7524–7529 2007

K. Enpuku, K. Soejima, T. Nishimoto, T. Matsuda, H. Tokumitsu, T. Tanaka, K. Yoshinaga, H. Kuma, N. Hamasaki: Biological Immunoassays Without Bound/Free Separation Utilizing Magnetic Marker and HTS SQUID *IEEE Transactions on Applied Superconductivity* **17** No. 2 816-819 2007

K. Enpuku, Y. Tamai, T. Mitake, M. Matsuo, A. Tsukamoto, T. Mizoguchi, A. Kandori: Liquid Phase Immunoassay Using AC Susceptibility Measurement of Magnetic Markers *Applied Physics Express* **2** 2009

R. L. Fagaly: Superconducting quantum interference device instruments and applications *Review of Scientific Instruments* **77** 101101-101146 2006

X. Fan, I. M. White, S. I. Shopova, H. Zhu, J. D. Suter, J. Sun: Sensitive optical biosensors for unlabeled targets: A review *Analytica Chimica Acta* **620** 8–26 2008

P. C. Fannin, B. K. P. Scaife, S. W. Charles: New technique for measuring the complex susceptibility of ferrofluids *Journal of Physics E: Scientific Instruments* **19** 238-239 1986

P. C. Fannin and T. Relihan: Experimental and theoretical profiles of the frequency-dependent complex susceptibility of systems containing nanometer-sized magnetic particles *Physical Review B* **55** No. 21 14423-14428 1987

P. C. Fannin, B. K. P. Scaife: The Measurement of the Frequency Dependent Susceptibility of Magnetic Colloids *Journal of Magnetism and Magnetic Materials* **72** 95-108 1988

B. Fischer, B. Huke, M. Lucke, R. Hempelmann: Brownian relaxation of magnetic colloids *Journal of Magnetism and Magnetic Materials* **289** 74–77 2005

J. Fritz, D. Anselmetti, J. Jarchow, X. Fernandez-Busquets: Probing Single Biomolecules with Atomic Force Microscopy *Journal of Structural Biology* **119** 165-171 1997

J. K. Galt: Motion of a ferromagnetic domain wall in Fe304 *Physical Review* **85** (4) 664-669 1952

W. Göpel, J. Hesse. J. N. Zemel (ed.): *Sensors Vol. 5 Magnetic Sensors* Weinheim: Wiley-VCH 1989

D. L. Graham, H. A. Ferreira, P. P. Freitas: Magnetoresistive-based biosensors and biochips *TRENDS in Biotechnology* **22** No.9 456-462 2004

H. L. Grossman, W. R. Myers, V. J. Vreeland, R. Bruehl, M. D. Alper, C. R. Bertozzi, J. Clarke: Detection of bacteria in suspension by using a superconducting quantum interference device Proceedings of the National Academy of Sciences **101** No. 1 129-134 2004

A. Grunwald: *Technikfolgenabschätzung – Eine Einführung* Berlin: edition Sigma 2002

S. A. Gudoshnikov, B.Y. Liubimov, Y. V. Deryuzhkina, L. V. Matveets, O. V. Snigirev, A. S. Kalabukhov, M. L. Ranchinski, F. Schmidl, P. Seidel: HTS scanning SQUID microscope with high spatial resolution for room temperature samples *Physica C* **372-376** 166- 169 2002

H. Gu, K. Xu, C. Xu, B. Xu: Biofunctional magnetic nanoparticles for protein separation and pathogen detection *Chemical Communications* No. 9 941-949 2006

T. Hayashi, H. Itozaki: SQUID Probe Microscope With Through-Hole SQUID *IEEE Transactions on Applied Superconductivity* **15** No. 2 737-740 2005

M. He, M. J. Taussig: Technique Review Ribosome display: Cell-free protein display technology *Briefings in Functional Genomics and Proteomics* **1** No. 2 204-212 2002

D. F. He, M. Tachiki, H. Itozaki: Highly sensitive anisotropic magnetoresistance magnetometer for Eddy-current nondestructive evaluation **80** Issue 3 R*eview of Scientific Instruments* 2009

E. Heim, F. Ludwig, M. Schilling: Binding assays with streptavidin-functionalized superparamagnetic nanoparticles and biotinylated analytes using fluxgate magnetorelaxometry *Journal of Magnetism and Magnetic Materials* **321** 1628–1631 2009

C. Hempen, U. Karst: Labeling strategies for bioassays Analytical and Bioanalytical Chemistry **384** No. 3 572-583 2005

T. G. Henares, F. Mizutani, H. Hisamoto: Current development in microfluidic immunosensing chip *Analytica Chimica Acta* **611** 17-30 2008

C. Hinnrichs, J. Stahl, K. Kuchenbrandt, M. Schilling: Dependence of Sensitivity and Noise of Fluxgate Sensors on Racetrack Geometry *IEEE Transactions on Magnetics* **37** No. 4 1983-1985 2001

P. Hinterdorfer, Y. F. Dufrêne: Detection and localization of single molecular recognition events using atomic force microscopy *Nature Methods* **3** No.5 347-355 2006

D. Horák, M. Babic, H. Macková, M. J. Benes: Preparation and properties of magnetic nano- and microsized particles for biological and environmental separations *Journal of Separation Science* **30** 1751–1772 2007

H. E. Horng, S. Y. Yang, Y. W. Huang, W. Q. Jiang, C.-Y. Hong, and H. C. Yang: Nanomagnetic Particles for SQUID-Based Magnetically Labeled Immunoassay *IEEE Transactions on Applied Superconductivity* **15** No. 2 2005

D. L. Huber: Synthesis, Properties, and Applications of Iron Nanoparticles *small* **1** No. 5 482-501 2005

H. Itozaki, T. Kondo, T. Nagaishi: HTS scanning SQUID microscope *Physica C* **392–396** 1392–1395 2003

B. Josephson: Possible New Effects in Superconductive Tunneling *Physics Letters* **1** No. 7 251-253 1962

N. D. Kataria, V. S. Tomar, A. K. Gupta, M. Kumar: Josephson effects in a constricted Bi-Sr-Ca-Cu-0 bulk superconductor *Journal of Physics C: Solid State Physics* **21** 523-527 1988

M. H. Ketchen, W. J. Gallagher, A. W. Kleinsasser, S. Murphy, J. R. Clem: DC Flux Focuser in: *SQUID '85* edited by H. D. Hahlbohm, H. Lubbig Berlin: de Gruyter 1985

P. T. Keyser, S. R. Jefferts: Magnetic susceptibility of some materials used for apparatus construction (at 295 K) *Review of Scientific Instruments* **60** (8) 2711-2714 1989

F. Kienberger, A. Ebner, H. J. Gruber, P. Hinterdorfer: Molecular Recognition Imaging and Force Spectroscopy of Single Biomolecules *Accounts of Chemical Research* 39 No. 1 29-36 2006

J. R. Kirtley: SQUID microscopy for fundamental studies *Physica C* **368** 55–65 2002

T. G. M. Kleinpenning: Design of an a.c. micro-gauss sensor *Sensors Actuators* **4** No. 1 3-9 1983

D. Koelle, R. Kleiner, F. Ludwig, E. Dantsker, J. Clarke: High-transition-temperature superconducting quantum interference devices *Reviews of Modern Physics* **71** No. 3 631-686 1999

G. H. Koenderink, A. P. Philipse: Rotational and Translational Self-Diffusion in Colloidal Sphere Suspensions and the Applicability of Generalized Stokes-Einstein Relations *Langmuir* **16** No. 13 5631-5638 2000

I. K. Kominis, T. W. Kornack, J. C. Allred, M. V. Romalis: A subfemtotesla multichannel atomic magnetometer *Nature* **422** 596-599 2003

R. Kötitz, H. Matz, L. Trahms, H. Koch: SQUID Based Remanence Measurements for Immunoassays *IEEE Transactions on Applied Superconductivity* **7** No. 2 3678-3681 1997

R. Kötitz, W. Weitschies, L. Trahms, W. Brewer, W. Semmler: Determination of the binding reaction between avidin and biotin by relaxation measurements of magnetic nanoparticles *Journal of Magnetism and Magnetic Materials* **194** 62-68 1999

H.-J. Krause, N. Wolters, Y. Zhang, A. Offenhäusser, P. Miethe, M. H. F. Meyer, M. Hartmann, M. Keusgen: Magnetic particle detection by frequency mixing for immunoassay applications *Journal of Magnetism and Magnetic Materials* **311** 436–444 2007

C. B. Kriz, K. Rådevik, D. Kriz: Magnetic Permeability Measurements in Bioanalysis and Biosensors *Analytical Chemistry* **68** 1966-1970 1996

K. Kriz, J. Gehrke, D. Kriz: Advancements toward magneto immunoassays *Biosensors & Bioelectronics* **13** 817–823 1998

J. Lange, R. Kötitz, A. Haller, L. Trahms, W. Semmler, W. Weitschies: Magnetorelaxometry — a new binding specific detection method based on magnetic nanoparticles *Journal of Magnetism and Magnetic Materials* **252** 381–383 2002

S. K. Lee, W. R. Myers, H. L. Grossman, H.-M. Cho, Y. R. Chemla, J. Clarke: Magnetic gradiometer based on a high-transition temperature superconducting quantum interference device for improved sensitivity of a biosensor *Applied Physics Letters* **81** No. 16 3094-3096 2002

T. S. Lee, E. Dantsker, J. Clarke: High-transition temperature superconducting quantum interference device microscope *Review of Scientific Instruments* **67** Issue 12 4208-4215 1996

N. Lewinski, V. Colvin, R. Drezek: Cytotoxicity of Nanoparticles *small* **4** Issue 4 26-49 2008

T.-H. Lin, G. D. J. Phillies: Probe Diffusion in Poly(acrylic acid)-Water. Effect of Probe Size *Macromolecules* **17** 1686-1691 1984

X.-M. Lin, A. C. S. Samia: Synthesis, assembly and physical properties of magnetic nanoparticles *Journal of Magnetism and Magnetic Materials* **305** 100–109 2006

G. Liu, J. Wang, H. Wu, Y. Lin, Y. Lin: Nanovehicles Based Bioassay Labels *Electroanalysis* **19** No.7-8 777–785 2007

F. Ludwig, E. Heim, S. Mäuselein, D. Eberbeck, Meinhard Schilling: Magnetorelaxometry of magnetic nanoparticles with fluxgate magnetometers for the analysis of biological targets *Journal of Magnetism and Magnetic Materials* **293** 690–695 2005

F. Ludwig, E. Heim, M. Schilling: Characterization of magnetic core–shell nanoparticles by fluxgate magnetorelaxometry, ac susceptibility, transmission electron microscopy and photon correlation spectroscopy - A comparative study *Journal of Magnetism and Magnetic Materials* **321** 1644-1647 2009

C. A. Marquette, L. J. Blum: State of the art and recent advances in immunoanalytical systems *Biosensors and Bioelectronics* **21** 1424-1433 2006

V. C. Martins, F. A. Cardoso, J. Germanod, S. Cardosoa, L. Sousad, M. Piedade, P. P. Freitas, L. P. Fonseca: Femtomolar limit of detection with a magnetoresistive biochip *Biosensors and Bioelectronics* **24** 2690–2695 2009

J. Matthews, S. Y. Lee, F. C. Wellstood, A. F. Gilbertson, G. E. Moore, and S. Chatraphorn: Multi Channel High-Tc Scanning SQUID Microscope *IEEE Transactions on Applied Superconductivity* **13** No. 2 219-222 2003

M. H. F. Meyer, H.-J. Krause, M. Hartmann, P. Miethe, J. Oster, M. Keusgen: Francisella tularensis detection using magnetic labels and a magnetic biosensor based on frequency mixing *Journal of Magnetism and Magnetic Materials* **311** 259–263 2007

G. Mihajlović, K. Aledealat, P. Xiong, S. v. Molnár, M. Field, G. J. Sullivan: Magnetic characterization of a single superparamagnetic bead by phase-sensitive micro-Hall magnetometry *Applied Physics Letters* **91** 2007

L. N. C. Morgan, C. Carr, A. Cochran, D. McA. McKirdy and G. B. Donaldson: Electro-magnetic Nondestructive Evaluation With Simple HTS SQUIDs: Measurements and Modelling *IEEE Transactions on Applied Superconductivity* **5** No. 2 3127-3130 1995

G. Möllenstedt, W. Bayh: Elektronen-Biprisma-Interferenzen mit weit getrennten kohärenten Teilbündeln *Naturwissenschaften* **48** No. 10 400 1961

M. Mück, B. Chesca, Y. Zhang: Radio Frequency SQUIDs and Their Applications in: *NATO Advanced Study Institute on Microwave Superconductivity* edited by H. Weinstock New York: Springer-Verlag 2000

S. P. Mulvaney, C. L. Cole, M. D. Kniller, M. Malito, C. R. Tamanaha, J. C. Rife, M. W.: Rapid, femtomolar bioassays in complex matrices combining microfluidics and magnetoelectronics *Biosensors and Bioelectronics* **23** 191–200 2007

H. Nakamura, I. Karube: Current research activity in biosensors *Analytical and Bioanalytical Chemistry* **377** 446–468 2003

J. Niebuhr, G. Lindner: *Physikalische Messtechnik mit Sensoren* Oldenburg: Industrieverlag 2002

P. I. Nikitin, P. M. Vetoshko, T. I. Ksenevicha: New type of biosensor based on magnetic nanoparticle detection *Journal of Magnetism and Magnetic Materials* **311** 445–449 2007

L. Nicu, T. Leïchlé: Biosensors and tools for surface functionalization from the macro- to the nanoscale: The way forward *Journal of Applied Physics* **104** Issue 11 111101-1111106 2008

F. Öisjöen, P. Magnelind, A. Kalabukhov, D. Winkler: High-T_C SQUID gradiometer system for immunoassays *Superconductivity Science and Technology* **21** 034004 2008

R. de Bruyn Ouboter: Superconductivity: Discoveries during the early years of low temperature research at Leiden 1908-1914 *IEEE Transactions on Magnetics* **MAG-23** No. 2 355-370 1987

Q. A. Pankhurst, J. Conolly, S. K. Jones, J. Dobson: Applications of magnetic nanoparticles in biomedicine *Journal of Physics D: Applied Physics* **36** 167-181 2003

M. Pannetier, C. Fermona, G. Le Goff, J. Simola, E. Kerr, J.M.D. Coey: Noise in smallmagnetic systems—applications to very sensitive magnetoresistive sensors *Journal of Magnetism and Magnetic Materials* **290–291** 1158–1160 2005

T. L. Paoli, J. F. Svacek: Derivative Measurement by Frequency Mixing *Review of Scientific Instruments* **47** No. 9 1016-1019 1976

A. Pretzell, H.-J. Krause, Y. Zhang, A. Offenhäusser: HTS rf SQUID System for Magnetic Nanoparticle Readout *Sensor Letters* **7** No. 3 2009 submitted

A. Prieto Astalan, F. Ahrentorp, C. Johansson, K. Larsson, A. Krozer: Biomolecular reactions studied using changes in Brownian rotation dynamics of magnetic particles *Biosensors and Bioelectronics* **19** 945–951 2004

A. Prieto Astalan, C. Jonasson, K. Petersson, J. Blomgren, D. Ilver, A. Krozer, C. Johansson: Magnetic response of thermally blocked magnetic nanoparticles in a pulsed magnetic field *Journal of Magnetism and Magnetic Materials* **311** 166–170 2006

A. M. Raem, P. Rauch: *Immunoassays* München: Elsevier GmbH 2007

P. Reimer, T. Balzer: Ferucarbotran (Resovist): a new clinically approved RES-specific contrast agent for contrast-enhanced MRI of the liver: properties, clinical development, and applications *European Radiology* **13** 1266-1276 2003

G. Reiss, H. Brückl, A. Hütten, J. Schotter, M. Brzeska, M. Panhorst, D. Sudfeld, A. Becker, P. B. Kamp, A. Pühler, K. Wojczykowski, P. Jutzi: Magnetoresistive sensors and magnetic nanoparticles for biotechnology *Journal of Materials Research* **20** No. 12 3294-3302 2005

D. Robbes: Highly sensitive magnetometers — a review *Sensors and Actuators A* **129** 86–93 2006

K. Sata, T. Ishida: Development of high-T_C SQUID microscope *Physica B: Condensed Matter* **329-333** Part 2 1502-1503 2003

S. K. Sahoo, V. Labhasetwar: Nanotech approaches to drug delivery and imaging *Drug Discovery Today* **8** No. 24 1112-1120 2003

M. Schmidt, H.-J. Krause, M. Banzet, D. Lomparski, J. Schubert, W. Zander, Y. Zhang, R. Akram, M. Fardmanesh: The set-up of a high temperature superconductor radio-frequency SQUID microscope for magnetic nanoparticle detection *Superconductivity Science and Technology* **19** 261–265 2006

J. Schotter, A. Shoshi, H. Brückl: Development of a magnetic lab-on-a-chip for point- of-care sepsis diagnosis *Journal of Magnetism and Magnetic Materials* **321** 1671–1675 2009

V. Shah, S. Knappe, P. D. D. Schwindt, J. Kitching: Subpicotesla atomic magnetometry with a microfabricated vapour cell *Nature Photonics* **1** 649-652 2007

A. H. Silver, J. E. Zimmermann: Quantum Transitions and Loss in Multiply Connected Superconductors *Physical Review Letters* **15** No. 23 888-891 1965

A. H. Silver, J. E. Zimmermann: Quantum States and Transitions in Weakly Connected Superconducting Rings *Physical Review* **157** No. 2 317-341 1967

B. Srinivasan, Y. Li, Y. Jing, Y. Xu, X. Yao, C. Xing, J.-P. Wang: A Detection System Based on Magnetoresistive Sensors and High-Moment Magnetic Nanoparticles Demonstrates Zeptomole Sensitivity: Potential for Personalized Medicine *Angewandte Chemie* **121** Issue 15 2802-2805 2009

W. C. Stewart: Current-Voltage Characteristics of Josephson Junctions A*pplied Physics Letters* **12** No. 8 277-280 1968

K. Sternickel, A. I. Braginski: Biomagnetism using SQUIDs: status and perspectives *Superconductivity Science and Technology* **19** 160–171 2006

L. Tabet: *Magnetic Nanoparticle Detection Using a SQUID Microscope* Internal Internship Report Research Centre Juelich 2006

M. A. Tafhime: *Development of a resonant tank circuit for gradiometric SQUID operation* Master of Science Thesis Research Centre Juelich 2006

C. R. Tamanaha, S. P. Mulvaney, J. C. Rife, L. J. Whitman: Magnetic labeling, detection, and system integration *Biosensors and Bioelectronics* **24** 1–13 2008

Z. Tang, H. T. Karnes: Coupling immunoassays with chromatographic separation techniques *Biomedical Chromatography* **14** 442-449 2000

A. S. Teja, P.-Y. Koh: Synthesis, properties, and applications of magnetic iron oxide nanoparticles *Progress in Crystal Growth and Characterization of Materials* **55** 22-45 2009

K. Teeparuksapun, P. Kanatharana, W. Limbut, C. Thammakhet, P. Asawatreratanakul, B. Mattiasson,B. Wongkittisuksa, C. Limsakul, P. Thavarungkul: Disposable Electrodes for Capacitive Immunosensor *Electroanalysis* **21** No. 9 1066–1074 2009

A. Thünemann, S. Rolf, P. Knappe, S. Weidner: In Situ Analysis of a Bimodal Size Distribution of Superparamagnetic Nanoparticles *Analytical Chemistry* **81** 296-301 2009

K. Tsukada, T. Kiwa, Y. Masuda: AC Magnetic Properties of Large Volume of Water – Susceptibility Measurement in Unshielded Environment *Japanese Journal of Applied Physics* **45** 1097-1099 2006

A. Tsukamoto, K. Saitoh, D. Suzuki, N. Sugita, Y. Seki, A. Kandori, K. Tsukada, Y. Sugiura, S. Hamaoka, H. Kuma, N. Hamasaki, and K. Enpuku: Development of Multisample Biological Immunoassay System Using HTS SQUID and Magnetic Nanoparticles *IEEE Transactions on Applied Superconductivity* **15** No. 2 656-659 2005

uniprot 2009 www.uniprot.org

Vacuumschmelze 2009 www.vacuumschmelze/dynamic/en/home/products/materialsampparts/softmagnetic.php

A. Voller, A. Bartlett, D. E. Bidwell: Enzyme immunoassays with special reference to ELISA techniques *Journal of Clinical Pathology* **31** 507-520 1978

S. X. Wang, G. Li: Advances in Giant Magnetoresistance Biosensors With Magnetic Nanoparticle Tags: Review and Outlook *IEEE Transactions on Magnetics* **44** No. 7 1687-1702 2008

A. Warsinke: Point-of-care testing of proteins *Analytical and Bioanalytical Chemistry* **393** 1393–1405 2009

W. Wernsdorfer, E. Bonet Orozco, K. Hasselbach, A. Benoit, B. Barbara, N. Demoncy, A. Loiseau, H. Pascard, D. Mailly: Experimental Evidence of the Néel-Brown Model of Magnetization Reversal *Physical Review Letters* **78** No. 9 1791-1794 1997

H.-C. Yang, C. H. Wu, J. C. Chen, K. L. Chen and M. J. Chen, S. H. Liao, H. E. Horng, S. Y. Yang: High-Tc Superconducting Quantum Interference Devices and Biomagnetic Applications *Journal of the Korean Physical Society* **48** No. 5 1084-1089 2006a

H.-C. Yang, S. Y. Yang, G. L. Fang, W. H. Huang, C. H. Liu, S. H. Liao, H. E. Horng, C.- Y. Hong: Magnetic relaxation measurement in immunoassay using high-transition-temperature superconducting quantum interference device system *Journal of Applied Physics* **99** 2006b

H.-C. Yang, J.-C. Chen, K.-L. Chen, C.-H. Wu, H.-E. Horng, S. Y. Yang: High-T_c superconducting quantum interference devices: Status and perspectives *Journal of Applied Physics* **104** 2008

T. Q. Yang, M. Abe, K. Horiguchi, K. Enpuku: Detection of magnetic nanoparticles with ac susceptibility measurement *Physica C* **412–414** 1496–1500 2004

X. Zeng: *Experimental Study of HTS SQUIDs at Large Thermal Fluctuations* Jülich: Berichte des Forschungszentrums Jülich 2000

B. Zhang, X. Liang, L. Hao, J. Cheng, X. Gong, X. Liu, G. Ma, J. Chang: Quantum dots/particle-based immunofluorescence assay: Synthesis, characterization and application *Journal of Photochemistry and Photobiology B: Biology* **94** 45–50 2009

Y. Zhang: *RF-SQUIDs aus oxydkeramischen Supraleitern: Präparation und Charakterisierung* Giessen: Inaugural Dissertation der Justus-Liebig-Universität 1990

Y. Zhang, H. Soltner, H.-J. Krause, E. Sodtke, W. Zander, J. Schubert, M. Grüneklee, D. Lomparski, M. Banzet, H. Bousack, A. I. Braginski: Planar HTS Gradiometers with Large Baseline *IEEE Transactions on Applied Superconductivity* **7** Issue 2 2866-2869 1997

L. Zhao, L. Sun, X. Chu: Chemiluminescence immunoassay *Trends in Analytical Chemistry* **28** No. 4 404-415 2009

C. Zhong, F. Li, F. Zhang, H. Ding, L. Hongsheng, L. Sheng, H. Dehua, Y. He: Scanning SQUID Microscope and its Application in Detecting Weak Currents I*nternational Journal of Modern Physics B* **19** Issue 1-3 431-433 2005

J. E. Zimmerman, J. A. Beall, M. W. Cromar, R. H. Ono: Operation of Y-Ba-O-Cu rf SQUID at 81 K *Applied Physics Letters* **51** No. 8 617-618 1987

J. A. Zimmermann, A. H. Silver: A High-Sensitivity Superconducting Detector *Journal of Applied Physics* **39** No. 6 2679-2682 1968

Annex

Abbreviations, Symbols and Constants

Vectorial quantities are in bold face, physical quantities in italic.

A	area (m^2)
AC	alternating current
B	magnetic induction (T)
BNC	Bayonet Neill-Concelman
BW	bandwidth (Hz)
C	capacitance (F)
cfu	colony forming units
CMOS	complementary metal oxide semiconductor
D	diffusion constant (m^2/s)
d	diameter (m)
DC	direct current
dB	decibel
DIN	Deutsches Institut für Normung (German Institute for Standardization)
e	elementary charge: $1.602 \cdot 10^{-19}$ C
E	energy (J)
ELISA	enzyme linked immunosorbent assay
EU	European Union
GMR	giant magnetoresistance
h	Planck constant: $6.626 \cdot 10^{-34}$ J·s
H	magnetic field strength (A/m)

HTS	high temperature superconductivity
I	current (A)
IR	infrared
j	heat flow (J/s)
k	Boltzmann constant: $1.381 \cdot 10^{23}$ J/K
k	coupling constant
K	anisotropy constant (J/m^3)
l	length (m)
L	Langevin function
L	inductance (H)
LN2	liquid nitrogen
LTS	low temperature superconductivity
$\boldsymbol{m}$	magnetic moment (Am^2)
M	mol/litre
$\boldsymbol{M}$	magnetization (A/m)
MCG	magnetocardiography
MRI	magnetic resonance imaging
N	number
NMR	nuclear magnetic resonance
rf	radio-frequency
PEEK	polyetheretherketone
Pt 100	temperature sensor
Q	quality factor
$\boldsymbol{r}$	point in three-dimensional space
R	resistance [Ω]
RCSJ	resistive-capacitive shunted junction
rpm	rounds per minute

SERF	spin exchange relaxation-free
SMD	surface-mounted device
SPR	surface plasmon resonance
SQUID	superconducting quantum interference device
t	time (s)
T	temperature (K)
V	voltage (V)
v	volume (m^3)
VCA	voltage controlled attenuator
VCO	voltage controlled oscillator
YBCO	yttrium barium copper oxide
z	complex number
Δ	difference
η	viscosity $(N \cdot s)/m^2$
θ	phase (deg)
λ	thermal conductivity $J/(s \cdot m \cdot K)$
μ_0	vacuum permeability: $4\pi \cdot 10^{-7}$ $(T \cdot m)/A$
τ	relaxation time (s)
Φ	magnetic flux (Tm^2)
Φ_0	magnetic flux quantum: $2.068 \cdot 10^{-15}$ Tm^2
χ	magnetic susceptibility

Instruments

Current generator	NGT 20 by Rohde und Schwarz / Precision: 2.5 %
Fluxgate	Fluxmaster by S. Mayer / Precision 0.5 % or ± 5 nT
Interface	BNC-2120 by National Instruments

Helium leak detector	UL 200 by Leybold / Precision: $5 \cdot 10^{-11}$ mbar l/s minimally detectable leak rate
Lock-in amplifier	SR830 DSP by Stanford Research Systems / Precision: 1% gain accuracy, 6 $nV/Hz^{1/2}$ input noise, phase error 1 deg absolute, frequency 25 ppm, amplitude 1 %
Multimeter	2000 by Keithley
Network analyzer	8711C by Hewlett Packard
Oscilloscope	203-7 by Hameg
Power amplifier	TOE 7610 by Toellner / Precision: ±0.1 mV eff. < 1 kHz
Signal generator	TG210 by Thurlby Thandar / Precision: amplitude 5 %, frequency 1 %
Spectrum analyzer	35670A by Hewlett Packard
Turbomolecular vacuum pump	TCP 380 by Balzers
Vacuum gauge	Compact Full Range Gauge PKR 251 by Balzers

Consumables

Biotin-Agarose B0519	by Sigma-Aldrich
Resovist nanoparticles	by Schering
FluidMAG-Streptavidin	by Chemicell
Two-component glue	Uhu Endfest by Henkel
Heat conducting paste	70-AM by GLT Germany
Vacuum grease	by Apiezon

Components

Cryostat	by Messer Cryotherm
Capillaries	by Hilgenberg
SMD capacitor	MPR 11P 1ROBN by Microelectronics Ltd.
Pt 100 sensor	Pt 100A-3/08 ls. by Electronic Sensor, Heilbronn

Software

AutoCAD LT 2004	by Autodesk Inc.
LabVIEW 8.2	by National Instruments
Open Office 3.1	by openoffice.org
Origin 5.0	by Origin Labs Inc.

Physical Data

Table 16: Data for the iron oxides, which build the core of the used particles [Cornell 2003].

Substance	Chemical structure	Magnetism	Specific saturation magnetization (Am^2/kg)	Density (kg/m^3)
magnetite	Fe_3O_4	ferrimagnetic	92-100 (300K)	$5.18 \cdot 10^3$
maghemite	γ-Fe_2O_3	ferrimagnetic	60-80 (300K)	$4.87 \cdot 10^3$

Table 17: Important data of the used particles [Chemicell 2009], [Reimer 2003], [Ludwig 2009], [Thünemann 2009].

Particles	Hydro-dynamic diameter (nm)	Core diameter (nm)	Core matter	Shell matter	Satura-tion magne-tization	Particles per ml
FluidMAG	97 nm $\sigma = 0.33$	crystals of 12 nm $\sigma = 0.24$	magnetite	starch	3100 A/m	$1.8 \cdot 10^{13}$
Resovist	62 nm	crystals of 5 ± 1.2 nm and 9.9 ±1.6 nm	magnetite/ maghemite	carboxy-dextran	-	-
Agarose beads	40 – 165 µm	no magnetic core	agarose		-	-

Table 18: Properties of the biotin-streptavidin system [uniprot 2009].

Molecule	Molecular weight (g/mol)	Binding sites	Dissociation constant K_D (M)
biotin	18834	1	$\approx 10^{-15}$
streptavidin	244.31	4	

Table 19: Magnetic and electric properties of the materials used for the device - references as indicated.

Material	Susceptibility χ	Electric permittivity ε	Electric conductivity
stainless steel	0.05 – 0.1 typical [BSSA 2009]	∞	metallic conductor
µ-metal	350000 typical [Vacuumschmelze 2009]	∞	metallic conductor
copper	$-9.8 \cdot 10^{-6}$ [Keyser 1989]	∞	metallic conductor
sapphire	$-17.0 \cdot 10^{-6}$ [Keyser 1989]	10.55 / 8.6 * [Landolt Börnstein]	isolator
PEEK	-	3.3 typical [Boedeker.com 2009]	isolator
Vespel SP-1	$-9.0 \cdot 10^{-6}$ [Keyser 1989]	3.6 typical [Boedeker.com 2009]	isolator
YBCO (supercond.)	-1	∞	superconductor

* parallel / orthogonal to optical axis at 10^{2}-10^{10} Hz

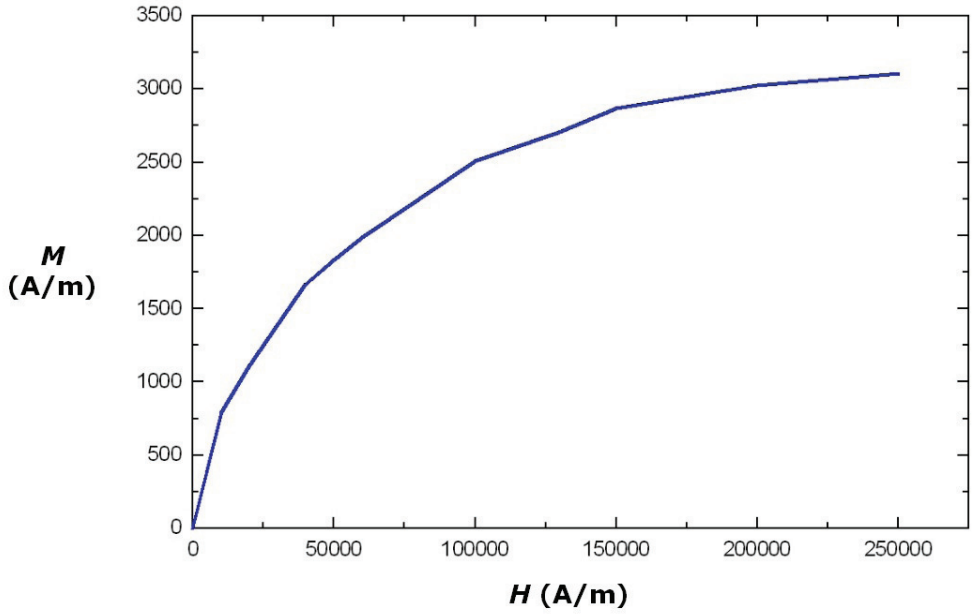

Figure 48: Graph showing the magnetization curve of the FluidMAG particles – data from [Chemicell 2009].

Proofs and Derivations

The transfer function for hysteretic operation - equation (13) in the theoretical chapter - follows from the following relations:

The maximum voltage V_{rf} of the tank circuit relates to the induced critical flux Φ_c in the ring and the mutual inductance M for zero outer field - V_B in Figure 48 - in the following way:

(33) $$V_{rf} = \frac{\omega_0 \cdot L_{TC}}{M} \cdot \Phi_c$$

For an outer field of $\Phi_0/2$ the maximum voltage - V_A in Figure 48 - amounts to

(34) $$V_{rf} = \frac{\omega_0 \cdot L_{TC}}{2\ M} \cdot (\phi_c - \phi_0/2)$$

The peak-to-peak difference of the resulting triangle shaped flux-to-voltage function for half a flux quantum of outer flux is therefore

(35) $$\Delta V_{rf} = \frac{\omega_0 \cdot L_{TC} \cdot \Phi_0}{2\ M}$$

and with the mutual inductance $M = k_1 (L_{TC}\ L_{SQ})^{1/2}$ the transfer function becomes

(36) $$\frac{\partial V_{rf}}{\partial \Phi} = \frac{\Delta V_{rf}}{\Phi_{0/2}} = \frac{\omega_0}{k_1}\left(\frac{L_{TC}}{L_{SQ}}\right)^{1/2}$$

The condition $k^2 Q \geq \pi/2$ - equation (14) in the theoretical chapter - is necessary for proper function of the hysteretic SQUID and can be derived from Figure 49 as follows: The distance I_C - I_A has to be larger than the distance I_B - I_A to be able to use the full difference $\Delta V_{rf} = V_B$ - V_A:

(37) $$I_C - I_A \geq I_B - I_A$$

This equation has to be expressed by other variables to show the condition to be proved.

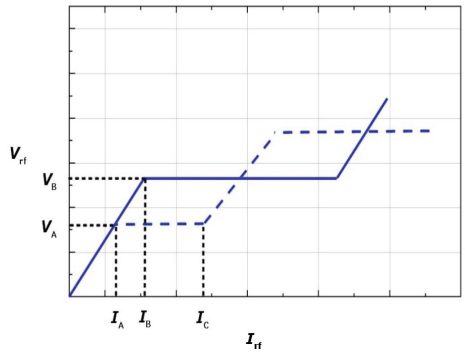

Figure 49: Dependence of the voltage V_{rf} on the current I_{rf} for $\Phi_0/2$ and Φ_0 field flux.

Regarding the term I_B - I_A, the difference of induced flux $\Phi_0/2$ in the SQUID can be expressed as

(38) $$\frac{\Phi_0}{2} = (I_A - I_B)\, MQ$$

The dissipated energy E of the SQUID due to flux catching - approximately the red area in Figure 50 divided by the inductance of the SQUID - can be expressed as:

(39) $$E = \frac{\Phi_c \Phi_0 - \Phi_0^2}{L_{SQ}}$$

The increment of power from I_A to I_C is

(40) $$V_A (I_C - I_A) = \frac{\omega}{2\pi} \cdot E$$

The results of equation (34) can be applied to V_A

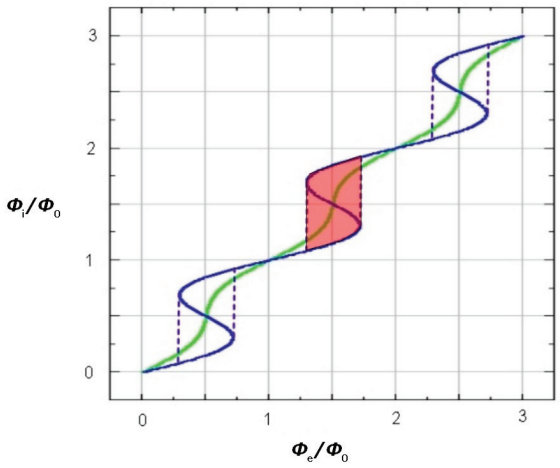

Figure 50: Graph for demonstration of dissipated energy in the tank circuit.

With equations (34), (39), and (40) the term $I_C - I_A$ can now be expressed as

(41) $$I_C - I_A = \frac{M \Phi_0}{\pi L_{SQ} L_{TC}}$$

And finally inserting equations (38) and (41) into equation (37), the result is $k^2 Q \geq \pi/2$.

The Langevin function of paramagnetism - equation (19) in the theoretical chapter - can be derived with the aid of the Stefan-Boltzmann Law: The energy E of a particle with magnetic moment $\boldsymbol{m}$ at an angle θ to the magnetic field of strength $\boldsymbol{B}$ is given by

(42) $$E = - \boldsymbol{m} \cdot \boldsymbol{B} = - m B \cos \theta$$

The probabilities p for the energies E of non-interacting particles in a field of strength B follow the Boltzmann distribution

(43) $$p(E) \sim \exp\left(\frac{m B \cos(\theta)}{k_B T}\right)$$

For a random distribution without any net magnetic moment and energy, the number dn of moments between angles θ and $\theta + d\theta$ is proportional to a strip dA of the surface area of a sphere:

(44) $$dA(\theta) = 2\pi \sin(\theta)\, d\theta ,$$

(45) $$dn(\theta) \sim dA(\theta)$$

Applying a field of strength B, the random distribution is changed to the Boltzmann distribution over this sphere. Bearing in mind the assumption of no interaction of the individual particles:

(46) $$dn(\theta) = C\, 2\pi \sin(\theta) \exp\left(\frac{m B \cos(\theta)}{k_B T}\right) d\theta$$

where C is a normalizing constant,

which equals

(47) $$C = \frac{N}{\int_o^{\pi} 2\pi \sin(\theta) \exp\frac{m\,B\cos(\theta)}{k_B T}\, d\theta}$$

where N denotes the total number of moments. Accordingly, the net magnetization M is specified by the expression

(48) $$M = \int_0^N m \cos(\theta)\, \mathrm{d}\, n$$

or in full

(49) $$M = \frac{N\, m \int_o^{\pi} 2\pi \cos(\theta)\sin(\theta)\exp\frac{m\,B\cos(\theta)}{k_B T}\, d\theta}{\int_o^{\pi} 2\pi \sin(\theta)\exp\frac{m\,B\cos(\theta)}{k_B T}\, d\theta}$$

By substituting $x = \cos(\theta)$ and $\mathrm{d}x = -\sin(\theta)\,\mathrm{d}\theta$ and integrating, the following result is obtained

(50) $$M(B) = N m\left[\coth\left(\frac{m\,B}{k\,T}\right) - \frac{k\,T}{m\,B}\right] = N m\, \mathrm{L}\left(\frac{m\,B}{k\,T}\right)$$

for the Langevin function L.

The principle of lock-in amplification – section 2.5.1 - is as follows: A sinusoidal excitation of the frequency ω_l is generated. The output voltage V_o of the sample is multiplied with a voltage V_l yielding

(51) $$V = V_o V_l \sin(\omega_o t + \theta_o)\sin(\omega_l t + \theta_l)$$

or multiplied

(52) $$V = 0.5\ V_o V_l \cos((\omega_r - \omega_l)t + \theta_o - \theta_l) - 0.5\ V_o V_l \cos((\omega_r + \omega_l)t + \theta_o + \theta_l)$$

This voltage V is run through a low-pass filter, thus cancelling all contributions of the last term –

including most of the noise – except for

(53) $$V = 0.5\ V_o V_I \cos(\theta_o - \theta_I)$$

for $\omega_I = \omega_o$ - the frequency of the excitation signal.

Acknowledgements

My colleagues in this project contributed most of the presented results. My part was mainly to mount and slightly modify the various components and make myself familiar with the underlying principles mentioned and resulting in the theoretical chapter and this thesis. The guide by Ebel, Bliefert and Russey [Ebel 2004] was helpful as an orientation on how to write this thesis. The construction of such a complicated instrument was only possible by intense teamwork:

Marko Banzet – SQUIDs
Willi Bischoff – ceramics dressing
Dr. Dietmar Eberbeck – experiments, theoretical help
Dr. Erik Heim – suggestions
Alexander Hirsch - suggestions
Alexandre Kisner – centrifugation
Dr. Hans-Joachim Krause - calculations, corrections, experiments
Dr. Simin Krause - SQUID electronics
Udo Lesten – leak detection
Dieter Lomparski - software and construction
Dr. Frank Ludwig - theoretical help
Dr. Michael Pabst - theoretical help
Dr. Longqing Qiu – experiments and construction
Dr. Rainer Quaas - nanoparticles
Maik Schmidt - basic system
Dr. Jürgen Schubert – SQUIDs
Heinz Schwan – ceramics dressing
Lyamine Tabet - SQUID characterization
Anik Tafhime - tank circuits
Prof. Dr. Saburo Tanaka – theoretical help
Team of the IBN-2 workshop – construction
Team of the library of the research center - literature
Team of the Technische Informationsbibliothek Hanover - literature
Prof. Dr. Lutz Trahms – theoretical help

Dr. Frank Wiekhorst – theoretical help
Hubert Wirtz and team - liquid nitrogen
Dr. Norbert Wolters - coil electronics
Willi Zander - specimen holder and SQUIDs
Prof. Dr. Yi Zhang - theoretical help

Personally I want to thank my advisors Prof. Dr. Andreas Offenhäusser for help and encouragement, PD Dr. Norbert Klein for his support during my application and especially Dr. Hans-Joachim Krause for his encouragement, for his openness to questions and suggestions as well as for his friendly guidance. Thankfully I want to mention Prof. Dr. Offenhäusser and Prof. Dr. Güntherodt for assessment of the thesis and Dr. Krause for correcting this thesis.

I want to thank the team of the SQUID-lab, the colleagues of IBN-2 and the Biodiagnostics project and many colleagues at the research center Juelich for the welcoming atmosphere.

Finally I also want to thank my family for having supported me during this time.

1. **Soft Matter**
   From Synthetic to Biological Materials
   Lecture manuscripts of the 39th IFF Spring School March 3 – 14, 2008
   Jülich, Germany
   edited by J.K.G. Dhont, G. Gompper, G. Nägele, D. Richter, R.G. Winkler (2008),
   c. 1000 pages
   ISBN: 978-3-89336-517-3

2. **Structural analysis of diblock copolymer nanotemplates using grazing incidence scattering**
   by D. Korolkov (2008), III, 167 pages
   ISBN: 978-3-89336-522-7

3. **Thermal Nonequilibrium**
   Thermal forces in fluid mixtures
   Lecture Notes of the 8th International Meeting on Thermodiffusion,
   9 – 13 June 2008, Bonn, Germany
   edited by S. Wiegand, W. Köhler (2008), 300 pages
   ISBN: 978-3-89336-523-4

4. **Synthesis of CMR manganites and ordering phenomena in complex transition metal oxides**
   by H. Li (2008), IV, 176 pages
   ISBN: 978-3-89336-527-2

5. **Neutron Scattering**
   Lectures of the JCNS Laboratory Course held at the Forschungszentrum Jülich and the research reactor FRM II of TU Munich
   edited by R. Zorn, Th. Brückel, D. Richter (2008), ca. 500 pages
   ISBN: 978-3-89336-532-6

6. **Ultrafast Magnetization Dynamics**
   by S. Woodford (2008), 130 pages
   ISBN: 978-3-89336-536-4

7. **Role of Surface Roughness inTribology: from Atomic to Macroscopic Scale**
   by C. Yang (2008), VII, 166 pages
   ISBN: 978-3-89336-537-1

8. **Strahl- und Spindynamik von Hadronenstrahlen in Mittelenergie-Ringbeschleunigern**
   von A. Lehrach (2008), II, 171 Seiten
   ISBN: 978-3-89336-548-7

9. **Phase Behaviour of Proteins and Colloid-Polymer Mixtures**
   by C. Gögelein (2008), II, 147 pages
   ISBN: 978-3-89336-555-5

10. **Spintronics – From GMR to Quantum Information**
    Lecture Notes of the 40th IFF Spring School March 9 – 20, 2009
    Jülich, Germany
    edited by St. Blügel, D. Bürgler, M. Morgenstern, C. M. Schneider,
    R. Waser (2009), c. 1000 pages
    ISBN: 978-3-89336-559-3

11. **ANKE / PAX Workshop on SPIN Physics**
    JINR, Dubna, Russia / June 22. – 26, 2009
    Org. Committee: A. Kacharava, V. Komarov, A. Kulikov, P. Lenisa, R. Rathmann,
    H. Ströher (2009), CD-ROM
    ISBN: 978-3-89336-586-9

12. **Entwicklung einer Nanotechnologie-Plattform für die Herstellung Crossbar-basierter Speicherarchitekturen**
    von M. Meier (2009), 135 Seiten
    ISBN: 978-3-89336-598-2

13. **Electronic Oxides –**
    Correlation Phenomena, Exotic Phases and Novel Functionalities
    Lecture Notes of the 41st IFF Spring School March 8 – 19, 2010
    Jülich, Germany
    edited by St. Blügel, T. Brückel, R. Waser, C.M. Schneider (2010), ca. 1000 pages
    ISBN: 978-3-89336-609-5

14. **4th Georgian-German School and Workshop in Basic Science**
    Tbilisi, Georgia / May 3 – 7, 2010
    Org. Committee: E. Abrosimova, R. Botchorishvili, A. Kacharava, M. Nioradze,
    A. Prangishvili, H. Ströher (2010); CD-ROM
    ISBN: 978-3-89336-629-3

15. **Neutron Scattering**
    Lectures of the JCNS Laboratory Course held at Forschungszentrum Jülich and the research reactor FRM II of TU Munich
    edited by Th. Brückel, G. Heger, D. Richter, G. Roth and R. Zorn (2010),
    ca 350 pages
    ISBN: 978-3-89336-635-4

16. **Ab *initio* investigations of magnetic properties of ultrathin transition-metal films on *4d* substrates**
    by A. Al-Zubi (2010), II, 143 pages
    ISBN: 978-3-89336-641-5

17. **Investigation of a metal-organic interface realization and understanding of a molecular switch**
    by O. Neucheva (2010), 134 pages
    ISBN: 978-3-89336-650-7

18. **Reine Spinströme in lateralen Spinventilen, *in situ* Erzeugung und Nachweis**
von J. Mennig (2010), V, 95 Seiten
ISBN: 978-3-89336-684-2

19. **Nanoimprint Lithographie als Methode zur chemischen Oberflächen-strukturierung für Anwendungen in der Bioelektronik**
von S. Gilles (2010), II, 169 Seiten
ISBN: 978-3-89336-686-6

20. **Macromolecular Systems in Soft- and Living-Matter**
Lecture Notes of the 42nd IFF Spring School 2011 February 14 – 25, 2011 Jülich, Germany
edited by J. K.G. Dhont, G. Gompper, P. R.Lang, D. Richter, M. Ripoll, D. Willbold, R. Zorn (2011), ca. 1000 pages
ISBN: 978-3-89336-688-0

21. **The spin structure of magnetic nanoparticles and in magnetic nanostructures**
by S. Disch (2011), V, 342 pages
ISBN: 978-3-89336-704-7

22. **Element-selective and time-resolved magnetic investigations in the extreme ultraviolet range**
by P. Grychtol (2011), xii, 144 pages
ISBN: 978-3-89336-706-1

23. **Spin-Transfer Torque Induced Dynamics of Magnetic Vortices in Nanopillars**
by V. Sluka (2011), 121 pages
ISBN: 978-3-89336-717-7

24. **Adsorption von Phthalocyaninen auf Edelmetalloberflächen**
von I. Kröger (2011), vi, 206 Seiten
ISBN: 978-3-89336-720-7

25. **Time-Resolved Single Molecule FRET Studies on Folding/Unfolding Transitions and on Functional Conformational Changes of Phospho-glycerate Kinase**
by T. Rosenkranz (2011), III, 139 pages
ISBN: 978-3-89336-721-4

26. **NMR solution structures of the MloK1 cyclic nucleotide-gated ion channel binding domain**
by S. Schünke (2011), VI, (getr. pag.)
ISBN: 978-3-89336-722-1

27. **Neutron Scattering**
    Lectures of the JCNS Laboratory Course held at Forschungszentrum Jülich and the research reactor FRM II of TU Munich
    edited by Th. Brückel, G. Heger, D. Richter, G. Roth and R. Zorn (2011), ca 350 pages
    ISBN: 978-3-89336-725-2

28. **Neutron Scattering**
    Experiment Manuals of the JCNS Laborator Course held at Forschungszentrum Jülich and the research reactorFRM II of TU Munich
    edited by Th. Brückel, G. Heger, D. Richter, G. Roth and R. Zorn (2011), ca. 180 pages
    ISBN: 978-3-89336-726-9

29. **Silicon nanowire transistor arrays for biomolecular detection**
    by X.T.Vu (2011), vii, 174 pages
    ISBN: 978-3-89336-739-9

30. **Interactions between parallel carbon nanotube quantum dots**
    by K. Goß (2011), viii, 139 pages
    ISBN: 978-3-89336-740-5

31. **Effect of spin-orbit scattering on transport properties of low-dimensional dilute alloys**
    by S. Heers (2011), viii, 216 pages
    ISBN: 978-3-89336-747-4

32. **Charged colloids and proteins: Structure, diffusion, and rheology**
    by M. Heinen (2011), xii, 186 pages
    ISBN: 978-3-89336-751-1

33. **Scattering Methods for Condensed Matter Research: Towards Novel Applications at Future Sources**
    Lecture Notes of the 43rd IFF Spring School 2012
    March 5 – 16, 2012 Jülich, Germany
    edited by M. Angst, T. Brückel, D. Richter, R. Zorn ca. 1000 pages
    ISBN: 978-3-89336-759-7

34. **Single-Site Green Function of the Dirac Equation for Full-Potential Electron Scattering**
    by P. Kordt (2012), 138 pages
    ISBN: 978-3-89336-760-3

35. **Time Resolved Single Molecule Fluorescence Spectroscopy on Surface Tethered and Freely Diffusing Proteins**
    by D. Atta (2012), iv, 126 pages
    ISBN: 978-3-89336-763-4

36. **Fabrication and Utilization of Mechanically Controllable Break Junction for Bioelectronics**
by D. Xiang (2012), 129 pages
ISBN: 978-3-89336-769-6

37. **Contact Mechanics and Friction of Elastic Solids on Hard and Rough Substrates**
by B. Lorenz (2012), iv, 121 pages
ISBN: 978-3-89336-779-5

38. **Ab initio Calculations of Spin-Wave Excitation Spectra from Time-Dependent Density-Functional Theory**
by M. Niesert (2012), 146 pages
ISBN: 978-3-89336-786-3

39. **Neutron Scattering**
Lectures of the JCNS Laboratory Course held at Forschungszentrum Jülich and the research reactor FRM II of TU Munich
edited by Th. Brückel, G. Heger, D. Richter, G. Roth and R. Zorn (2012), ca 350 pages
ISBN: 978-3-89336-789-4

40. **Neutron Scattering**
Experiment Manuals of the JCNS Laborator Course held at Forschungszentrum Jülich and the research reactorFRM II of TU Munich
edited by Th. Brückel, G. Heger, D. Richter, G. Roth and R. Zorn (2012), ca. 175 pages
ISBN: 978-3-89336-790-0

41. **Influence of a shear flow on colloidal depletion interaction**
by C. July (2012), xviii, 105 pages
ISBN: 978-3-89336-791-7

42. **NMR studies on the isolated C39 peptidase-like domain of ABC transporter Haemolysin B from *E. coli*: Investigation of the solution structure and the binding interface with HlyA**
by J. Lecher (2012), 126 pages
ISBN: 978-3-89336-793-1

43. **Spin Correlations and Excitations in Spin-frustrated Molecular and Molecule-based Magnets**
by Z. Fu (2012), 208 pages
ISBN: 978-3-89336-797-9

44. **Crystal and spin structure and their relation to physical properties in some geometrical and spin spiral multiferroics**
by N. K. Chogondahalli Muniraju (2012), iii, 190 pages
ISBN: 978-3-89336-802-0

45. **Multiferroicity in oxide thin films and heterostructures**
by A. Glavic (2012), xi, 152 pages
ISBN: 978-3-89336-803-7

46. **German Neutron Scattering Conference 2012**
September 24 -26, 2012. Gustav-Stresemann-Institut, Bonn, Germany
edited by Th. Brückel (2012)
ISBN: 978-3-89336-807-5

47. **STM beyond vacuum tunnelling: Scanning Tunnelling Hydrogen Microscopy as a route to ultra-high resolution**
by C. Weiss (2012), II, 165 pages
ISBN: 978-3-89336-813-6

48. **High Temperature Radio-Frequency Superconducting Quantum Interference Device System for Detection of Magnetic Nanoparticles**
by A. Pretzell (2012), 122 pages
ISBN: 978-3-89336-814-3

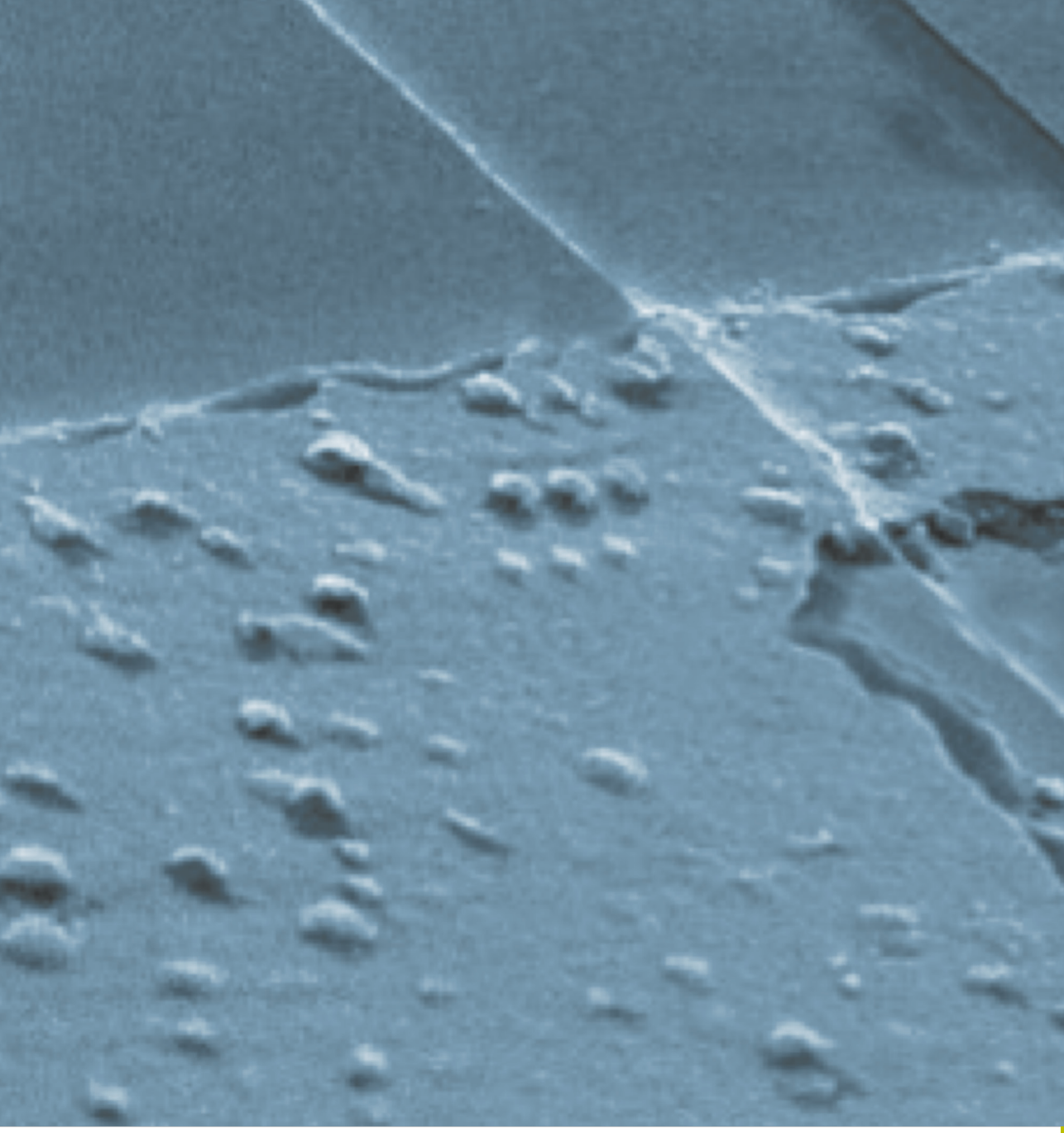

Schlüsseltechnologien / Key Technologies
Band / Volume 48
ISBN 978-3-89336-814-3

JÜLICH
FORSCHUNGSZENTRUM